Title
Slicing and Dicing the Photon Stream as a Photophysical Probe and Imaging Methodology

Author
Sica, Anthony Vincent

Publication Date
2023

Peer reviewed|Thesis/dissertation

UNIVERSITY OF CALIFORNIA

Los Angeles

Slicing and Dicing the Photon Stream

as a Photophysical Probe and Imaging Methodology

A dissertation submitted in partial satisfaction of the

requirements for the degree Doctor of Philosophy

in Chemistry

by

Anthony Vincent Sica

2023

ABSTRACT OF THE DISSERTATION

Slicing and Dicing the Photon Stream

as a Photophysical Probe and Imaging Methodology

by

Anthony Vincent Sica

Doctor of Philosophy in Chemistry

University of California, Los Angeles, 2023

Professor Justin Ryan Caram, Chair

Single photon counting has led to many innovations in the manner we observe physical properties of materials, molecules and biological substrates. This comes with the ability to also generate photon streams that record emissive events on the timescale of picoseconds. Using time correlated single photon counting (TCSPC) the events of light stimulation can be recorded with high precision. I leverage the use of TCSPC as a platform to develop complimentary methods to study and manipulate this collected photon stream. Within this I develop methodologies to probe systems across the spectrum from the UV-visible to the short-wave infrared or SWIR (1-2 μm). In Chapter 1 I describe the basis of using light to stimulate photophysical events, covering definitions and theory. There I will also introduce single photon counting along with the ability to resolve spectral signatures through interferometry.

In Chapter 2, I cover the implementation of Mach-Zehnder interferometry to simultaneously take broadband spectra while retaining the timing information of photon events. We call this technique Decay Associated Fourier Spectroscopy (DAFS), a method that utilizes interferometry to associate photophysical lifetimes with spectral signatures. I demonstrate DAFS' capability by recovering Forster resonance energy transfer (FRET) dynamics for a mixture of an organic dye and quantum dots. I then demonstrate the broadband resolution of DAFS by mixing a visible and SWIR quantum dot and recovering the spectra and lifetime data simultaneously over an octave spanning window.

In Chapter 3, I introduce a follow-up method to the aforementioned DAFS. Taking advantage of the spectral coherence of emitted photon streams, I introduce interferometric or Fourier filtering to separate signals and term this method "Spectrally-selective Time-resolved Emission Filtering" or STEF. I demonstrate STEF in the context of several systems including laser scatter and emitter, mixed and emitters, and imaging biological systems. STEF allows me to bypass the use of conventional filters in the study of complex chromophore mixtures.

In Chapter 4, I then develop another method that utilizes precision timing of multiple pulses to shelf and study short-time events such as fluorescence and long-time events such as phosphorescence simultaneously. Here we term the method fluorescent optical cycling or FOC. Using FOC, I can use pulse trains of on and off times to collect the "total photon economy" or all photon events to understand all radiative, nonradiative, and other energy dissipation pathways. Along with a simple kinetic model, I use FOC to measure these properties in dual emitting platinum complexes, highly phosphorescent anti-boron clusters, and SWIR-emitting singlet oxygen. To finish, I show that FOC and DAFS can be used in tandem to achieve spectral specificity.

I will then finish with a perspective on preliminary efforts to establish measurement schemes that could complement the above novel methods. Within Chapter 5, I describe and demonstrate our ability to collect SWIR Fluorescent lifetime imaging microscopy (SW-FLIM), Fluorescent Correlation Spectroscopy (FCS), and dip probe studies. Alongside this, I will discuss experimental plans, to combine these techniques with DAFS, STEF, and FOC while offering perspective on future experiments.

The dissertation of Anthony Vincent Sica is approved.

William M. Gelbart

Benjamin Joel Schwartz

Shimon Weiss

Justin Ryan Caram, Committee Chair

University of California, Los Angeles

2023

To my family, the family I have made along the way,

and the guileless curiosity that got me here.

TABLE OF CONTENTS

TABLE OF FIGURES

TABLES

ACKNOWLEDGEMENTS0

During my life, I often sought disorder because of how it could be an environment I thrive in. Going into graduate was something I did not have any context for. My family consists of teachers and immigrants so you can imagine their surprise when I wanted to go to graduate school. My parents were a big inspiration for this. Despite raising three children and working long hours they both fought hard to get master's degrees themselves. My mother herself would take pride over the better grades she often got than me in high school through her masters. My father came from Italy after tragedy had struck his hometown. He was a hard worker himself as he would claim an engineering degree. I thank him for the curiosity and interest in the world he gave me. My parents both didn't have much growing up, so they worked to the bone to support me and my siblings. I thank my mother for showing me true perseverance and patience. The patience she uses everyday to guide the future in special education. My mother also taught me the use in many different passions. On top of being a hard-working teacher she is also 100% muscle as she teaches fitness classes all night to save extra money.

My grandparents: my grandma, grandpa, nona, and nono often helped pick up the slack when my parents needed it. Whether it be distracting us with parades and ice cream accompanied by my Zizzi and cousins or picking me up after school and making me do the dreaded English assignments. My grandma and grandpa both passed away this year so getting through this despite the many plane rides was a trial on its own. They taught me what it is to love your family and those around me. Even through sickness my grandma called me to cheer me on. I am relieved they were able to see the love they taught me spread. To the rest of my family, I wish I could talk in detail but that's best left for words. Thank you to all my aunts, uncles, and cousins who were consistent in my life. Through the trials, you helped make me smile even if I can make it hard to

see. To Aunt Anna and Aunt Zia especially, wherever you are your desire to always bring everyone together was something I had a great fortune to see growing up.

To my dismay, I cannot continue without talking about the Oogie Boogie kids themselves, my brother and sister. Though the trivial arguments will continue to ensue now I would not be the person I am without you guys. In the end, Nicky and Tash, you will always stick through my life. I love being able play games, DnD, and even being mad with you because I know you are there. There through all the shit, through the downs, and of course the ups (and all that jazz). I leave this short cause I cannot find the words the only one I find is united. I would not have the ground I often float above without your support and love. You are the goofballs in my life, and I love you both dearly.

My family helped shape me but also the family I made along the way. To my partner in crime Ash, I know we met a little late into my graduate school, but you impacted it so greatly. I care for you so dearly. You make me laugh and make me feel at home. The time we spend feels like a fountain of joy that has no end and no sight of drying up. May our years be filled with fortune but also support for the misfortune to come. I hope you become retired in a fun way. I cannot wait to see the projects you pursue and the friends you will make. To my second soulmate and best friend Kc. The years have never knocked down the bond we have. You helped me grow and helped me find myself. Through all the foolishness and fun, we had since undergrad. Through the trials we faced together as we dragged ourselves to get out of bed and discover the world around us. Your curiosity and ambition sparked a kinship in me. You are so much more than you have always seen in yourself, I know you will become the great writer I see you as. You will **definitely** find better words than I will.

I would also like to thank Eli, Katie, and Keegan. No one knew the pain of graduate school like you guys! The memories I made as roomies and through our friendship. To the long nights of typing while playing wordle or semantle, To the foolishness we will pursue as friends and you two pursue together. The better decision of my life was introducing all of you (especially Keegan and Katie). May we continue to support each other. I would also like to thank my childhood best friend Sebass. You knew me when I didn't know me. Thank you for the nights with Dr. Who and the time we spent together. I hope your wife, Nikkie, can be just as good as a friend to me! My friends Alex, Chris, Jared, and Tom have always helped distract me through undergraduate. I may miss you guys constantly but you are always in my heart. I would also like to thank the friends who took me away from the stress through games and dumb jokes: Botai, Neel, Ben, Anne, Diego, Jae, and Trevor. You guys have always been there when I needed to not think and just laugh, thank you. Ben, I know I give you a rough time, but I know you will be resilient as a grad student.

To my lab mates and all the support, you guys have provided. As well as my committee for all the help they have given me. Especially Jman himself you will be and have been a great boss to work with and will be an even better father, especially with Diablo IV coming out. I would like to especially thank my two desk mates Prof. Timothy Atallah (Sir Luke for short) and Dr. Arundhati Deshmukh. As well as the lab aunt Jill, and the big man himself Barry. All of you have been amazing people to work with as mentors and friends. Thank you, Tim, for always pushing me even if we got annoyed at each other and thank you Anu for always guiding and inspiring me. As well as past mentors and inspirations: Prof. Scott Lefurgy and Prof. Rodney Finzel. I would like to also thank the soon-to-be Dr. Stephanie Tenney as well. We kicked ass first year together and it has been an honor working alongside you and watching you thrive as a

graduate student. Finally, of course, I thank my cats Nutella and Azrael. If I could make them coauthors, I would.

Chapters 1 and 5 contain parts from an unpublished perspective by Anthony Sica.

Chapter 2 is adopted from the published paper, “Timothy L. Atallah, Anthony V. Sica, Ashley J. Shin, Hannah C. Friedman, Justin R. Caram Decay Associated Fourier Spectroscopy: Visible to Shortwave Infrared Time-Resolved Photoluminescence Spectra.. *J. Phys. Chem. A* **2019**, *123* (301, 6792-6798. https://pubs.acs.org/doi/full/10.1021/acs.jpca.9b04924” Copyright 2019 American Chemical Society.” Experiments and data analysis: TLA, AVS, AJS; writing: TLA, AVS, AJS; editing: all authors; advising: JRC.

Chapter 3 is adopted from the published paper, “Anthony V. Sica, Ash Sueh Hua, Helen H. Lin, Ellen M. Sletten , Timothy L. Atallah*and Justin R. Caram. Spectrally-selective Time-resolved Emission through Fourier-filtering (STEF). *J. Phys. Chem. Lett.* **2023**, *14, 2,* 552-558. https://doi.org/10.1021/acs.jpclett.2c01504” Copyright 2023 American Chemical Society.” Experiments and data analysis: AVS, ASH, HHL; writing: AVS, TLA, ASH; editing: all authors; advising: JRC, TLA, EMS.

Chapter 4 is adopted from the unpublished manuscript, “Anthony V. Sica, Ash Sueh Hua, Belle Coffey, Kierstyn P. Anderson, Ben T. Nguyen, Alexander M. Spokoyny, and Justin R. Caram. Measuring the Total Photon Economy of Molecular Species through Fluorescent Optical Cycling (FOC)” Experiments and data analysis: AVS, ASH, BC, KPA, BTN; writing: AVS, ASH, BTN, BC; editing: all authors; advising: JRC.

BIOGRAPHICAL SKETCH

Education

2018 **B.S- Chemistry Minor Physics**

Hofstra University

Publications (Selected)

Timothy L. Atallah, **Anthony V. Sica**, Ashley J. Shin, Hannah C. Friedman, Justin R. Caram Decay Associated Fourier Spectroscopy: Visible to Shortwave Infrared Time-Resolved Photoluminescence Spectra. *J. Phys. Chem. A* **2019**, *123* (301, 6792-6798. https://pubs.acs.org/doi/full/10.1021/acs.jpca.9b04924" Copyright 2019 American Chemical Society."

Anthony V. Sica, Ash Sueh Hua, Helen H. Lin, Ellen M. Sletten , Timothy L. Atallah*and Justin R. Caram. Spectrally-selective Time-resolved Emission through Fourier-filtering (STEF). *J. Phys. Chem. Lett.* **2023**, *14, 2,* 552-558. https://doi.org/10.1021/acs.jpclett.2c01504" Copyright 2023 American Chemical Society

S. M. Tenney, L. A. Tan, M. L. Sonnleitner**, A. V. Sica**, A. J. Shin, R. Ronquillo, T. Ahmed, T. L Atallah, J. R. Caram "Mesoscale Quantum-Confined Semiconductor Nanoplatelets through Seeded Growth" Chem. Mater. 34 (13), 6048-6056 (2022).

Presentations

2023 Quantum Biology, Gordan Research Conference (Poster)

2022 ACS National Meeting, Chicago (Oral/Poster)

2020 Pacific Conference on Spectroscopy and Dynamics, San Diego (Poster)

2019 Seaborg Symposium (Poster)

Awards and Honors

2022 Summer Mentored Research Fellow

2022 Stones Fellowship

2018 Excellence in Advanced Organic Chemistry

2018 Excellence in Advanced Inorganic Chemistry

2018 Group Tutor of the Year

2018 Teamwork in Tutoring

2018 Long Island Chemistry Challenge, Gold

2017 NYU REU in Chemical Biology

2018 Lister Fellowship

2017 Honorable Mention Nichol's Fellowship

2014-18 Presidential Scholar

Chapter 1: Introduction to Spectroscopy Using the Emitted Photon Stream

1.1 Interface of Physical Chemistry and Measuring Photoemission

The study of physical chemistry has canonically been accomplished by introducing thermodynamic perturbations that create chemical or physical changes which are monitored in time. Through these changes, it is possible to study chemical kinetics, separate and isolate complex mixtures, and even drive chemistry to produce products ordinarily impossible to create. However, much to the dismay or delight (depending on the type of physical chemist), chemistry is not only limited to thermalized states. The introduction of optical photon energy often drives systems far out of equilibrium, and understanding the fate of excitation requires an additional set of rules dictated by electrodynamics and quantum dynamics. This was first observed in 1900, when Max Planck picked apart blackbody radiation to remedy the ultraviolet catastrophe via the introduction of quantized radiation.[1] The observation, timing, and relative phase of emitted photons allow chemists to speak and rationalize states out of equilibrium observed in photo-excited samples. The observation of single photons first occurred in the 1930's with the creation of photomultiplier tubes,[2] but it was not until 1960 that the first iteration of stimulated emission was realized.[3] The invention of pulse lasers and improved timing electronics presented an opportunity to probe specific excited states and measure the resulting time-resolved energetics as a product of the perturbation of the system by light. Within this thesis, I demonstrate examples of manipulating excitation and measuring photoemission to answer fundamental questions about physical systems.

1.2 Light-Matter Interactions

Electrons in atoms are "housed" in orbitals that have discrete energy levels.[4] The simplest two-level system describes a ground state and an excited state. When an electromagnetic field interacts with an atom, the ground state electrons may absorb the incoming field and populate a new electron configuration, nominally known as the excited state. When the charge distribution changes between the ground and excited state, the probability of light absorption is dictated by the system's transition dipole moment using Fermi's Golden Rule:[5,6]

$$\mathrm{P}'_{\mathrm{a}\to\mathrm{b}} = \frac{2\pi}{\hbar}|\langle\psi_a|\hat{\mu}|\psi_b\rangle|^2\rho(E) \tag{1.1}$$

Where $|\langle\psi_\mathrm{a}|\hat{\mu}|\psi_\mathrm{b}\rangle|^2$ is the square of the transition dipole moment, which depends on the ground and excited state dipole $\hat{\mu}$, $\hbar$ is Planck's constant, and $\rho(E)$ is the density of photon states that bridge the transition energy. A more rigorous description of light's interaction with matter can be found in many other resources.[7–10]

Initially, when a system interacts with light the atom absorbs the light and begins to populate singlet excited states. Singlet excited states will have the opposite spin of the electrons that remain in ground state. If the molecule can undergo collisions with its environment, the excited system will undergo a series of vibrational relaxation events, as well as internal conversion with other excited singlet states. Subsequently, a large population of excited state atoms will quickly relax to the ground state through several pathways which can be divided into radiative and non-radiative events. In non-radiative pathways, the decay from the excited to ground state produces no emitted light while in radiative pathways the decay results in emitted light. The radiative relaxation rate from singlet excited states to the singlet ground state is defined as fluorescence and often occurs on the scale of nanoseconds for typical organic molecules. A second pathway also occurs via

intersystem crossing where excited state electron configurations transition from the singlet state to a spin-paired triplet state close energy. The transition from singlet to triplet state is less probable due to it being "spin forbidden," yet it can occur due to coupling between the electron spin and the angular momentum of the orbitals that define the electron configuration. Because of this, the resulting radiative process, known as phosphorescence, is comparably slower than singlet to singlet transitions.[11]

As will be demonstrated below, these radiative processes may be studied through different means. For example, to begin to understand the energetics of the sample system, the transition from ground to excited state is measured through absorption spectra. Following this, the radiative relaxation events that proceed are measured through emission spectrum and are typically measured with a fluorimeter. This process involves sample excitation with a lamp or laser where the resulting emission components are split using a diffraction grating. The resulting spectra is dispersed onto a detector. The combination of absorption and emission spectra help to understand the energetics within the different states of the molecular system.[11] Another common approach is studying the time of relaxation after light stimulation.[12] After the absorption event of a molecule, the excited electronic state decay or lifetime of the system can be observed through time-resolved methods.[13] The decay will often be modeled as a series of exponentials convolved with the instrumental response function of the detector/excitation source.[11] There are a variety of methods that measure the timed event and others that measure the emission spectra. However, few systems exist that can measure both the time and energetic properties of a system without the use of grating monochromators.[13]

1.3 Laser Fundamentals

The term Laser stands for Light Amplification by Stimulated Emission of Radiation. Selection of a light source in spectroscopy is paramount to an instrument's design. Before the implementation of lasers, the light sources used for spectroscopy-based experiments were limited to arc lamps, tungsten halogen lamps, and sources of blackbody radiation.[14] Even celestial bodies such as the sun were used as spectroscopic light sources.[14] However, because of the stochastic nature of photon generation in such sources, the emitted radiation lacks temporal coherence. Optical coherence is the ability for light waves to be consistently in phase with one another across large distances and long times.[15] Lasers retain coherence which allows for more sophisticated light manipulations, such as ultrafast pulsing and interferometric control. These light sources work in a very different manner than typical gas lamps, through a process called stimulated emission.

We described spontaneous emission in section 1.2, but lasers work through a related radiative process known as stimulated emission.[16] In stimulated emission, an excited state interacts with an external electric field that matches the energy difference between it and its ground state resulting in the emission of a photon in the same direction, phase, and energy as the incoming photon. Stimulated emission is an amplification process where one photon is fed into the system and two coherent photons are produced. This process is unlikely to happen thermally for optical transitions, due to the large energy gaps between ground and excited state. To drive a laser, the population of the excited states must be greater than the population of the ground state, an event known as population inversion. Lasing materials are chosen where excitation can transfer electrons from a short-lived excited state into a long-lived lower energy metastable state. In that longer-lived state the population is shelved and over time to reach an occupancy considerably greater than the ground state resulting in an overall net amplification of stimulated emission or a

lasing event.[17] This process may also be enhanced through the implementation of multi-state lasers. The introduction of extra states removes the competition between the repleting excitation into the meta-stable state and the depleting stimulated emission out of the meta-stable state.

Lasers are created using an optical cavity; this consists of two mirrors: one maximumly reflective and one that fractionally transparent. The initial excited-state atoms of the gain media emit photons in many random directions and in many different phases. Some photons that emit in the direction of the cavity (also known as “seed” photons) are then continuously reflected through the gain media. With each pass through the gain media, the intensity and number of coherent photons increases. Laser output then occurs as a small amount of coherent light transmits through the fractionally transparent mirror. The remaining light remains in the cavity to continue the process.

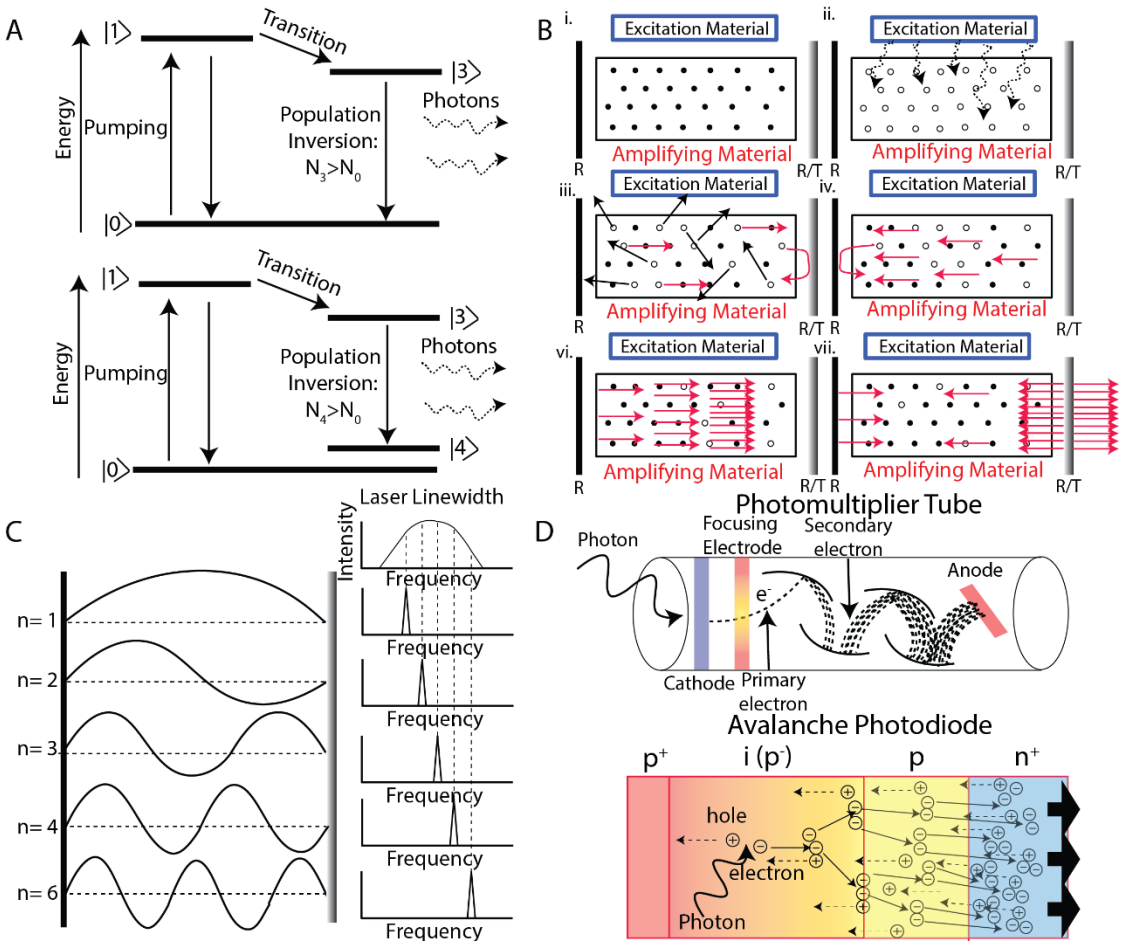

Figure 1.1 Laser Operation and Single Photon Detection

A. Two and three state laser system that depicts the principles of population inversion. B. Process of pumping a gain medium continually until amplification results in lasing through the partially transmitting mirror. C. Series of longitudinal modes that constructively interfere creating output frequencies. The modes transmit through the mirror making a series of frequencies that will make the overall linewidth. D. Single photon counting devices: photomultiplier tube (PMT) and avalanche photodiode (APD). PMTs will use a long tube to focus an electron and build of charge to create voltage that can be read as a photon. APDs operate using p-n junction set to near the breakdown voltage, which results in creates a large enough electric field that leaves the APD on the edge of an avalanche event. Light stimulus then creates an avalanche increasing the electrons (n-side) that accelerate to the holes (p-side). This movement of electrons causes a swift rise in current change. Once the current exceeds a signal threshold a photon event is registered Figures A-C adapted[17]

1.4 Pulsed Lasers

Lasers can either be engineered to be continuous wave in which the photon intensity remains constant or to be pulsed wave in which light arrives in bunched packets. The use of pulsed lasers offers an advantage by initiating and measuring temporal dynamics. Pulsed lasers allow for faster timing resolution because they offer short periodic bursts with up to attoseconds pulse width. However, there is a tradeoff, short pulses lose wavelength specificity in excitation.[18] The bandwidth of laser is set by the gain media and quality of the cavity (Q-factor).[19] Along with the ability to stimulate the system in fast repetition, often set by the length of cavity, pulsed lasers achieve repetition rates on the order of megahertz to a few gigahertz. Gigahertz lasers can achieve their fast repetition rates by leveraging techniques such as electro-optic combs,[20] mode locking solid state lasers,[21] and micro resonator combs.[22,23] Both CW and pulsed lasers operate on the same principle in that they are pumped and cycled through a gain medium paired with a cavity to produce a laser output.

Pulses can be formed through two main mechanisms: mode locking and Q-switching. Achieving up to femtosecond pulses, mode locking lasers leverage the fixed phases within the laser cavity to create constructively interfering longitudinal modes. Q-switching, on the other hand, results in higher energy pulse but has much lower repetition rates and longer pulse duration. Q-switching modulates the Q-factor of the cavity with the use of an attenuator. While the switch is closed, the medium will continue to undergo continuous stimulated emission until the population number no longer increases resulting in a saturation of intensity. Once saturated the attenuator is shut off, allowing feedback in the cavity to occur once more. As a result, a high energy laser pulse exits the system.[12] We apply to principle later in the thesis when discussing fluorescence optical cycling (FOC). Here singlet states are continuously excited with some population crossing to longer lived

triplet states. The pumping continues until a similar saturation is reached. After this, the pumping is stopped, and the decay of longer-lived states can be observed.

1.5 Single Photon Detection

The implementation of pulsed lasers allows light-induced dynamics to be observed because of its ability to initiate time-resolved photoemission events. With modern electronics, the deterministic timing of laser pulses has improved to the point where it is possible to record photon events such as photoluminescence at picosecond resolution. With this, the system's "total photon economy" can be measured. In other words, the resulting photon stream can be observed as a function of photon in (the laser excitation) vs photon out (system response). Several detections schemes allow for the detection of single photons and operate using similar principles.

Physical Limits of Detection

There are many important aspects to consider when discussing the characteristics of photon detectors. To begin, one should consider the quantum efficiency of the device or its ability to convert single photons to detectable charge cascades. Many things can influence this, including the properties of the material, such as the band gap of the semiconductor used in detection. Additionally, engineering aspects in the device such as device thickness and the reflection and transmission of the area of detection play a part in device efficiency. Along with quantum efficiency, spectral response should also be considered. Different detectors have different quantum efficiencies across the electromagnetic spectrum which can limit broadband capability. Another significant device property is the noise inherent to the devices. One major contribution to noise is described as dark counts. Dark counts are registered as false photon counts that are a product of excess heat in the system exciting charge carriers either from trap states or across the bandgap.

More dark counts will result in more noise, making this increasingly difficult to distinguish low fluence signals from noise. Device dark counts are usually sensitive to environmental conditions such as the temperature of the detectors.[24] Additionally, defects in the material, either intrinsic to the fabrication process or as a result of damage from prolonged light radiation contribute to higher dark counts.[25] Because of the design of single photon detectors, detection is limited to measuring one photon event at a time. Many detection schemes have a reset time, or an amount of time needed to restore to equilibrium before another photon can be detected. Shorter reset times are desirable to minimize the loss of photon events but come with tradeoffs due to afterpulsing. Finally, there is the timing jitter of the electronics within the detection scheme. Jitter is described as the deviation of a signal produced from a system to the true event of the impulse on the system.[26] With something as temporally resolved as single photon counting, variations from jitter can lead to more statistical uncertainty. The innate width of a signal, or the instrument response function, can also be largely affected by jitter.

Single Photon Detectors

Examples of such single photon detectors are photomultiplier tubes (PMTs) and photodiodes (PD). The work done in this thesis uses the common silicon avalanche photodiode (APD) detector for detecting visible light. Recent advances have allowed for the use of superconducting nanowire single photon detectors (SNSPDs) to measure longer wavelengths (>900 nm) which will be discussed in its own section. Avalanche photodiodes (APDs) are comprised of semiconducting materials, (e.g. silicon) that leverages avalanche breakdown to detect a photon event. The APD consists of a p-n junction that operates by applying a high reverse bias voltage. The large reverse bias creates a large enough electric field that leaves the APD on the edge of an avalanche event.[27] When a photon hits the detector this avalanche begins, exponentially increasing the electrons (n-

side) that accelerate to the holes (p-side). This movement of electrons causes a swift rise in current. Once the current exceeds a signal threshold a photon event is registered. By lowering the bias, the ability for recombination events is then halted which swiftly quenches the avalanche.[28] The bias is then raised above breakdown once more in order to detect the photon. The time of quenching to regaining this steady breakdown voltage dictates the reset time, or the time after a photon event before another photon can be detected. APDs offer the advantage of high quantum efficiencies, lower jitter, and less dark counts than PMTs.[29] Furthermore the gain required for APD operation is not as large as PMTs, leading to simpler operation. However, the active area of a PMT is significantly larger because an avalanche breakdown occurs across several microns. APDs excel in spectral broadband measurements which require sensitive detection, low electronic noise, and low signal gain, but PMTs are preferred for large-area detection.[30–32]

Advantages and Disadvantages of Single Photon Counting

Single photon counting leverages many advantages such as the elimination of gain noise and improvement in temporal resolution. The resolution can reach picoseconds because the act of measuring single photon results in single signal impulse events. In non-single photon detection schemes many photons are detected at once, causing an overlap in the response seen in the detector. This can limit the temporal resolution to that of the fall time in the signal of detection. However, a limitation of single photon detectors is their reset times, which limits the speed at which a signal can be detected. Longer reset times make it difficult to distinguish photon events that are temporally nearby or reach the limit of the detector's rest time. Additionally, the longer reset times limit the maximum count rate that can be detected. As a result, single photon measurements are usually performed with a smaller number of photons. Unlike conventional detection, single photons become reliant on photon statistics and shot noise resulting in a lower

contrast signal to noise. Single photon detectors are also more sensitive to temperature, with higher temperatures will result in a decreased gain and less sensitivity.

1.6 Superconducting Nanowire Single-Photon Detectors (SNSPDs)

To measure photons beyond the bandgap of silicon, the shortwave infrared (SWIR: 1000-2000 nm), requires different technology. The SWIR region is considered "spectrally quiet" because few molecules absorb and emit into the SWIR. In addition, imaging in the SWIR region has improved contrast due to decreased scattering. These advantages make SWIR materials useful for imaging with little background from autofluorescence and through scattering environments such as fog, foliage, and biological material.[33–35] Furthermore, the lower noise interference also makes this window ideal for telecommunications. However, a challenge in SWIR imaging is the low quantum yield associated with the materials that emit in this region.[36]

There are a few materials that accommodate SWIR detection which examples being Germanium (Ge), Indium Gallium Arsenide (InGaAs), Indium Antimonide (InSb), and Mercury Cadmium Telluride (MCT).[37] Lattice matched InGaAs/InP detectors are most common due to their comparably higher device quantum efficiencies and low dark counts at room temperature. In recent years, the use of superconducting nanowire single-photon detectors (SNSPDs) has begun to outperform InGaAs/InP detectors. With remarkably low timing jitter,[38] quantum efficiencies of near unity,[39] and sub-ps resolution[40] SNSPDs are among the fastest photon detectors at nearly any wavelength.[41]

Principles of Operation

SNSPDs are comprised of an array of superconducting nanowires bundled into a compact geometry. The wires are cooled (in our case to around 2.25 K) to below superconducting critical

temperature where a bias current close to critical current is applied. The basic principle on the operation of SNSPDs is still debated. One argument is that the nanowire undergoes a Kosterlitz–Thouless Transition during photon absorption.[42,43] Here, the photon impinging on an SNSPD creates a vortex-antivortex pairs. Vortex-antivortex pairs are bound quasi-particles of two spin orientations (Figure 1.2B). As the wires are heated, pair generation begins to increase until a critical temperature is reached. At this temperature the pairs will unbind or break apart.[44–46] Two possible mechanisms follow. The first being, that the absorption of photon creates an increase in the density of vortex-antivortex pairs. Then, as a result of the wire's current a Lorentz force begins to pull at the pair*s* in opposite directions. The force reaches a critical point where the pair*s* are separated*,* breaking super conductance. The second mechanism is that a photon impinges upon the wire creates a hot spot. This hot spot decreases the energy barrier necessary for the pair to travel across the wire. However, alternate studies suggest that the second argument*'s* main mechanism is drive by the breaking of cooper pairs in local hot spots instead *of* the vortex pairs.[47] Cooper pairs are electron pairs that are intrinsically responsible for superconductivity.

All the different mechanisms*'* principles ultimately end similarly, with result a single photon temporarily breaking super conductance in the nanowire. The spike in resistance creates a small but measurable change in voltage which is amplified and registered as a photon event. The fast reset time is set by the wire cooling and regaining superconducting character. In this thesis, we use SNSPDs in tandem with silicon APDs to take broadband measurements from visible to SWIR.

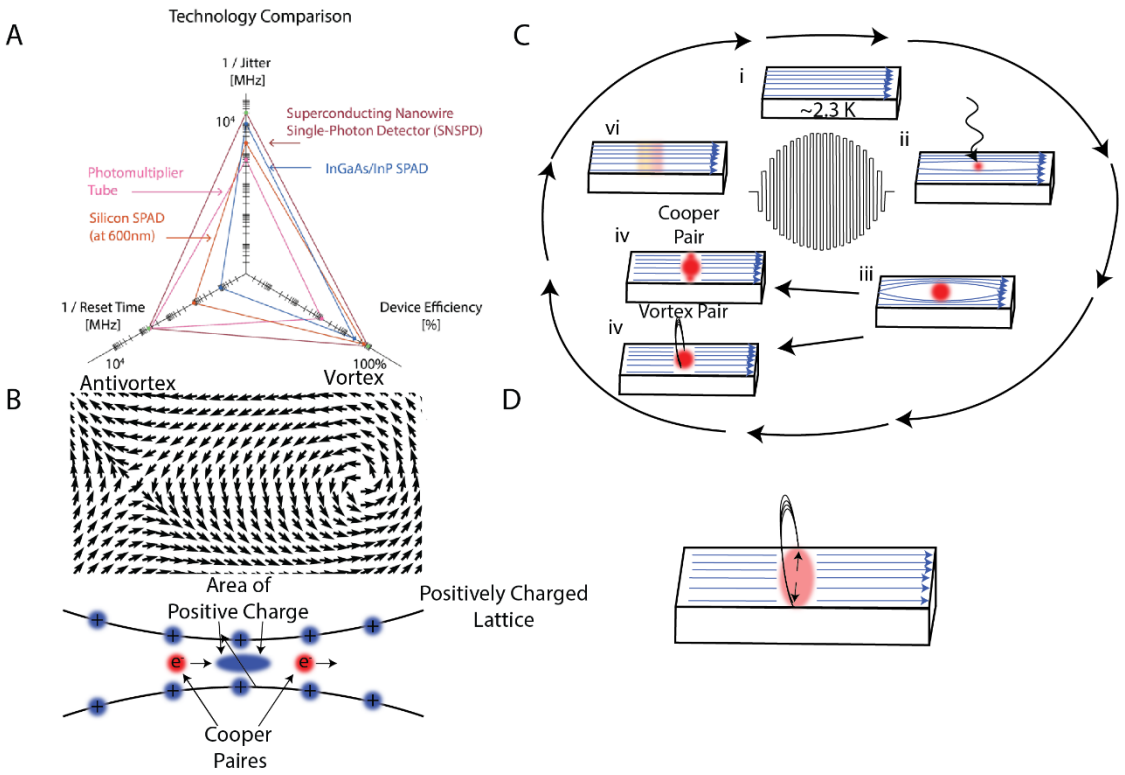

Figure 1.2 Operation of SNSPDs

A. Comparison of single photon detectors. As seen SNSPDs have the fastest reset time, lowest jitter, and highest device efficiency. B. Examples of vortex-antivortex pairs (top) in which the heat of the system perturbs the spin. As spin continues to orient itself it assumes the lower energy vortex (right) and antivortex(left) configuration. Along this is a representation of cooper pairs (bottom) in which a positive lattice creates an area of positive attraction that attracts electrons in the same direction causing a binding of electrons. C. SNSPD operation as a photon event occurs on the nanowire. The nanowire is spun in a circular geometry to maximize surface area. i) As the SNSPDs are idle at supercooled temperatures (~2.3 K) they maintain super conductance. ii) A photon fiber coupled through impinges on the nanowires creating a local hot spot. iii) This local hot spot begins to break super conductance creating a local point of resistance. iv) The local spot of resistance creates a spike in the voltage in which a photon event is registered. This hotspot is still debated if it breaks cooper pairs or vortex-antivortex pairs. vi) Dictating the rest time, the super conductance begins to relax back to equilibrium. D. An alternate mechanism of vortex-antivortex in which the photon splits the vortex-antivortex pairs unbinding the two and breaking super conductance.

1.7 Single Photon Statistics

When collecting single photons, it is important to understand how to extract information from the photon stream. Typically, when averaging over an ensemble intensity of light, one can derive the intensity as a square of the electric field:

$$\mathrm{I(t)} = |\varepsilon(\mathrm{x,t})|^2 \ = \varepsilon_0 \sin\left(\mathrm{kx} - \omega\mathrm{t} + \phi\right) \tag{1.2}$$

Where an electric field $\varepsilon(x,t)$, is equal to the amplitude, ε_0, multiplied by a wave form containing variables for angular frequency, ω, phase, ϕ, and the wave vector, k, where $\mathrm{k} = \frac{\omega}{\mathrm{c}}$. Because photons are discrete and indivisible for any given time, their arrival time must be distributed in random intervals with non-integer photon numbers impossible as seen in Figure 1.3A. Because of this, when we look at a time averaged intensity and at shorter time scales the photon arrival exhibits interesting and statistically determined arrival times. Adapting a derivation from reference [48] we can begin by considering a light of constant power across a beam of length L. We describe the number of average photon number as:

$$\langle n \rangle = \frac{\phi L}{c} \tag{1.3}$$

When we span across large enough L the average number of photons, $\langle n \rangle$, approaches integer values. Now let us divide the overall photon stream into subsections, N. The probability of finding a photon within each subsection N, becomes a binomial distribution:

$$\mathrm{P(n)} = \sum_{n=0}^{N} \binom{N}{n} p^n (1-p)^{N-n} \tag{1.4}$$

Where $\mathrm{p} = \frac{\langle n \rangle}{N}$. After, the use of the Stirling formula and equation manipulation equation 1.4 will become:

$$\mathrm{P(n)} = \sum_{n=0}^{N} \frac{\langle n \rangle^n}{n!} \left(1 - \frac{\langle n \rangle}{N}\right)^{N-n} \tag{1.5}$$

Where $\sum_{n=0}^{N} \left(1 - \frac{\langle n \rangle}{N}\right)^{N-n}$ resembles an exponential expressed as summation making equation 1.5:

$$\lim_{\mathrm{N}\to\infty} [P(n)] = \frac{1}{n!} \langle n \rangle^n exp(-\langle n \rangle) \tag{1.6}$$

Finally, this equation arrives us at:

$$\mathrm{P(n)} = \frac{\langle n \rangle^n}{n!} exp\ (-\langle n \rangle^n) \quad \mathrm{n} = 0,1,2,3\ldots. \tag{1.7}$$

Which is the definition of Poisson distributions. As single photons are produced, they follow this distribution which yields the probability of photon events with finite integers representing photon number. The nature of the photon stream following this distribution also leads to the consequence of the variance being the variance of a Poisson distribution where:

$$\mathrm{Var(n)} = \Delta n = \sqrt{\langle n \rangle} \tag{1.8}$$

Equation 1.8 elucidates the signal to noise of single photon counting where the uncertainty of the measurements is the square root of the photon counts. This is also the origin of the random photon fluctuations we see in the detectors known as shot noise.

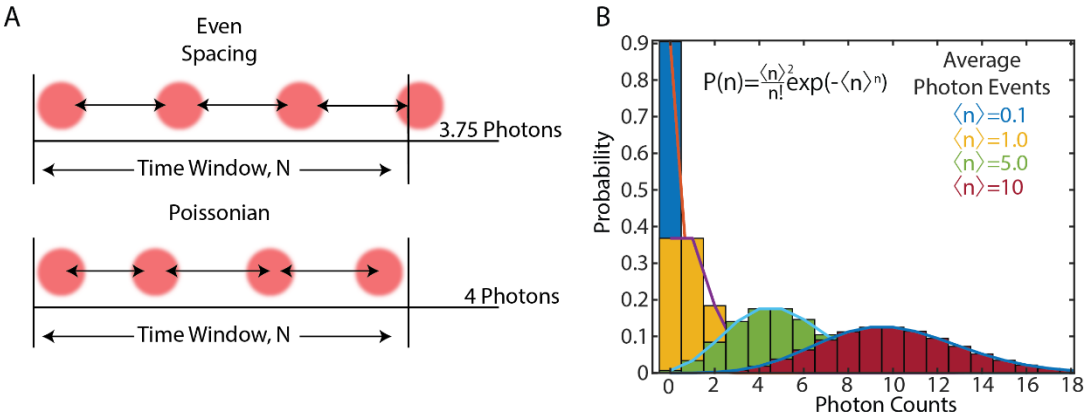

Figure 1.3 Photon Statistics

A. Pictorial representation demonstrating the discrete properties of single photon counting. Evenly spaced photons would yield non integer photons across time window N. For this reason, photons follow a Poissonian distribution. The probability distribution unevenly spaces the photons so that every event is an integer value. B. Poissonian photon counts as mean value increases**.**

1.8 Time Correlated Single Photon Counting (TCSPC)

With the current toolset described above many time-resolved experiments are feasible with hardware to accurately record the timing events of photons. Here we utilize Time Correlated Single Photon Counting (TCSPC), a sophisticated system for high timing precision of photon events. Constant Fraction Discriminators (CFD) are utilized to extract timing information from electrical detector pulses. The signal is then fed into a Time to Digital Converter (TDC) that leverages time differences using the delay of signals in semiconductor logic gates such as Field Programmable Gate Arrays (FPGAs). The delays are fed into the TCSPC registering photon events with fast timing responses relative to laser pulses.[48]

When collecting a TCSPC trace, the simplest experiment uses a pulsed laser to excite a sample and a single photon detector collects the emission. On every laser a pulse, a sync signal is sent to the TCSPC unit marking a start time. In the case of a photon event, the detectors will then send a signal to the TCSPC unit as time relative to the sync event. The TCSPC unit throughout the studies

here is a HydraHarp. The photon times are then histogrammed with the maximum binning in the HydraHarp being 65,565 (16 bits) and the bin width set 1 picosecond at a minimum.

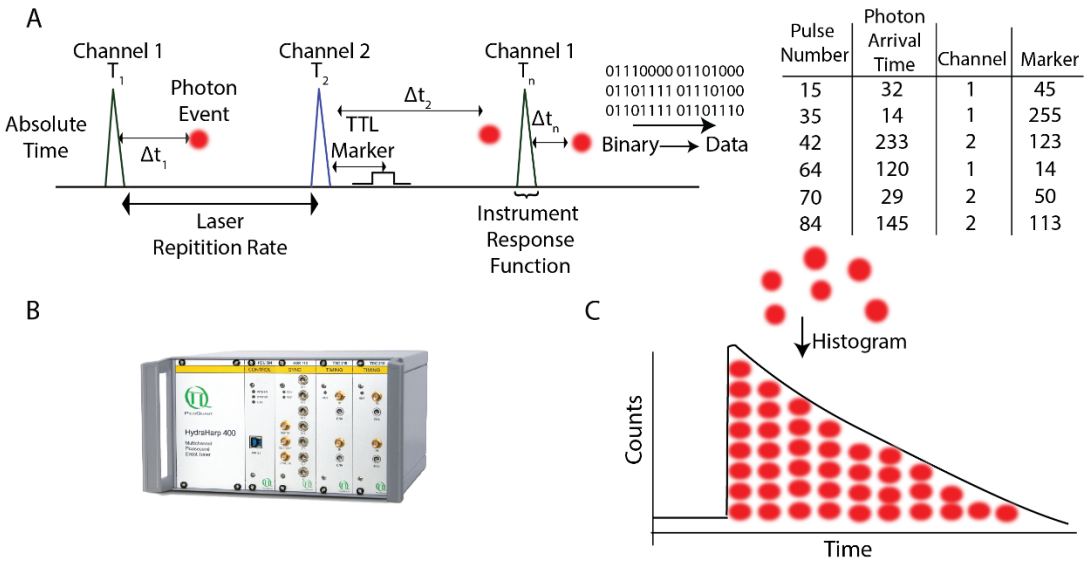

Figure 2.4 TCSPC Collection

A. Pictorial representation of the collection of the photon stream using TTTR mode. Each laser sync corresponding to a photon event, the bin of the photon event timed relative to the laser pulse, channel number, and marker are stored into a binary file. This as well as metadata of the experiment is then translated from binary into a list of all these parameters constructing the photon stream which can be used later for multiple purposes such as reconstructing the lifetime via histogramming**.** B. The HydraHarp 400 sold by Picoquant and is used in all the following experiments. C. Pictorial representation of a histogrammed photon events that yield a lifetime curve.

1.9 Time-Tagged Time-Resolved Mode (TTTR)

One can also go beyond histogramming photon arrival times. In Time-Tagged Time-Resolved Mode (TTTR), all timing events that occur within the experiment can be recovered. When acquiring data in TTTR, a list of all pulse numbers, relative photon time compared to the pulse, channel numbers, and external signal markers is collected. With the photon stream, much more complicated methods can be implemented such fluorescent lifetime imaging (FLIM) and newer

methods described in later chapters. In TTTR mode the resulting data can be processed and manipulated to gain more insight on the photophysical events occurring beyond lifetimes.

1.10 Interferometry

As alluded above, the ability to send in and collect coherent light in collection allows for flexible manipulation of photons in time and space. One such method utilized across disciplines is interferometry. In interferometry, the electric field is split and superimposed to decipher information about the system through comparison of relative phase and timing of the detected light. Manipulation of the phase can be done through the inclusion of translational stages and optical components of varying thicknesses and/or refractive indices that increase the path of the light. The overlapping of light begins to interfere constructively and destructively, resulting in the overall intensity increasing and decreasing. The fluctuations are known as fringes and can tell a multitude of things about the light such as linewidth given by the coherence length of the interference.[49] Another common implementation uses the interference to measure energy of the incoming emission by using the frequency of the incoming fringes. A common example of the latter approach is Fourier transform infrared spectroscopy (FTIR) in which the interference helps examine vibrational resonances in molecules.[50]

Interferometers can be split into two main categories: ones that split wavefronts and others that split overall amplitudes. Wavefront splitting interferometers take waves from a point source and then split the incoming field into wavefront components. The wavefronts interfere as they travel through space and the resulting interference pattern is collected. An example of this being Young's two-slit experiment (Figure 1.5A) in which the wavefront is separated with the use of slits.[51] The interferometer discussed in the following thesis is a double-path amplitude-splitting

interferometer. In this scheme, light is split using a reflective optic such as a beam splitter. The two subsequent paths or "arms" of the interferometer travel in space and then recombine introducing interference. Interference is then collected by scanning across position space.

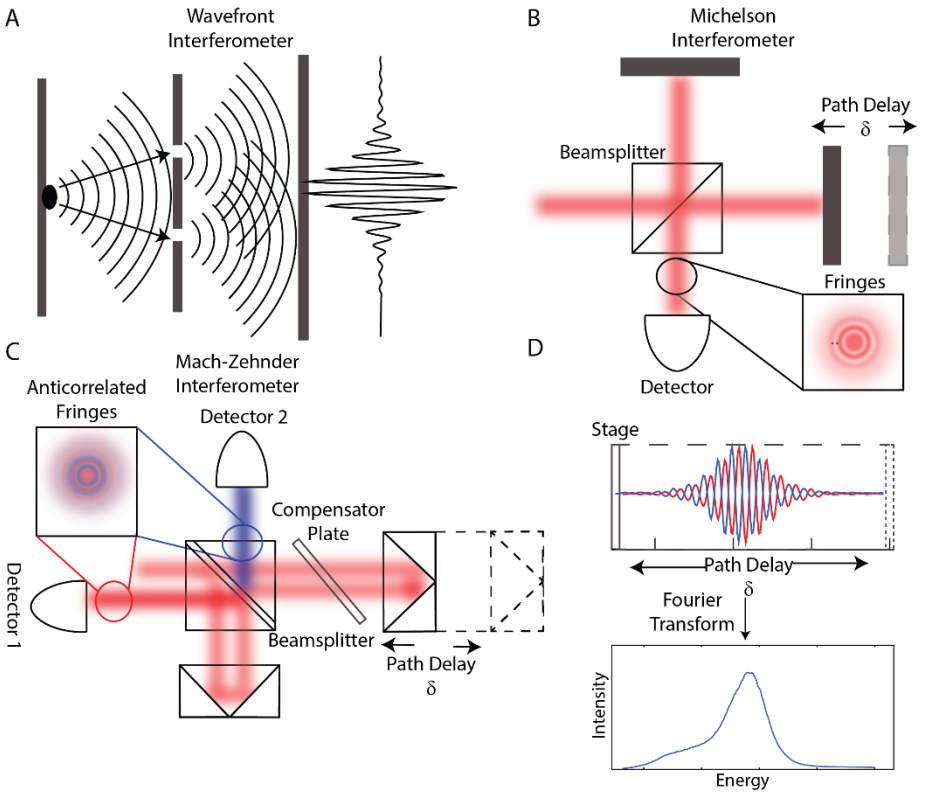

Figure 1.5 Interferometry

A. Example of a wavefront interferometer such as the one used in Young's two-slit experiment. Here a point is split into two separate waves that interfere in space creating an interference pattern. B-C. Instances of amplitude-based interferometry where light is split using a beam splitter to separate the radiation into a static and dynamic arm. One arm will change the phase relative to the other and the two are then recombined. In Michelson (B) they are recombined the same beam splitter that divided the stream in the first place. In Mach-Zehnder(C) they are recombined on a second beam splitter. This offers the advantage of anticorrelated signals collected on two detectors. Which provides the ability to remove random noise, drift, and leverage balanced detection. D. A sample signal that is collected as the stage translates. The signal is then Fourier Transformed from position space to energy space yielding an emission spectrum.

An example of amplitude-splitting interferometer is the Michelson interferometer (Figure 1.5B) where light is split using a beamsplitter. One path changes the delay of light, and the two divided paths are then subsequently recombined on the same beam splitter. In the following thesis, a folded Mach-Zehnder interferometer (Figure 1.5C) is used to perform spectroscopy. The difference being that the light is recombined on a second beam splitter allowing for the use of two detectors after the second beam splitter. The resulting anticorrelated interferences can then be used to cancel random noise and drift in the signal (Figure 1.5D). In addition, Mach-Zehnder allows small fluctuations to be measured across detectors allowing for cross-correlations as well as balanced detection. In this thesis, I take advantage of Mach-Zehnder interferometry whose benefits are discussed in more depth in later chapters.

The Fourier Transform

Interferometry utilizes the principles of Fourier Transforms to collect energetic information from the sample. To simplify, a Fourier Transform takes the data collected in position space and transforms it into the inverse space. In this case, the inverse of position is energy or frequency of the signal. This subsequently leads to an emission spectrum. The Fourier transform is of the following form:

$$f(\nu) = \int_{-\infty}^{\infty} f(x) e^{-i2\pi\nu x} dx \tag{1.2}$$

Where ν is the frequency and x is the position. The inverse may be used as well to transform frequencies back to positions, this is leveraged as a filtering method we call STEF seen in Chapter 3. The real component of the Fourier transform can be thought of as a sum of cosine frequencies while the imaginary phase components can be found in a series of sine frequencies. The real sums of frequencies produce the desired emission spectrum while the imaginary sums describe the phase

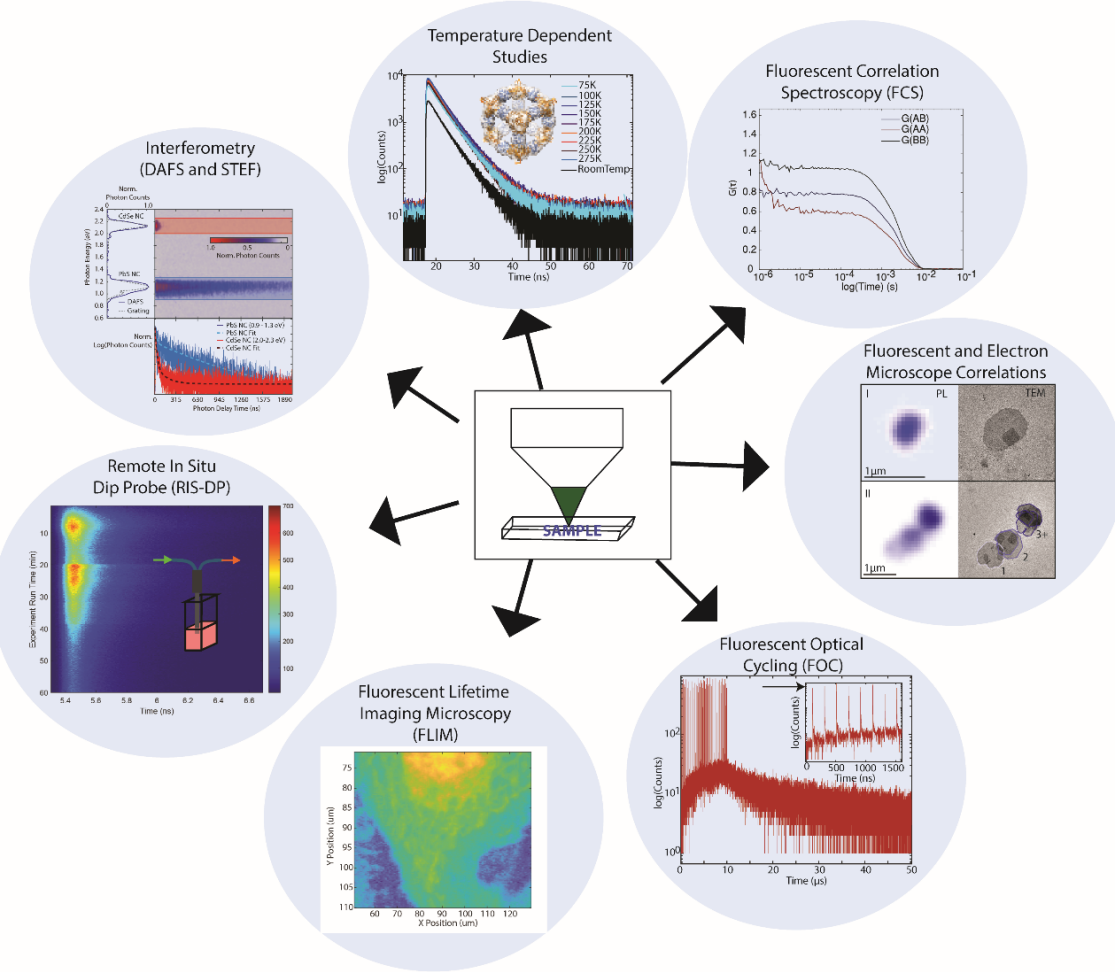

Figure 3.6 Summary of Projects

Graph demonstrating the extent of single photon counting and methods developed that will be elaborated more upon in the thesis

of the incoming field. Interferometry is combined in tandem with TCSPC to collect time and energetic information of a sample. This offers an alternative to diffraction based TCSPC-emission collection, foregoing diffraction artifacts that may occur across broadband collection.

1.11 Summary

A short summary of all experiments can be found in Figure 1.6. DAFS can be found within the second chapter, followed by STEF in the third, and FOC in the fourth. The rest of the techniques are discussed briefly with preliminary data in the final chapter.

References

1. Planck, M. The Theory of Heat Radiation. in *Waermestrahlung* (ed. P. Blakiston's Son & Co.) (The Maple Press York, 1913).

2. Bienfang, J., Fan, J., Migdall, A. & Polyakov, S. V. Single-Photon Sources and Detectors Book: Chapter 1: Introduction. (2013).

3. Physics History: Maiman Builds First Working Laser. *APS News* **19**, (2010).

4. Griffiths, D. J. & Schroeter, D. F. *Introduction to quantum mechanics*. (Cambridge University Press, 2019).

5. Dirac, P. A. M. & John', S. The Quantum Theory of the Emission and Absorption of Radiation. *Proc. Roy. Soc* **114**, 243.

6. Orear, Jay., Fermi, E., Rosenfeld, A. H. & Schluter, R. A. Nuclear physics : a course given by Enrico Fermi at the University of Chicago. 248 (1974).

7. Fox, M. (Anthony M. Quantum optics : an introduction. 378 (2006).

8. Scully, M. O. & Zubairy, M. S. 1997 Scully Zubairy Quantum Optics. (2007).

9. Mandel, L. & Wolf, E. Optical Coherence and Quantum Optics | Optics Optoelectronics and Photonics | Cambridge University Press. 1194 (1995).

10. Walls, D. F. & Milburn, G. J. Quantum Theory of the Laser. *Quantum Optics* 231–246 (2008) doi:10.1007/978-3-540-28574-8_12.

11. Introduction to Fluorescence. *Principles of Fluorescence Spectroscopy* 1–26 (2006) doi:10.1007/978-0-387-46312-4_1.

12. Paschotta, R. *Field Guide to Lasers | (2008) | Paschotta | Publications | Spie*. vol. FG12 (SPIE Press, 2008).

13. Metzger, W. K. *et al.* Conference Paper Time-Resolved Photoluminescence and Photovoltaics. (2004).

14. Brand, J. C. D. Lines of light: The sources of dispersive spectroscopy, 1800-1930. *Lines of Light: The Sources of Dispersive Spectroscopy, 1800-1930* 1–266 (2017) doi:10.1201/9780203748862/lines-light-brand.

15. Mandel, L. & Wolf, E. Optical Coherence and Quantum Optics | Optics Optoelectronics and Photonics | Cambridge University Press. 1194 (1995).

16. Einstein, A. Zur quantentheorie der strahlung. *Physikalische Zeitschrift* **18**, 121–128 (1917).

17. Kolluri, R. Fundamentals of Light and Lasers, 3rd Edition – LASER-TEC. in *Fundamentals of Light and Lasers* vol. 6 (OP-TEC, 2018).

18. Backus, S., Durfee, C. G., Murnane, M. M. & Kapteyn, H. C. High power ultrafast lasers. (1998).

19. Keller, U. *Ultrafast Lasers*. (Springer International Publishing, 2021). doi:10.1007/978-3-030-82532-4.

20. Mizutori, A. *et al.* Phase-noise characteristics of a 25-GHz-spaced optical frequency comb based on a phase- and intensity-modulated laser. *Optics Express, Vol. 21, Issue 24, pp. 29186-29194* **21**, 29186–29194 (2013).

21. Heinecke, D., Bartels, A. & Diddams, S. A. Passively mode-locked 10 GHz femtosecond Ti:sapphire laser. *Optics Letters, Vol. 33, Issue 16, pp. 1905-1907* **33**, 1905–1907 (2008).

22. Del'Haye, P. *et al.* Optical frequency comb generation from a monolithic microresonator. *Nature 2007 450:7173* **450**, 1214–1217 (2007).

23. Endo, M. *et al.* Direct 15-GHz mode-spacing optical frequency comb with a Kerr-lens mode-locked Yb:Y_2O_3 ceramic laser. *Optics Express, Vol. 23, Issue 2, pp. 1276-1282* **23**, 1276–1282 (2015).

24. Itzler, M. A. *et al.* Single photon avalanche diodes (SPADs) for 1.5 μm photon counting applications. *https://doi.org/10.1080/09500340600792291* **54**, 283–304 (2007).

25. Wilson, B. A., Miloshevsky, A., Hooper, D. A. & Peters, N. A. Radiation-Induced Dark Counts for Silicon Single-Photon Detectors in Space. *Phys Rev Appl* **16**, 064049 (2021).

26. Maichen, Wolfgang. Digital timing measurements : from scopes and probes to timing and jitter. 240 (2006).

27. Haitz, R. H. Mechanisms Contributing to the Noise Pulse Rate of Avalanche Diodes. *J Appl Phys* **36**, 3123 (2004).

28. Cova, S., Longoni, A. & Andreoni, A. Towards picosecond resolution with single-photon avalanche diodes. *Review of Scientific Instruments* **52**, 408 (1998).

29. Wong, T.-H. *et al.* Sensitive infrared signal detection by upconversion technique. *https://doi.org/10.1117/1.OE.53.10.107102* **53**, 107102 (2014).

30. McInTyre, R. J. Multiplication Noise in Uniform Avalanche Diodes. *IEEE Trans Electron Devices* **ED-13**, 164–168 (1966).

31. Brown, R. G. W., Rarity, J. G. & Ridley, K. D. Characterization of silicon avalanche photodiodes for photon correlation measurements. 1: Passive quenching. *Applied Optics, Vol. 25, Issue 22, pp. 4122-4126* **25**, 4122–4126 (1986).

32. Teich, M., Matsuo, K. & Saleh, B. Excess noise factors for conventional and superlattice avalanche photodiodes and photomultiplier tubes. *IEEE J Quantum Electron* **22**, 1184–1193 (1986).

33. Hong, G., Antaris, A. L. & Dai, H. Near-infrared fluorophores for biomedical imaging. *Nature Biomedical Engineering 2017 1:1* **1**, 1–22 (2017).

34. SPIE, P. of. Front Matter: Volume 8889. *Sensors, Systems, and Next-Generation Satellites XVII* **8889**, 888901 (2013).

35. Carr, J. A., Valdez, T. A., Bruns, O. T. & Bawendi, M. G. Using the shortwave infrared to image middle ear pathologies. *Proc Natl Acad Sci U S A* **113**, 9989–9994 (2016).

36. Wan, H., Du, H., Wang, F. & Dai, H. Molecular imaging in the second near-infrared window. *Adv Funct Mater* **29**, (2019).

37. Hansen, M., Malchow Marc Hansen, D. P., Malchow, D. S. & Hansen, M. P. Overview of SWIR detectors, cameras, and applications. *https://doi.org/10.1117/12.777776* **6939**, 94–104 (2008).

38. Vodolazov, D. Y., Manova, N. N., Korneeva, Y. P. & Korneev, A. A. Timing Jitter in NbN Superconducting Microstrip Single-Photon Detector. *Phys Rev Appl* **14**, 044041 (2020).

39. Reddy, D. V. *et al.* Superconducting nanowire single-photon detectors with 98% system detection efficiency at 1550 nm. *Optica, Vol. 7, Issue 12, pp. 1649-1653* **7**, 1649–1653 (2020).

40. Korzh, B. *et al.* Demonstration of sub-3 ps temporal resolution with a superconducting nanowire single-photon detector. *Nature Photonics 2020 14:4* **14**, 250–255 (2020).

41. Vetter, A. *et al.* Cavity-Enhanced and Ultrafast Superconducting Single-Photon Detectors. *Nano Lett* **16**, 7085–7092 (2016).

42. Kosterlitz, J. M. & Thouless, D. J. Ordering, metastability and phase transitions in two-dimensional systems. *Journal of Physics C: Solid State Physics* **6**, 1181 (1973).

43. Halperin, B. I. & Nelson, D. R. Resistive transition in superconducting films. *J Low Temp Phys* **36**, 599–616 (1979).

44. Bulaevskii, L. N., Graf, M. J., Batista, C. D. & Kogan, V. G. Vortex-induced dissipation in narrow current-biased thin-film superconducting strips. *Phys Rev B Condens Matter Mater Phys* **83**, 144526 (2011).

45. Zotova, A. N. & Vodolazov, D. Y. Photon detection by current-carrying superconducting film: A time-dependent Ginzburg-Landau approach. *Phys Rev B Condens Matter Mater Phys* **85**, 024509 (2012).

46. Kadin, A. M., Leung, M. & Smith, A. D. Photon-assisted vortex depairing in two-dimensional superconductors. *Phys Rev Lett* **65**, 3193 (1990).

47. Kadin, A. M. & Johnson, M. W. Nonequilibrium photon-induced hotspot: A new mechanism for photodetection in ultrathin metallic films. *Appl. Phys. Lett* **69**, 3938 (1996).

48. Kalisz, J. Review of methods for time interval measurements with picosecond resolution. *Metrologia* **41**, 17 (2003).

49. Zhao, Z. *et al.* Narrow laser-linewidth measurement using short delay self-heterodyne interferometry. *Opt Express* **30**, (2022).

50. Griffiths, P. R. & De Haseth, J. A. Fourier Transform Infrared Spectrometry: Second Edition. *Fourier Transform Infrared Spectrometry: Second Edition* 1–529 (2006) doi:10.1002/047010631X.

51. Born, M. *et al.* Principles of Optics: Electromagnetic Theory of Propagation, Interference and Diffraction of Light. *Principles of Optics* (1999) doi:10.1017/CBO9781139644181.

Chapter 2: Decay Associated Fourier Spectroscopy: Visible to Shortwave Infrared Time-Resolved Photoluminescence Spectra.

We describe and implement an interferometric approach to decay associated photoluminescence spectroscopy, which we term decay associated Fourier spectroscopy (DAFS). In DAFS, the emitted photon stream from a substrate passes through a variable path length Mach-Zehnder interferometer prior to detection and timing. The interferometer encodes spectral information in the intensity measured at each detector enabling simultaneous spectral and temporal resolution. We detail several advantages of DAFS, including wavelength-range insensitivity, drift-noise cancellation, and optical mode retention. DAFS allows us to direct the photon stream into an optical fiber, enabling the implementation of superconducting nanowire single photon detectors for energy-resolved spectroscopy in the shortwave infrared spectral window (λ=1-2 μm). We demonstrate the broad applicability of DAFS, in both the visible and shortwave infrared, using two Förster resonance energy transfer pairs: a pair operating with conventional visible wavelengths and a pair showing concurrent acquisition in the visible and the shortwave infrared regime.

2.1 Canonical TCSPC and Spectra in Tandem

Time correlated single photon counting (TCSPC) provides an invaluable background free method to quantify time-resolved photluminescence (TRPL) from emitters in both ensemble and microscopic contexts. TCSPC has been extensively applied in a range of disciplines such as semiconductor physics,[1,2] nanomaterial science,[3,4] optoelectronic device engineering,5,6 photochemistry,[7] cellular imaging,[8,9] and in the characterization of photoactive materials. TCSPC is typically performed using silicon single photon avalanche detectors (SPADs), which limit its range to photons with energies in the visible and near infrared. However, many technologically relevant species luminesce in the shortwave infrared (SWIR, 1 – 2 μm), i.e. below the bandgap of silicon, ($\boldsymbol{E_g^{Si}}$=1.1 eV). This spectral region includes telecom relevant semiconductor single photon emitters,[10–12] deep tissue imaging dyes,[13–16] and singlet oxygen[17], all of which have broad physical, chemical and biological importance. By combining spectral and temporal resolution of the emitted photon stream we can probe complex photophysics and influence new materials development.

Typically, SWIR detection requires InGaAs photomultipliers tubes or avalanche photodiodes to sense and time photons. In spite of this, these detectors suffer from either low relative efficiencies, high dark count rates, or long reset times.[18] Commercialized SWIR sensitive superconducting nanowire single photon detectors (SNSPDs) have recently overcome these limitations. In an SNSPD, a photon impinges on a superconducting nanowire, creating a transient resistance that can be amplified and timed using traditional TCSPC electronics. SNSPDs detect photons with near unity quantum efficiency[19] and less than 20 ps timing resolution20 in the SWIR, but require that the photon stream be coupled into a single or few mode optical fiber. Consequently, SNSPD's use has been limited to telecommunication studies,[21] quantum key

distribution[22] and characterization of the spectra or anti-bunching properties of SWIR emitters.[12,23,24] Combining spectral resolution with TRPL using SNPSDs will greatly increase the potential applications of this exciting technology.

Spectrally-resolved TRPL (commonly named Decay Associated Spectroscopy or DAS) quantifies the population dynamics of multiple emissive states. Separating luminescent states by photon energy provides direct insight into energy transfer among states,[4] hot carrier dynamics,[2] or enables new channels for multiplexed signal processing.[25,26] In this manuscript, SNSPDs and silicon SPADs are implemented in concert to develop Decay Associated Fourier Spectroscopy (DAFS); which we use to extend DAS across the visible and SWIR. We employ a Mach-Zehnder interferometer (MZI) with TCSPC using multiple detectors to interferometrically sort and time-resolve the emitted photon stream. We outline the theory and implementation of DAFS, demonstrate the method on several Förster resonant energy transfer (FRET) emissive systems, and describe how it provides several advantages over traditional approaches to decay associated emission spectroscopy—focusing on its application in the SWIR.

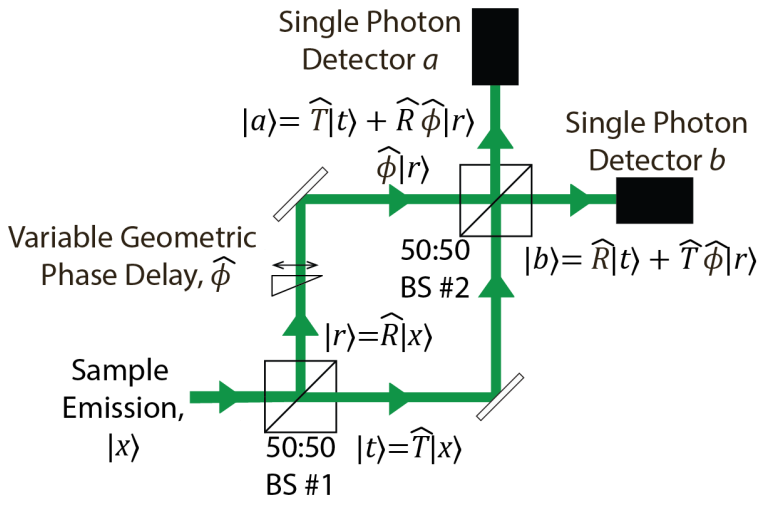

Figure 2.1. Quantum Description of a Conventional Mach-Zehnder Interferometer

Schematic of a conventional Mach-Zehnder interferometer showing the propagation of the photon as a wavefunction from a sample, |x⟩. Shown are the corresponding operations from each component, and the wavefunctions of each arm, and outputs produced by the MZI. The variable geometric phase delay component corresponds to our linear delay stage in our setup. BS: Beamsplitter.

2.2 Semi-Classical Derivation of Mach-Zehnder Interferometry

An idealized Mach Zehnder interferometer is illustrated in Figure 2.1. Photons emitted from the sample are directed through a beamsplitter, and a geometric phase shift is introduced on one path. The beams then recombine at a second beamsplitter, resulting in an interference between transmitted and reflected paths. Unlike a Michelson interferometer commonly employed in FTIR measurements, both path combinations are collected after the second beamsplitter. A typical MZI measurement introduces a sample along one interferometer arm and the resulting phase-shift between reflected and transmitted beams changes the relative intensities in each output path. In our system, we control the phase-shift by scanning a delay stage and thus the interferometer retardation, δ, allowing us to modulate the photon's relative phase in each arm of the interferometer. Following conventions from FTIR spectroscopy, when $\delta = 0$ each path

length is equal, and the beams fully interfere resulting in the "centerburst", the delay stage position of maximum phase coherence.

Following is a semi-classical derivation of the action of a scanning MZI on a photon emitted from a sample. We use the simplifying assumption that each emitted photon possesses a single wavevector, k, and has a normalized wavefunction, $|x\rangle$ (i.e. $\langle x|x\rangle = 1$).[27] When 50:50 beamsplitter reflects $|x\rangle$, inducing a $\frac{\pi}{2}$ phase shift: $\hat{R}|x\rangle = \frac{i}{\sqrt{2}}\ |x\rangle$, or transmits $|x\rangle$, $\hat{T}|x\rangle = \frac{1}{\sqrt{2}}\ |x\rangle$. Within the reflective path, we introduce a variable path geometric phase retardation, $\hat{\phi}$, (experimentally from a delay stage). The phase delay operator is expressed as,

$$\hat{\phi}|x\rangle = e^{i\delta k}|x\rangle \tag{2.1}$$

where $k = \frac{\omega}{c} = \frac{2\pi}{\lambda}$ describes the wavevector of the photon and δ is the scanned interferometer retardation. Therefore, the probability of detecting the self-entangled photon in a detector in the output path $|a\rangle$ is given by,

$$P_a = \langle a|a\rangle = \left[\langle x|\left(\hat{R}\hat{T}\right)^* + \langle x|\left(\hat{T}\hat{\phi}\hat{R}\right)^*\right]\left[\hat{R}\hat{T}|x\rangle + \hat{T}\hat{\phi}\hat{R}\ |x\rangle\right]. \tag{2.2}$$

Which resolves into:

$$P_a = \frac{1}{2}(1 + \cos(\delta k)). \tag{2.3}$$

Similarly, the probability of detecting the photon in a detector in the output path $|b\rangle$ is:

$$P_b = \frac{1}{2}(1 - \cos(\delta k)), \tag{2.4}$$

recovering the equivalent result of the purely classical electric field derivation.[28] Hence the idealized signal, $S_{a,b}^{ideal}(\delta)$, from a stream of identical photons in each detector is:

$$S_{a,b}^{ideal}(\delta) = \dot{N}\, P_{a,b} = \frac{\dot{N}}{2}(1 \pm \cos(\delta k)), \tag{2.5}$$

where $\dot{N}$ rate of sample photon emission. Notice that the spectral component of the signal, $\cos(\delta k)$, from detector a will be anticorrelated to signal from detector b while scanning across δ. For photons with various wavelengths, if we assume photons only interfere within themselves, i.e. first order correlation only, the signal is a weighted sum of cosines:

$$S_{a,b}^{ens}(\delta) = \sum_i \frac{\dot{N}_i}{2}(1 \pm \cos(\delta k_i)), \tag{2.6}$$

and the ideal anti-correlated signal is:

$$S^{AntiCor}(\delta) = S_a^{ens}(\delta) - S_b^{ens}(\delta) = \sum_i \dot{N}_i \cos(\delta k_i), \tag{2.7}$$

where now $\dot{N}_i$ corresponds to the rate of photon emission with of photons with wavevector, k_i. By using time correlated detection, we obtain the photon arrival time relative to laser pulse excitation time, or delay time, τ. So, eq. 2.7 becomes:

$$S^{AntiCor}(\delta, \tau) = \sum_i \dot{N}_i(\tau) \cos(\delta k_i). \tag{2.8}$$

By Fourier transforming $S^{AntiCor}(\delta, \tau)$ along the interferometer retardation domain, δ, we recover the distribution of photons at each corresponding wavevector at each delay time, i.e. our DA spectrum, $I(k, \tau)$.

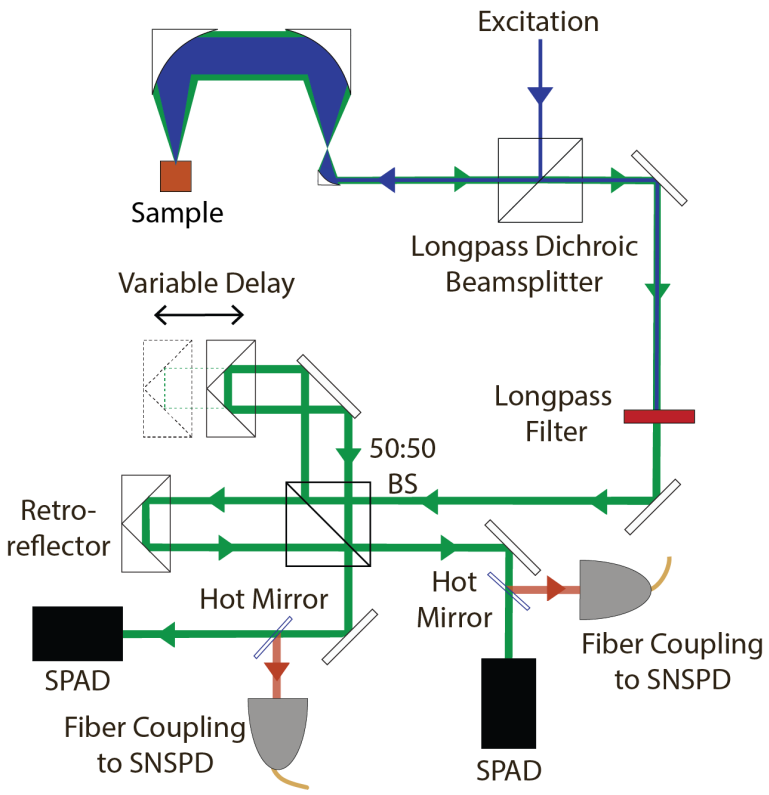

Figure 2.2. DAFS Scheme

The excitation and emission are colocalized in all- reflective off-axis parabolic epifluorescence setup. After passing through the MZI, the photons are separated, using a 700 nm hot mirror and selectively directing them to either the Si SPADs or SNSPDs.

2.3 Implementation of DAFS

We use a custom all-reflective epifluorescence spectrometer to colocalize excitation and collection. The excitation is filtered from the sample photon stream, which passes through the scanning MZI and is selectively directed toward SPADs and/or SNSPDs as illustrated in Figure 2.2. DAFS data is obtained by tagging photon arrival times relative to the laser synchronization pulse (Hydraharp Time-Tagged Time-Resolved or TTTR mode). As stage moves, each position is marker with an TTL pulse that the HydraHarp registers. The signals are globally correlated to the position of the linear translation stage while it scans across the PL's coherence length yielding a time-resolved interferogram. Each photon arrival time is histogrammed into a two-

dimensional matrix with one axis representing stage position, δ', and the other arrival time relative to the pulsed excitation laser.

2.4 Balanced Detection

We establish how an MZI removes shared fluctuations and drift from the spectral measurement. The signal at the single photon detector with noise is

$$S_{a,b}(\delta') = \frac{\eta_{a,b}}{2}\left(S_{a,b}^{ens}(\delta') + S^{CorNoise}\left(\delta'(T)\right)\right) + S_{a,b}^{StatNoise}. \tag{2.9}$$

In eq. 9, $\eta_{a,b}$ incorporates respective detector quantum efficiency and losses from the setup and $S_{a,b}^{StatNoise}$ is the static noise from dark counts and constant background scattered light unique to each detector. The $S^{CorNoise}\left(\delta'(T)\right)$ refers to the fluctuation/drift noise, in global time, T, common to both detectors, e.g. a moving baseline observed in figure 3a.

Considering the signal when δ' isoutside the coherence length of the photon stream so $S^{AntiCor}(\delta') = 0$, then in range we express the ratio of detector signals as:

$$\frac{S_a(\delta')}{S_b(\delta')} = \left(\frac{\eta_a}{\eta_b}\right)\left(\frac{\left(1 + S^{CorNoise}\left(\delta'(T)\right)\right) + S_a^{StatNoise}}{\left(1 + S^{CorNoise}\left(\delta'(T)\right)\right) + S_b^{StatNoise}}\right) \tag{2.10}$$

Hence by fitting a linear regression to $S_a(\delta')$ vs $S_b(\delta')$ we may extract the slope, $\left(\frac{\eta_a}{\eta_b}\right)$, as plotted in figure 2.3b. Taking the difference of the two detectors' signals weighted by their respective efficiency terms (i.e. the slope extracted from eq. 2.10), $\left(\frac{\eta_a}{\eta_b}\right)$, we obtain a post-processed balanced signal. This eliminates the drift/fluctuation term, $S^{CorNoise}\left(\delta'(T)\right)$:

$$S_a(\delta') - \left(\frac{\eta_a}{\eta_b}\right)S_b(\delta') = S^{AntiCor}(\delta') + S_a^{StatNoise} - \left(\frac{\eta_a}{\eta_b}\right)S_a^{StatNoise}. \tag{2.11}$$

We can further eliminate the static noise terms by subtracting the mean of eq. 11:

$$S(\delta') = S_a(\delta') - \left(\frac{\eta_a}{\eta_b}\right) S_b(\delta') - \text{ Mean}\left[S_a(\delta') - \left(\frac{\eta_a}{\eta_b}\right) S_b(\delta')\right]_\delta = \sum_i \dot{N}_i \cos(\delta k_i). \tag{2.12}$$

Hence, we recover eq. 2.7's idealized anti-correlated signal as seen in figure 2.3c. Uncorrelated drift/fluctuations and shot noise are still present in the signal. However, upon Fourier transforming eq. 2.12, the uncorrelated drift/fluctuations contributions fall outside of the spectral region of interest, limiting their impact on our signal.

2.5 Chirp Correction

The derivation of eq. 2.5 assumes that the phase difference between the two MZI arms has no wavelength dependence given by $\hat{\phi}$. This yields a symmetric Fourier spectrum around the centerburst. However, a dispersive component in the phase delay, $\theta(k)$, can contribute an asymmetry or "chirp" (figure 2.3a and 2.3b), resulting in a change of the detection probability for a given k:[28]

$$S^{AntiCor}(\delta') = \sum_i \dot{N}_i \cos\big(\delta k_i - \theta(k_i)\big). \tag{2.13}$$

Upon Fourier transforming $S(\delta)$ yields a complex PL spectrum, $I(k)$:

$$I(k) = \int_{-\infty}^{\infty} S(\delta') e^{-ik\delta'} d\delta' = \text{Re}[I(k)] + i\ \text{Im}[I(k)] = |I(k)| e^{i\theta(k)}. \tag{2.14}$$

To correct for this dispersive component, we employ the Mertz method from the FTIR literature as described in the SI.[28] Briefly, we extract the slow moving phase, $\theta(k)$, from a subset of the data around the centerburst and use it to correct the overall DAS through the complex Euler identity.

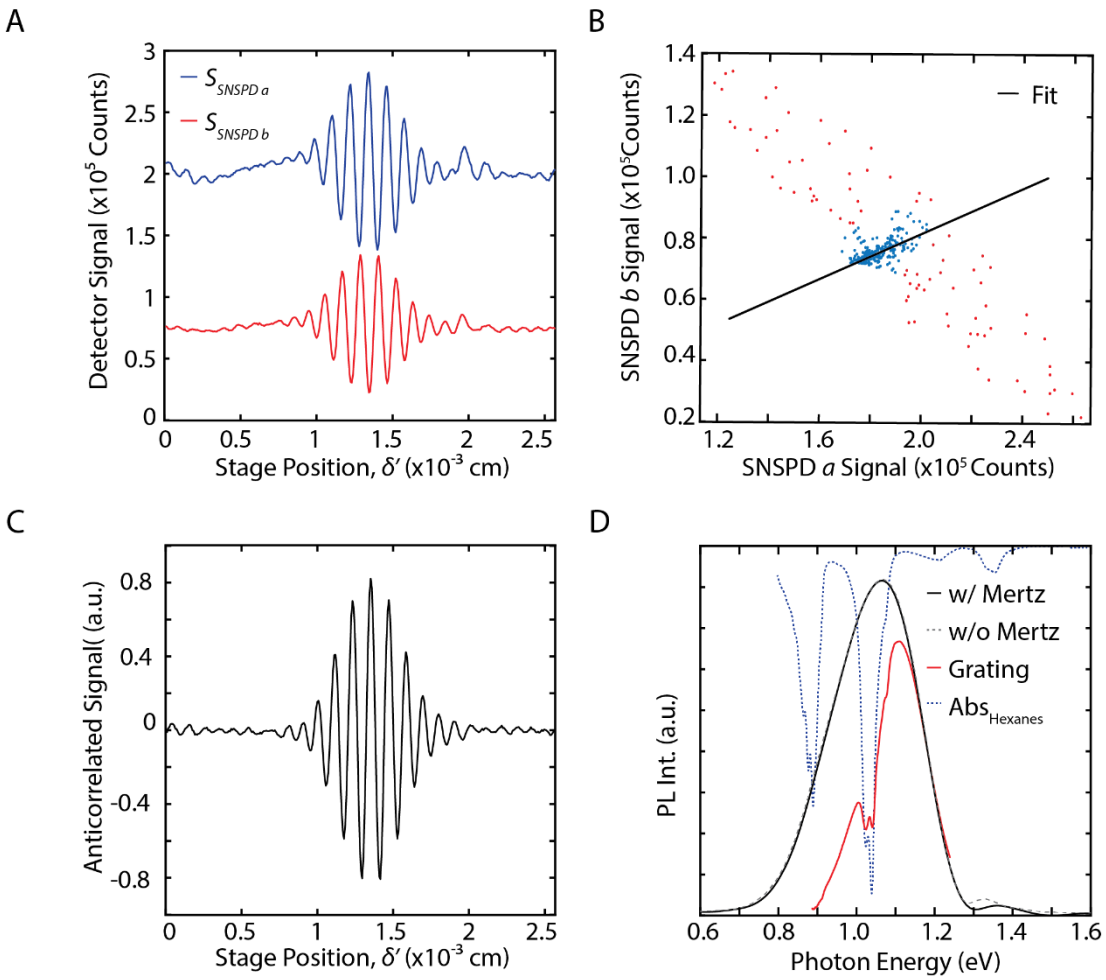

Figure 2.3. Mertz Correction

A. The integrated raw interferometric trace from each SNSPD detector collected from a sample of colloidal PbS NC in hexanes (532 nm excitation). B. The correlated signal (blue dots) from SNSPD a vs SNSPD b was fit with a line and its slope corresponding to $\left(\frac{\eta_a}{\eta_b}\right)$was extracted (eq. 2.10). The red dots are anti-correlated and fall outside of our fit. C. The corrected anti-correlated signal as determined by eq. 1.12. D The PL spectrum of the colloidal PbS NC in hexanes under a 532 nm excitation obtained from the apodized and zero-padded Fourier transform of the anti-correlated signal in with Mertz correction (black solid) and without (grey dashed). The signal shows negligible chirp which accounts for the minimal difference. The red line shows the emission as obtained from a side-illuminated grating spectrometer with an InGaAs detector. The discrepancy in the peak shape/width is attributed to the hexanes absorption (blue dashed).

Figure 2.3D demonstrates the comparison between the Mertz phase corrected spectrum and the uncorrected spectrum.

2.6 Application of DAFS

Energy transfer between two chromophores present an ideal system to test this DAS method. FRET processes control the energy flow within many chemical or condensed phase systems,[4] and FRET pairs are employed as implanted sensors and nanoscale rulers for studying dynamic distance fluctuations.[29,30] First, we study a mixture of CdSe colloidal nanocrystals (NC) and Pinacyanol chloride (PIC-Cl) dye. Our second sample shows the spectral breadth of the DAFS by probing emissions ranging from the visible to the SWIR with donor CdSe colloidal NCs and acceptor PbS colloidal NCs.

2.7 Observing FRET in DAFS

To show the effectivity of the MZI DAFS in the conventional visible DAS regime, we prepared the mixed FRET solution of CdSe NC (donor) and PIC-Cl (acceptor) in dichloromethane. The linear PL spectra (figure 2.4a) from a conventional grating spectrometer showed a depleted emission of the CdSe NC in the mixed solution at $2.15\ eV$ relative to the isolated CdSe NC solution; this indicates an energy loss of the CdSe NC emissive state. Accordingly, we observe an enhanced emission in the FRET solution from the PIC-Cl at $1.95\ eV$ in comparison to the isolated PIC-Cl solution in the mix, showing an energy transfer to the PIC-Cl. After a DAFS acquisition and analysis on the CdSe NC and PIC-Cl we obtained the time-resolved anti-correlated signal displayed in Figure 2.4B. Applying the Mertz corrected Fourier transform to each time slice we observe two spectral features in Figure 2.4C. The peak at $2.15\ eV$ reflects the dynamics of the donor, CdSe NC, and the peak at $1.95\ eV$ reflects the dynamics of the acceptor, PIC-Cl. By

integrating across the spectral region for the CdSe NC ($2 - 2.25\ eV$) and PIC-Cl ($1.9 - 2.0\ eV$) we can resolve their respective TRPL lifetime traces. The bottom panel of figure 4c shows similar lifetimes for both the CdSe NC and the PIC-Cl, which is consistent with a FRET process from a long lived CdSe donor to a short lived PIC-Cl acceptor.[31] In comparison to the TCSPC traces taken from the isolated solutions of CdSe NC (figure 4d) and PIC-Cl (figure 4e), we observe diminished the PL lifetimes in the CdSe NCs and increased PIC-Cl lifetimes (details of the fitting time

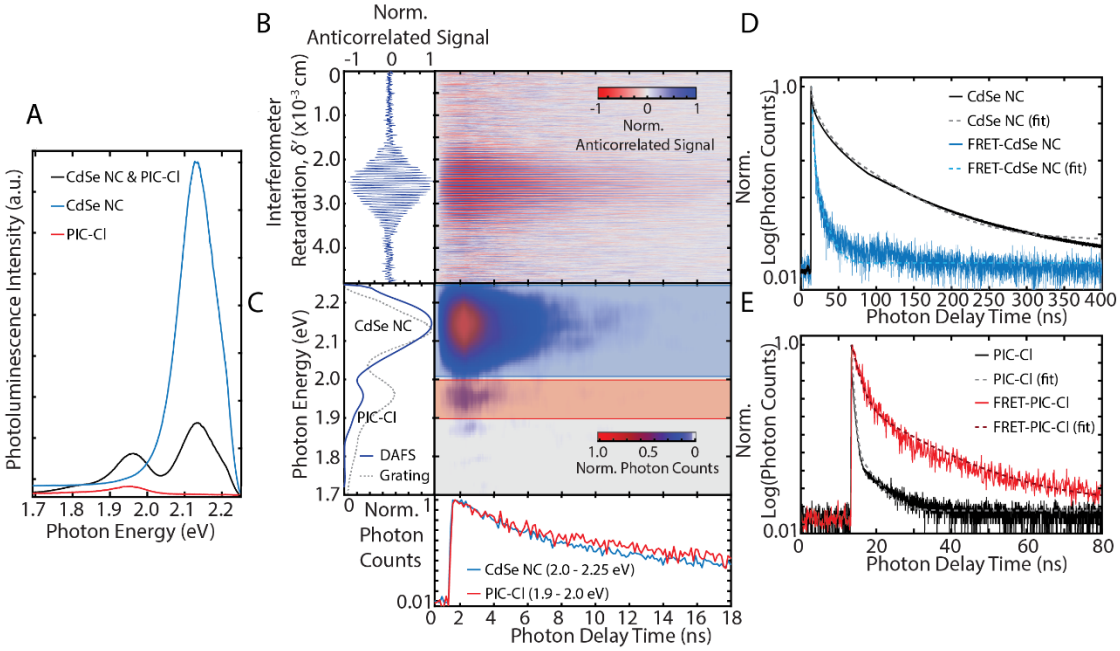

Figure 2.4. Analyzing FRET with DAFS

A. PL spectrum of CdSe NC (donor) and PIC-Cl (acceptor) as isolated and mixed solutions. In the presence of PIC-Cl the NC emission is strongly quenched while the PIC-Cl emission is enhanced. B. A plot of the time-resolved interferogram of the CdSe NC and PIC-Cl mixed solution after application of eq. 12 to balance the detectors. The left-hand panel shows the result of summing along the time delay axis to give the time-averaged interferogram. C. DA spectrum obtained by Fourier transforming and applying the Mertz correction each delay. Spectral features corresponding to the CdSe NCs at ~2.15 eV (light blue) and to the PIC-Cl at ~1.95 eV (red). The left-hand panel gives the time-averaged PL spectrum from the Fourier transform, compared to the grating base measurement. The bottom panel shows the TRPL traces corresponding CdSe NC and PIC-Cl. D. TRPL traces corresponding to an isolated CdSe NCs (black) and CdSe NCs PIC-CL (blue). E. TRPL traces corresponding to an isolated PIC-Cl solution (black) PIC-Cl in the FRET pair mixed solution obtained from the DA spectrum summing from 1.9-2.0 eV.

constants can be found in the SI in table 2.1.) This is consistent with a FRET process, in which the CdSe NC more rapidly transfer their excited state energy to the PIC-Cl resulting in longer overall lifetimes.[11,31]

2.8 Octave Spanning

To demonstrate the octave-spanning capabilities of DAFS, we show another donor-acceptor system which requires resolving emission from 0.8 to 2.2 eV (560-1600 nm). Again, the CdSe NCs act as donors and are excited at 2.33 eV. The acceptors are PbS colloidal NCs which emit between 0.8 and 1.1 eV. We concurrently acquire anti-correlated visible and SWIR photon streams using SPADs and SNSPDs from each output.

After processing, the 2D photon energy/lifetime histogram is shown in figure 2.5. The spectrum shows features corresponding to both the CdSe NCs at 2.1 eV and PbS NCs at 1.1 eV. By integrating across the spectral region for the CdSe NC (2-2.25 eV) and PIC-Cl (1.9-2.0 eV) we can resolve their respective TRPL unique lifetime traces in the bottom panel of figure 2.5. In comparison to the TCSPC traces taken from the isolated solutions of CdSe NC (figure 2.4d) and PbS NC (figure 2.9), we observe somewhat unchanged PL lifetimes for the CdSe NC and a reduction in the PbS lifetimes increased (multi-exponential fitting details found in the SI.) This is consistent with a FRET process, in which the CdSe NC more transfer their excited state energy to the PbS, resulting high transient excited state population which causes faster emission.[31]

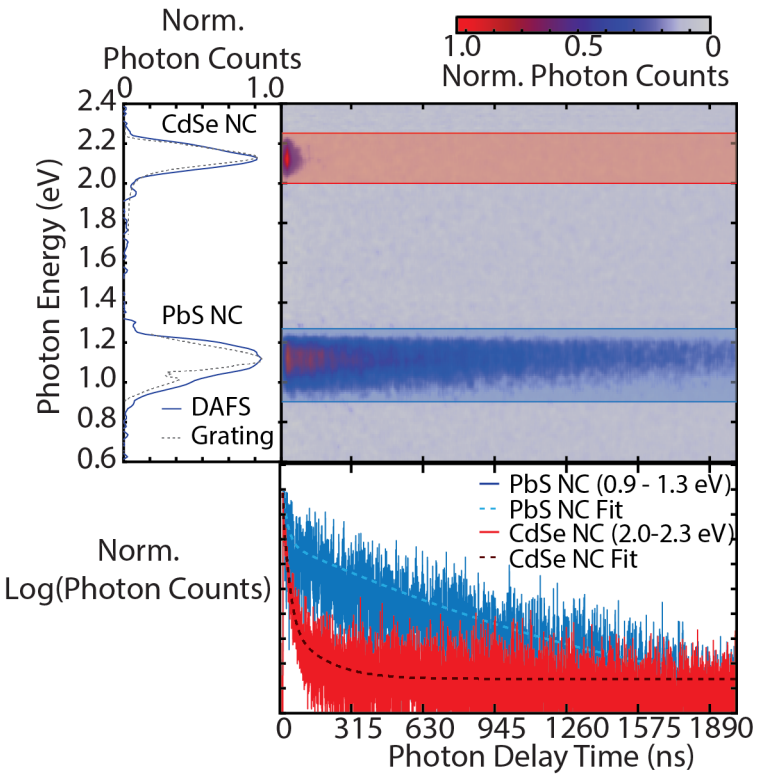

Figure 2.5. Octave Spanning in DAFS

Corrected DAFS spectrum of the CdSe NC and PbS NC FRET solution. The left panel shows the time averaged spectrum. The bottom panel shows the time traces corresponding to the spectral components PbS NCs and CdSe NCs respectively taken by summing the spectral slices in the appropriately labeled ranges.

2.9 Discussion

We compare DAFS to conventional photon-resolved DA spectra, obtained by scanning a grating monochromator with a single pixel SPAD. In this implementation, the grating lines/mm, slit width, and path length of the spectrometer lead to a tradeoff between resolution and throughput.[28] In most implementations the monochromator disrupts the optical mode, limiting its applicability for use with small area detectors, such as SNSPDs. Furthermore, in a grating based measurement, fluctuations in the count rate cannot be separated from changes in the spectral content of the signal. This makes it challenging to acquire spectra from emitters with fluctuating brightness. DAFS

overcomes the tradeoff between resolution and throughput by collecting DA spectra interferometrically, thus avoiding use of a slit or grating (i.e. Jaquinot's advantage). Our theoretical spectral resolution is 12.4 μeV, depending only on the path length that our stage can sample.[28] Our approach retains the optical mode and polarization of the emitted photon stream allowing us to couple the light into cryogenically cooled SNSPDs and extend our method into the SWIR. By encoding spectral information in the anti-correlated photon signal from two single photon detectors positioned at each output of the interferometer DAFS acquisitions are insensitive to signal drift/fluctuation through spectrally balanced detection, as shown in figure 3c.

Interferometric detection methods are commonly used for mid-infrared absorption measurements,[28] e.g. FTIR, and have yet to be extensively implemented in the visible. Recently, Perri *et al.* demonstrated similar single-path interferometric TRPL, measurements.[32] Here, they adapt their Translating-Wedge-based Identical pulses eNcoding System (TWINS) to provide a phase delay between "transmitted" and "reflected" paths. Our approach complements the TWINS interferometric method adding all-reflective epifluorescence collection, a Mach Zehnder interferometer, and the use of SNSPDs. We thus obtain balanced spectral detection, increased photoluminescence collection and a broad spectral range--well suited for samples with unknown or weak emission that requires long acquisition times.

2.10 Conclusions

We implement and use decay associated Fourier spectroscopy to attain energy resolved—and thus state specific-- photoluminescence decay spectra across the visible and shortwave infrared. After processing the photon stream acquired along both output ports of a Mach Zehnder interferometer, we acquire two-dimensional photon energy-lifetime histograms. Our implementation enables us

to probe weak signals of visible and SWIR photons simultaneously, allowing us to interrogate the electronic states in organic and inorganic materials. In general, combining path length interferometry with single photon detection can provide new contrast in exploring how complex energy transfer manifests multi-chromophore systems. In the limit of detector noise dominating the signal from a given state, interferometric measurements are intrinsically multiplexed, and thus the signal improves with the higher count rates (i.e. Felgett's Advantage). DAFS will therefore excel for samples with very low photon count rates for a given state, especially in the background of a large signal. For example, material experiments on systems with low quantum yields (e.g. triplet phosphorescence), and low excitation fluxes used (e.g. exciton annihilation experiments) or low number density of emitters (for example in a microscope) would all be enhanced using DAFS. Utilizing SNSPDs as SWIR photon detectors, instead of InGaAs technology also leverages faster reset times, lower dark count rates, and improved timing resolution for sensitive detection of weak signals in the SWIR. Finally, in using an all-reflective excitation/collection scheme allows for highly multiplexed detection from the visible ($\sim 390\,n\mathrm{m}$) to the SWIR ($\sim 2\,\mu\mathrm{m}$). As demonstrated in figure 5, we access octave spanning dynamics using SPADs and SNSPDs concurrently, without the need for filters to block out second order diffraction from a grating. This is ideal for studying new systems with unknown emission energies. In the future, we will apply DAFS techniques to second order correlation measurements, single molecule spectral dynamics, photon correlation Fourier spectroscopy, and the detection of entangled photons through antibunching.

2.11 Supplementary Information

Experimental Setup

The sample is excited by a 532 nm pulsed diode laser (LDH-P-FA-530B, PicoQuant). The excitation is focused onto the sample using off-axis parabolic mirrors hard mounted onto an aluminum block. The epifluorescence is then collected and collimated by the same off-axis parabolic mirrors and transmitted through the 550 nm longpass dichroic beamsplitter (DMLP550R, Thorlabs). Any remaining excitation light is filtered by a notch (NF533-17, Thorlabs) and longpass filter (FEL0550, Thorlabs). The sample PL emission was then transmitted through the MZI: the PL was passed through a 50:50 cube beamsplitter (20BC17MB.1, Newport) with one path containing a fixed hollow retroreflector and the other directed to linear translational stage (ANT-95L-050, Aerotech). The output of each path is recombined at different spot on the same 50:50 cube beamsplitter. The two outputs of the interferometer were then split using hot mirrors with ultraviolet and visible light were transmitted through and focused onto APDs (PD-050-CTD, Micro Photon Devices), while near and shortwave infrared light are reflected into a single-mode fiber (F-SMF-28-C-3FC, Newport) coupled reflective collimator and detected using SNSPDs (Quantum Opus One). Photon streams are timed by a HydraHarp 400 (Picoquant) in Time-Tagged Time-Resolved (TTTR) mode while moving the interferometer's linear translational stage at constant velocity.

Data acquisition

We implement a 2D histogramming algorithm, where each photon arrival is placed into a bin corresponding to its arrival time relative to laser pulse or delay time, τ_i and a bin corresponding to the stage delay, δ', calculated from the count of the laser's synchronization pulse given the laser

repetition rate, R, and markers sent from an external pulse generator at each position change. This marker helps to define the binning of step size in the interferometer.

Balanced Detection

Histogramming produces a time-resolved interferogram for each channel signal, $S_{a,b}(\delta'_N, \tau_i)$. By summing along the delay time axis, t, $\sum_j S_{a,b}(\delta'_N, \tau_i)$, we recover a delay-time averaged interferogram, $\langle S_{a,b}(\delta'_N)\rangle_{\tau_i}$ for each channel. From $S_{a/b}(\delta'_N)$, we define the points outside the coherence length and thus will be dominated by signal that is correlated between the two detectors as within the one standard deviation of the mean of $S_{a,b}(\delta'_i)$ for each detector:

$$S_{a/b}^{correlated}(\delta'_N) \in \tag{2.15}$$

$$\text{Mean}[S_{a,b}(\delta'_N)]_\delta - \sqrt{\text{Var}[S_{a,b}(\delta'_N)]} \leq S_{a,b}(\delta'_N) \leq \text{Mean}[S_{a,b}(\delta'_N)]_\delta + \sqrt{\text{Var}[S_{a,b}(\delta'_N)]} \tag{2.16}$$

The slope of the linear fit between $S_a^{correlated}(\delta'_N)$ vs $S_b^{correlated}(\delta'_N)$ gives the $\left(\frac{\eta_a}{\eta_b}\right)$ scaling factor. When subtracting the scaled detector signals, we recover only the anti-correlated signal (containing all the spectral information) with an offset.

Using this, we take this scaling factor and apply it to the 2D time-resolved signals, subtracting the two channel signals as described in the main text eq. 2.9, resulting in one overall 2D time resolved histogram for both channels. To eliminate a linear offset in the interferogram at each time slice, t_i, we subtract the mean at each t_i (averaged over each δ'_N). This results in a 2D time-resolved interferogram, $S_{bal.}(\delta'_N, \tau_i)$, that oscillates about 0 as shown in the manuscript figure 2.4b.

Mertz Phase Corrected Fourier Transform

In the ideal case all photon frequencies follow the same path in the interferometer, possessing the same centerburst ($\delta = 0$) position, yielding a symmetric two-sided interferogram. However, frequency dependent refractive indices, result in a chirped or asymmetric interferogram. The frequency dependent phase shift, $\theta(k)$ is a common occurrence in interferometric methods, such as FTIR and typically corrected using the Mertz method.[21] The method effective determines the slow moving phase of the interferogram and corrects the Fourier transform accordingly.

We implement the Mertz correction for our data by taking a 64 point subset, $S_{subset}({\delta'}_N)$, around the approximate centerburst region of our balanced delay-time averaged interferogram, $\langle S_{bal.}({\delta'}_N)\rangle_{\tau_i}$. The subset is chosen by determine the point of maximum signal and taking 32 data points before and 31 after. The $S_{subset}({\delta'}_N)$ was apodized with a triangle function and Fourier transformed giving the corresponding spectrum, $I'(k)$, with slowly varying phase, $\theta'(k) = \arctan\frac{\mathrm{Im}[I'(k)]}{\mathrm{Re}[I'(k)]}$. As this was taken from a subset of $\langle S_{bal.}({\delta'}_N)\rangle_{\tau_i}$, the number of points of $\theta'(k)$ are less than those from the Fourier transform of the complete interferogram (i.e. smaller dimension). To match the dimensional length a linear interpolation of $\theta'(k)$ is performed.

To determine the complete Mertz phase-corrected time-resolved decay associated spectrum, we take the complete time-resolved interferogram, $S_{bal.}({\delta'}_N, \tau_i)$, and Fourier transform along ${\delta'}_N$ at giving a spectrum, $I(k)$, each time t_i. The Mertz phase-corrected spectrum, $I_{cor}(k)$, at each delay-time t_i is:

$$I_{cor}(k) = \mathrm{Re}[I(k)]\cos\big(\theta'(k)\big) + \mathrm{Im}[I(k)]\sin\big(\theta'(k)\big) \tag{2.14}$$

Stitching these delay-time slices back together we recover the Mertz phase-corrected decay associated spectrum, $I_{cor}(k, \tau_i)$ as plotted in figures 2.4c and 2.5 in the manuscript.

Materials and Solution Preparation

The absorbance spectra were taken using UV-Vis Cary60 for visible only or JASCO V-770 UV/Vis/NIR for visible and SWIR. The photoluminescence spectra were acquired using a pulsed 532 nm excitation laser (LDH-P-FA-530B, PicoQuant) with a home-built all-reflective epifluorescence collection with a 550 longpass and detected with Flame spectrophotometer (Ocean Optics). The same setup was used for visible and SWIR TCSPC measurement, but the light was passed to silicon APDs or SNSPDs. SWIR photoluminescence spectra were taken using Horiba Fluorometer PTI QM-400 with a liquid nitrogen cooled InGaAs and under 532 nm excitation.

Oleic Acid Capped CdSe Colloidal Nanocrystals

Colloidal CdSe nanocrystal synthesis was adapted from previous methods.[33] A selenium precursor solution was prepared by dissolving 30 mg of selenium (Acros, 99.5% powder) in 5 mL of octadecene (ODE, Alfa Aesar, tech. 90%) and 0.4 mL of trioctylphosphine (Acros Organic, 90%). The cadmium precursor solution was made by dissolving 25 mg CdO (Alfa Aesar, 99.5% metal basis) in 1.2 mL oleic acid (Alfa Aesar, 99%) and 20 mL of ODE. Both precursor solutions were degassed with argon. While under inert argon atmosphere, the CdO solution was heated to 225°C. The selenium solution was then injected into the CdO solution. The reaction proceeded at 225°C for 3 minutes and was quenched using an ice bath. The CdSe was crashed out of solution by using

methanol and acetone and centrifuging the mixture at 14000 rpm (Sorvall Legend X1 Centrifuge) for 30 min. The organic layer was extracted, and dichloromethane (DCM) was used as a solvent.

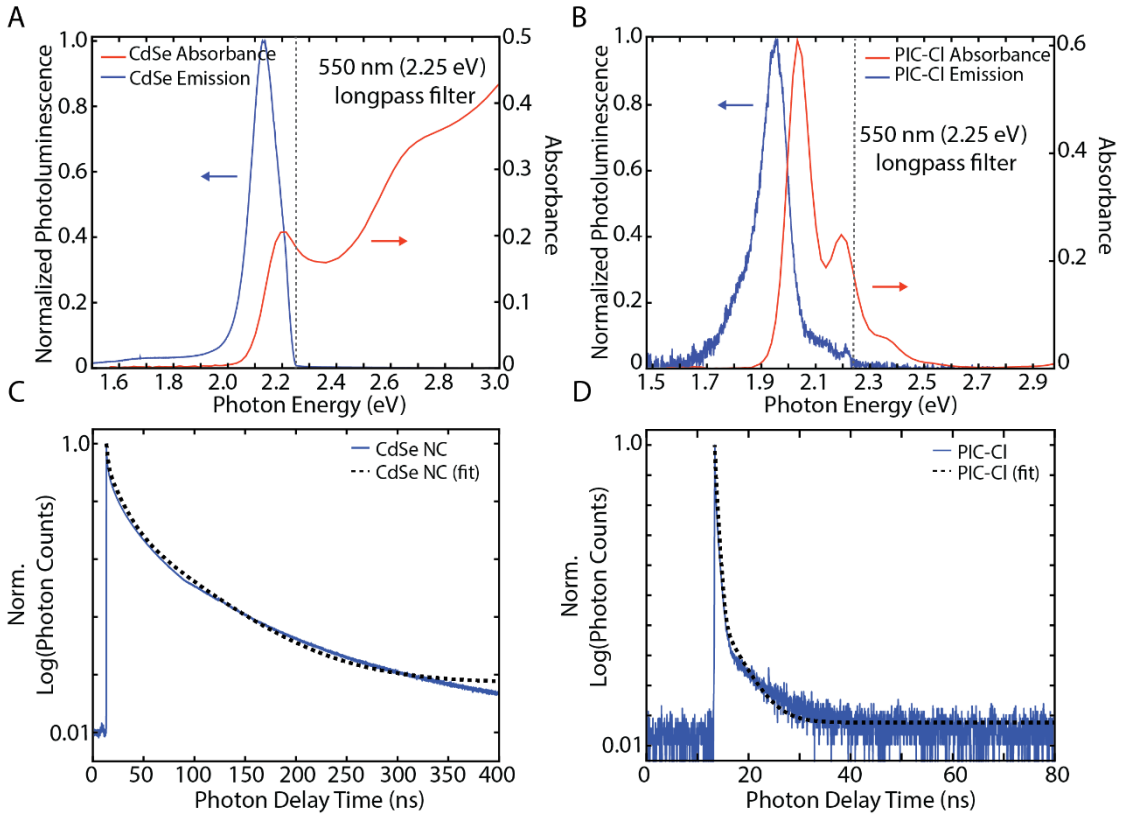

Figure 2.6. Optical Characterization of CdSe and PIC-Cl

A. Photoluminescence (blue) and absorbance (orange) spectra of CdSe nanocrystals. A 550 nm longpass filter (dashed grey) was used to remove excess excitation light.B. Photoluminescence (blue) and absorbance (orange) spectra of the Cy-3 dye pinacyanol chloride (PIC-Cl). A 550 nm longpass filter (dashed grey) was used to remove excess excitation light C. TCSPC trace taken of the CdSe NC (blue) with triexponential fit (grey dotted). See table S1 for fit details. D. TCSPC trace taken of the PIC-Cl (blue) with triexponential fit (black dotted). See table 2.1 for fit details.

Oleic Acid Capped PbS Colloidal Nanocrystals

Colloidal PbS nanocrystal synthesis was adapted from previous methods.[34] Briefly, a sulfur precursor solution was prepared by suspending 215 mg of diphenylthiourea (Alfa Aesar, 98%) in 3 mL of ODE and degassing under vacuum for 1 hour at 100°C. The suspension was heated to 125°C under argon and held at temperature for 30 min. The suspension was then cooled to 30°C.

The lead precursor solution was prepared by suspending 836 mg $PbCl_2$ (Alfa Aesar, reagent grade) in 7.5 mL oleylamine (TCI Chemicals) and degassing under vacuum at 100°C for 1 hour. The solution was heated to 125°C under argon and held for 30 min. The solution was set for 120°C and 2.25 mL of the diphenyl thiourea solution was injected. The reaction was quenched after 600 sec by adding a mixture of 10mL of toluene and 25 mL of ethanol and centrifuge at 14000 rpm (Sorvall Legend X1 Centrifuge) for 10 min. After decanting, the solution was cleaned two more times in a toluene/ethanol mixture, then diluted in hexanes.

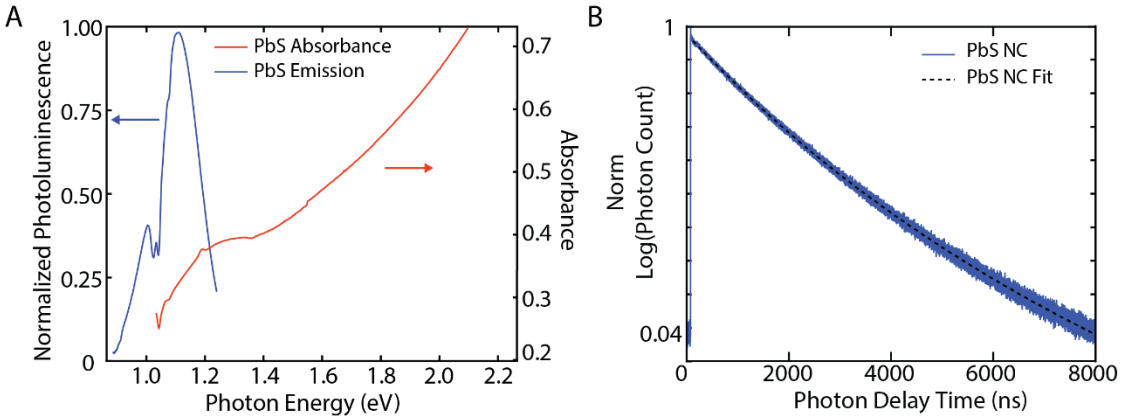

Figure 2.7 Optical Characterization of PbS

A. Photoluminescence (blue) and absorbance (orange) spectra of PbS nanocrsytals. B. TCSPC trace taken of the PbS NC (blue) with biexponential fit (black dotted). See table 2.1 for fit details.

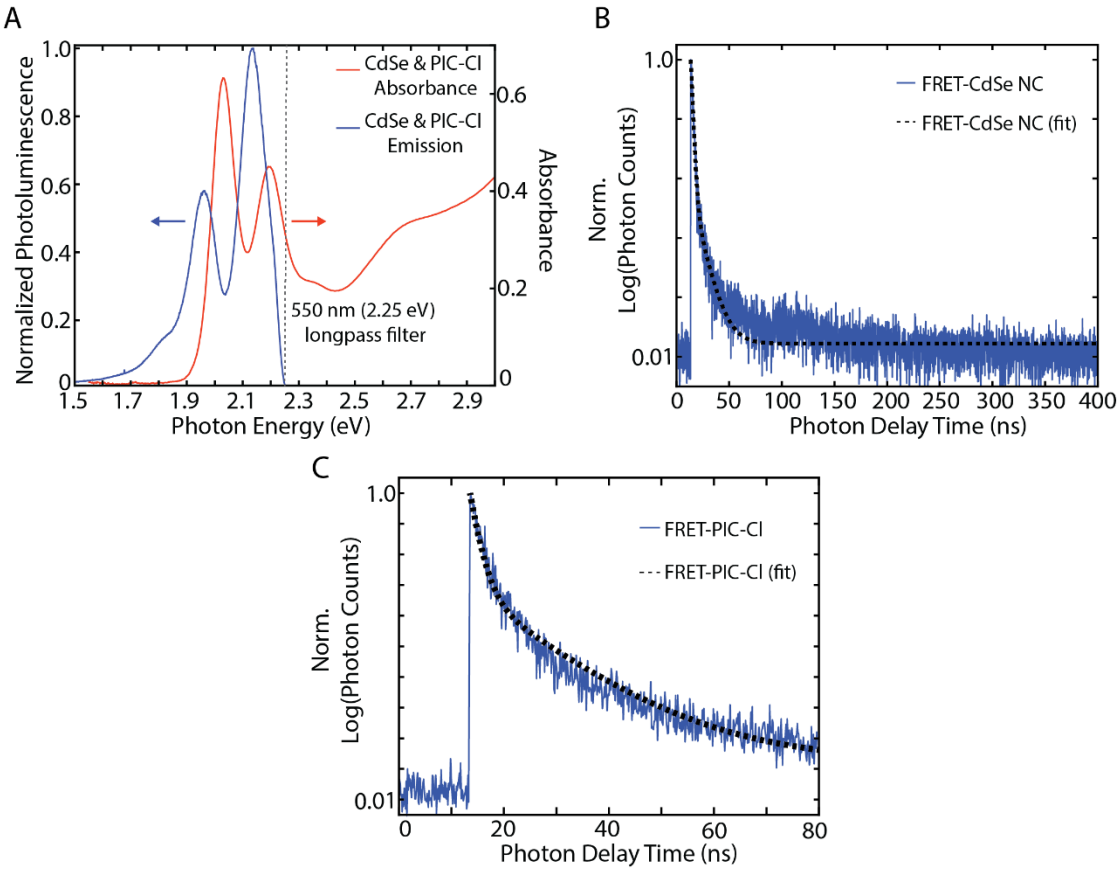

Figure 2.8 Optical Characterization of PIC-Cl/CdSe FRET

A. Photoluminescence (blue) and absorbance (red) spectra of the mixed sample of Cy-3 dye pinacyanol chloride (PIC-Cl) and CdSe NC. A 550 nm longpass filter (dashed grey) was used to remove excess excitation light. B. TRPL trace taken of the CdSe NC component of the PIC-Cl & CdSe FRET pair. This was fit using biexponential function. C. TRPL trace taken of the PIC-Cl nanocrystals component of the PIC-Cl & CdSe FRET pair. This was fit using biexponential function. See table 2.1 for fit details.

Details of Fitting

All TRPL traces were fit to either a bi- or trixponential of the form using Matlab software

$$(t) = A_1 e^{-\frac{t}{\tau_1}} + A_2 e^{-\frac{t}{\tau_2}} + A_3 e^{-\frac{t}{\tau_3}} + C \tag{2.15}$$

The following table gives all fitting coefficients extracted with the corresponding fit error

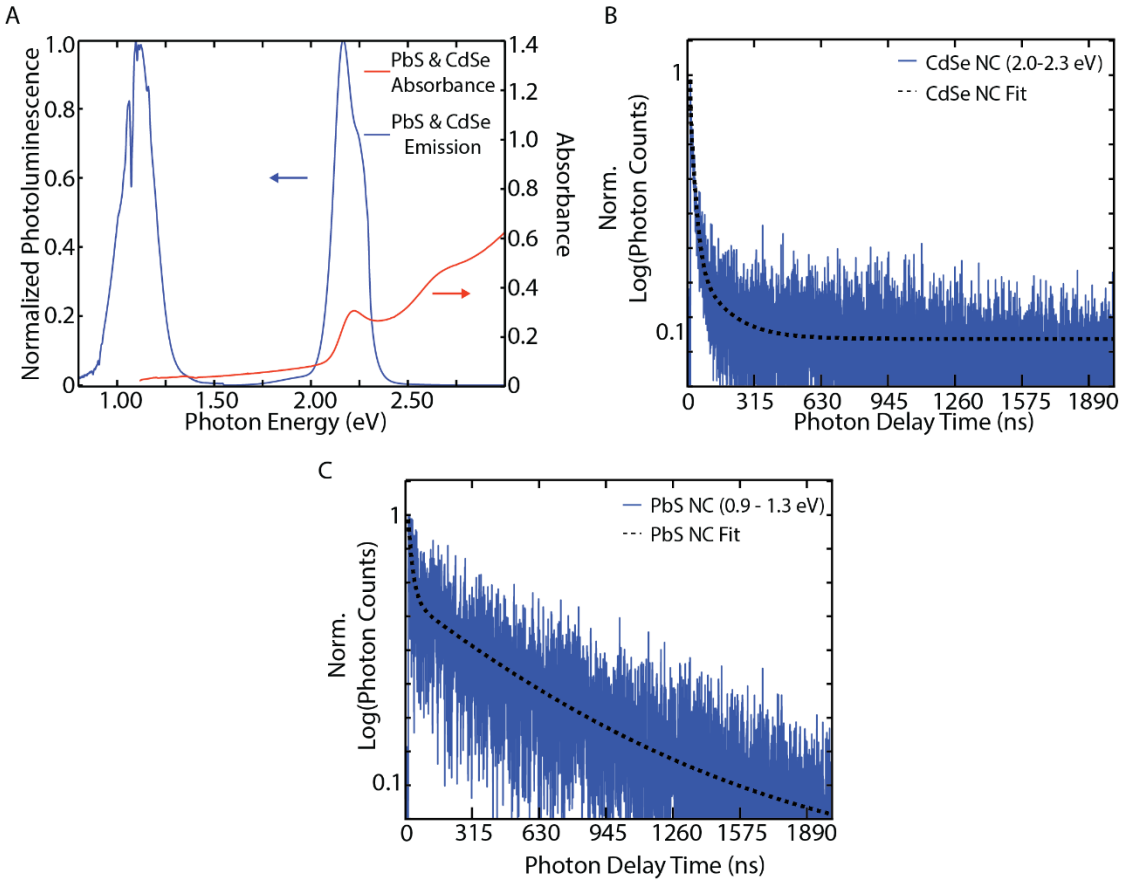

Figure 2.9 Optical Characterization of PbS/CdSe FRET

a Photoluminescence (blue) and absorbance (red) spectra of the mixed sample of PbS NC and CdSe NC. b TRPL trace taken of the PbS nanocrystals component of the PbS & CdSe FRET pair. This was fit using biexponential function. c TRPL trace taken of the CdSe NC component of the PbS & CdSe FRET pair. This was fit using triexponential function. FRET pair. This was fit using triexponential function.

Table 2.1 Bi- or Triexponential Fitting coefficients for the TRPL traces of CdSe NC, PIC-Cl and PbS isolated or in FRET solutions.

	CdSe NC	CdSe NC (w/ PIC-Cl)	CdSe NC (w/ PbS NC)	PIC-Cl	PIC-Cl (w/ CdSe NC)	PbS NC	PbS NC (w/ CdSe NC)
A_1	$(6.26 \pm 0.02) \times 10^4$	196 ± 1	3.7 ± 0.4	$(2.90 \pm 0.02) \times 10^4$	13.7 ± 0.2	$(4.3 \pm 0.1) \times 10^3$	5.4 ± 0.8
$\tau_1\ (ns)$	1.399 ± 0.005	1.87 ± 0.06	1.5 ± 0.3	0.1434 ± 0.0006	1.87 ± 0.06	1260 ± 10	21 ± 5
A_2	$(1.299 \pm 0.002) \times 10^5$	12 ± 1	7.8 ± 0.2	$(4.04 \pm 0.02) \times 10^4$	3.6 ± 0.2	$(3.9 \pm 0.1) \times 10^3$	13.5 ± 0.2
$\tau_2\ (ns)$	12.67 ± 0.03	9.9 ± 0.7	20 ± 1	0.350 ± 0.001	16.5 ± 0.7	2940 ± 50	910 ± 60
A_3	$(5.49 \pm 0.02) \times 10^4$	-	1.3 ± 0.2	$(2.8 \pm 0.1) \times 10^2$	-	-	-
$\tau_3\ (ns)$	55.5 ± 0.2	-	130 ± 10	2.90 ± 0.09	-	-	-
C	5.2 ± 0.3	0.46 ± 0.03	1.30 ± 0.01	5.2 ± 0.3	0.318 ± 0.008	90 ± 7	4.8 ± 0.3

CdSe NC and PIC-Cl FRET Discussion Concerning Time Constants

All TRPL traces were fit to either a bi- or trixponential of the form using Matlab software Comparing the isolated the CdSe NC TRPL lifetimes to the CdSe NC lifetimes in the FRET solution with PIC-Cl solution: we observe a shortening of the lifetimes suggesting more rapidly transfer their excited state energy to the PIC-Cl resulting in shorter overall lifetimes. Further support for FRET is seen when comparing the isolated PIC-Cl lifetimes to the PIC-Cl in the FRET solution. The PIC-Cl lifetimes lengthen considerably in the FRET solution, to the point where they show similar dynamics to the CdSe NC, which is consistent in the FRET process with a long lived donor and short lifetimes acceptor.[35]

CdSe NC and PbS NC FRET Discussion Concerning Time Constants

Comparing the isolated the CdSe NC TRPL lifetimes to the CdSe NC lifetimes in the FRET solution with PbS NCs: we observe similar lifetimes, with the longer time components lengthening a small amount. This is likely due to the faster strongly emissive states transferring their energy to the PbS NCs and the longer lived states then emitting. FRET behavior is also observed comparing the isolated PbS NC lifetimes to the PbS NC lifetimes in the FRET solution. The PbS NC lifetimes shorten dramatically in the FRET solution as a result of the transient high excited state population due to the CdSe NC transferring their excited state energy. At long times the PbS returns to its own long TRPL lifetime, though it a mixed sample may introduce new non-radiative loss channels which shorten the microsecond lifetime.[31]

References

(1) Lien, D.-H.; Uddin, S. Z.; Yeh, M.; Amani, M.; Kim, H.; Ager, J. W.; Yablonovitch, E.; Javey, A. Electrical Suppression of All Nonradiative Recombination Pathways in Monolayer Semiconductors. *Science (80-.).* **2019**, *364* (6439), 468–471. https://doi.org/10.1126/science.aaw8053.

(2) Zhu, H.; Miyata, K.; Fu, Y.; Wang, J.; Joshi, P. P.; Niesner, D.; Williams, K. W.; Jin, S.; Zhu, X.-Y. Screening in Crystalline Liquids Protects Energetic Carriers in Hybrid Perovskites. *Science (80-.).* **2016**, *353* (6306).

(3) Shulenberger, K. E.; Bischof, T. S.; Caram, J. R.; Utzat, H.; Coropceanu, I.; Nienhaus, L.; Bawendi, M. G. Multiexciton Lifetimes Reveal Triexciton Emission Pathway in CdSe Nanocrystals. *Nano Lett.* **2018**, *18* (8), 5153–5158. https://doi.org/10.1021/acs.nanolett.8b02080.

(4) Kagan, C. R.; Murray, C. B.; Nirmal, M.; Bawendi, M. G. Electronic Energy Transfer in CdSe Quantum Dot Solids. *Phys. Rev. Lett.* **1996**, *76* (9), 1517–1520. https://doi.org/10.1103/PhysRevLett.76.1517.

(5) Chang, J.-Y.; Chang, Y.-A.; Wang, T.-H.; Chen, F.-M.; Liou, B.-T.; Kuo, Y.-K. Reduced Efficiency Droop in Blue InGaN Light-Emitting Diodes by Thin AlGaN Barriers. *Opt. Lett.* **2014**, *39* (3), 497. https://doi.org/10.1364/OL.39.000497.

(6) Bae, W. K.; Park, Y.-S.; Lim, J.; Lee, D.; Padilha, L. A.; McDaniel, H.; Robel, I.; Lee, C.; Pietryga, J. M.; Klimov, V. I. Controlling the Influence of Auger Recombination on the Performance of Quantum-Dot Light-Emitting Diodes. *Nat. Commun.* **2013**, *4* (1), 2661. https://doi.org/10.1038/ncomms3661.

(7) Goldsmith, R. H.; Moerner, W. E. Watching Conformational- and Photodynamics of Single Fluorescent Proteins in Solution. *Nat. Chem.* **2010**, *2* (3), 179–186. https://doi.org/10.1038/nchem.545.

(8) Becker, W.; Bergmann, A.; Biskup, C. Multispectral Fluorescence Lifetime Imaging by TCSPC. *Microsc. Res. Tech.* **2007**, *70* (5), 403–409. https://doi.org/10.1002/jemt.20432.

(9) Bruchez, M.; Moronne, M.; Gin, P.; Weiss, S.; Alivisatos, A. P. Semiconductor Nanocrystals as Fluorescent Biological Labels. *Science* **1998**, *281* (5385), 2013–2016. https://doi.org/10.1126/SCIENCE.281.5385.2013.

(10) Ma, X.; Hartmann, N. F.; Baldwin, J. K. S.; Doorn, S. K.; Htoon, H. Room-Temperature Single-Photon Generation from Solitary Dopants of Carbon Nanotubes. *Nat. Nanotechnol.* **2015**, *10* (8), 671–675. https://doi.org/10.1038/nnano.2015.136.

(11) Caram, J. R.; Bertram, S. N.; Utzat, H.; Hess, W. R.; Carr, J. A.; Bischof, T. S.; Beyler, A. P.; Wilson, M. W. B.; Bawendi, M. G. PbS Nanocrystal Emission Is Governed by Multiple Emissive States. *Nano Lett.* **2016**, *16* (10), 6070–6077. https://doi.org/10.1021/acs.nanolett.6b02147.

(12) Sandberg, R. L.; Padilha, L. A.; Qazilbash, M. M.; Bae, W. K.; Schaller, R. D.; Pietryga, J. M.; Stevens, M. J.; Baek, B.; Nam, S. W.; Klimov, V. I. Multiexciton Dynamics in Infrared-Emitting Colloidal Nanostructures Probed by a Superconducting Nanowire Single-Photon Detector. *ACS Nano* **2012**, *6* (11), 9532–9540. https://doi.org/10.1021/nn3043226.

(13) Carr, J. A.; Franke, D.; Caram, J. R.; Perkinson, C. F.; Saif, M.; Askoxylakis, V.; Datta, M.; Fukumura, D.; Jain, R. K.; Bawendi, M. G.; et al. Shortwave Infrared Fluorescence

Imaging with the Clinically Approved Near-Infrared Dye Indocyanine Green. *Proc. Natl. Acad. Sci. U. S. A.* **2018**, *115* (17), 4465–4470. https://doi.org/10.1073/pnas.1718917115.

(14) Cosco, E. D.; Caram, J. R.; Bruns, O. T.; Franke, D.; Day, R. A.; Farr, E. P.; Bawendi, M. G.; Sletten, E. M. Flavylium Polymethine Fluorophores for Near- and Shortwave Infrared Imaging. *Angew. Chemie - Int. Ed.* **2017**, *56* (42). https://doi.org/10.1002/anie.201706974.

(15) Bruns, O. T.; Bischof, T. S.; Harris, D. K.; Franke, D.; Shi, Y.; Riedemann, L.; Bartelt, A.; Jaworski, F. B.; Carr, J. A.; Rowlands, C. J.; et al. Next-Generation in Vivo Optical Imaging with Short-Wave Infrared Quantum Dots. *Nat. Biomed. Eng.* **2017**, *1* (4), 0056. https://doi.org/10.1038/s41551-017-0056.

(16) Hong, G.; Diao, S.; Chang, J.; Antaris, A. L.; Chen, C.; Zhang, B.; Zhao, S.; Atochin, D. N.; Huang, P. L.; Andreasson, K. I.; et al. Through-Skull Fluorescence Imaging of the Brain in a New near-Infrared Window. *Nat. Photonics* **2014**, *8* (9), 723–730. https://doi.org/10.1038/nphoton.2014.166.

(17) Gemmell, N. R.; McCarthy, A.; Liu, B.; Tanner, M. G.; Dorenbos, S. D.; Zwiller, V.; Patterson, M. S.; Buller, G. S.; Wilson, B. C.; Hadfield, R. H. Singlet Oxygen Luminescence Detection with a Fiber-Coupled Superconducting Nanowire Single-Photon Detector. *Opt. Express* **2013**, *21* (4), 5005. https://doi.org/10.1364/OE.21.005005.

(18) Natarajan, C. M.; Tanner, M. G.; Hadfield, R. H. Superconducting Nanowire Single-Photon Detectors: Physics and Applications. *Supercond. Sci. Technol.* **2012**, *25* (6), 63001.

(19) Marsili, F.; Verma, V. B.; Stern, J. A.; Harrington, S.; Lita, A. E.; Gerrits, T.; Vayshenker, I.; Baek, B.; Shaw, M. D.; Mirin, R. P.; et al. Detecting Single Infrared Photons with 93%

System Efficiency. *Nat. Photonics* **2013**, *7* (3), 210–214. https://doi.org/10.1038/nphoton.2013.13.

(20) Wu, J.; You, L.; Chen, S.; Li, H.; He, Y.; Lv, C.; Wang, Z.; Xie, X. Improving the Timing Jitter of a Superconducting Nanowire Single-Photon Detection System. *Appl. Opt.* **2017**, *56* (8), 2195. https://doi.org/10.1364/AO.56.002195.

(21) Robinson, B. S.; Kerman, A. J.; Dauler, E. A.; Barron, R. J.; Caplan, D. O.; Stevens, M. L.; Carney, J. J.; Hamilton, S. A.; Yang, J. K.; Berggren, K. K. 781 Mbit/s Photon-Counting Optical Communications Using a Superconducting Nanowire Detector. *Opt. Lett.* **2006**, *31* (4), 444. https://doi.org/10.1364/OL.31.000444.

(22) Takesue, H.; Nam, S. W.; Zhang, Q.; Hadfield, R. H.; Honjo, T.; Tamaki, K.; Yamamoto, Y. Quantum Key Distribution over a 40-DB Channel Loss Using Superconducting Single-Photon Detectors. *Nat. Photonics* **2007**, *1* (6), 343–348. https://doi.org/10.1038/nphoton.2007.75.

(23) Bertram, S. N.; Spokoyny, B.; Franke, D.; Caram, J. R.; Yoo, J. J.; Murphy, R. P.; Grein, M. E.; Bawendi, M. G. Single Nanocrystal Spectroscopy of Shortwave Infrared Emitters. *ACS Nano* **2018**. https://doi.org/10.1021/acsnano.8b07578.

(24) He, X.; Hartmann, N. F.; Ma, X.; Kim, Y.; Ihly, R.; Blackburn, J. L.; Gao, W.; Kono, J.; Yomogida, Y.; Hirano, A.; et al. Tunable Room-Temperature Single-Photon Emission at Telecom Wavelengths from Sp3 Defects in Carbon Nanotubes. *Nat. Photonics* **2017**, *11* (9), 577–582. https://doi.org/10.1038/nphoton.2017.119.

(25) Raymond, S. B.; Boas, D. A.; Bacskai, B. J.; Kumar, A. T. N. Lifetime-Based Tomographic Multiplexing. *J. Biomed. Opt.* **2010**, *15* (4), 046011.

https://doi.org/10.1117/1.3469797.

(26) and, J. C.; Selvin*, P. R. Lifetime- and Color-Tailored Fluorophores in the Micro- to Millisecond Time Regime. **2000**. https://doi.org/10.1021/JA9913986.

(27) Weihs, G.; Zeilinger, A. Photon statistics at beam-splitters: an essential tool in quantum information and teleportation http://copilot.caltech.edu/documents/278-weihs_zeillinger_photon_statistics_at_beamsplitters_qip.pdf (accessed May 21, 2019).

(28) Griffiths, P. R.; De Haseth, J. A. *Fourier Transform Infrared Spectrometry*; Hoboken, NJ, USA, 2007. https://doi.org/10.1002/047010631X.

(29) Clegg, R. M.; Schneider, P. C. Fluorescence Lifetime-Resolved Imaging Microscopy: A General Description of Lifetime-Resolved Imaging Measurements. In *Fluorescence Microscopy and Fluorescent Probes*; Springer US: Boston, MA, 1996; pp 15–33. https://doi.org/10.1007/978-1-4899-1866-6_2.

(30) Zheng, J. FRET and Its Biological Application as a Molecular Ruler. In *Biomedical Applications of Biophysics*; Humana Press: Totowa, NJ, 2010; pp 119–136. https://doi.org/10.1007/978-1-60327-233-9_5.

(31) Lakowicz, J. R. *Principles of Fluorescence Spectroscopy*; Springer, 2006.

(32) Perri, A.; Gaida, J. H.; Farina, A.; Preda, F.; Viola, D.; Ballottari, M.; Hauer, J.; De Silvestri, S.; D'Andrea, C.; Cerullo, G.; et al. Time- and Frequency-Resolved Fluorescence with a Single TCSPC Detector via a Fourier-Transform Approach. *Opt. Express* **2018**, *26* (3), 2270. https://doi.org/10.1364/OE.26.002270.

(33) Landry, M. L.; Morrell, T. E.; Karagounis, T. K.; Hsia, C.-H.; Wang, C.-Y. Simple

Syntheses of CdSe Quantum Dots. J. Chem. Educ. 2014, 91 (2), 274–279. https://doi.org/10.1021/ed300568e

(34) Chan, S.; Liu, M.; Latham, K.; Haruta, M.; Kurata, H.; Teranishi, T.; Tachibana, Y. Monodisperse and Size-Tunable PbS Colloidal Quantum Dots via Heterogeneous Precursors. J. Mater. Chem. C 2017, 5 (8), 2182–2187. https://doi.org/10.1039/C6TC05329G.

Chapter 3: Spectrally-selective Time-resolved Emission through Fourier-filtering (STEF)

We demonstrate a method for separating and resolving the dynamics of multiple emitters without the use of conventional filters. By directing the photon emission through a fixed path-length imbalanced Mach-Zehnder interferometer, we interferometrically cancel (or enhance) certain spectral signatures corresponding to one emissive species. Our approach, Spectrally-selective Time-resolved Emission through Fourier-filtering (STEF), leverages the detection and subtraction of both outputs of a tuned Mach-Zehnder interferometer, which can be combined with Time-correlated single photon counting TCSPC or confocal imaging to de-mix multiple emitter signatures. We develop a procedure to calibrate out imperfections in Mach-Zehnder interferometry schemes. Additionally, we demonstrate the range and utility of STEF by performing the following procedures with one measurement: 1) filtering out laser scatter from a sample, 2) separating and measuring a fluorescence lifetime from a binary chromophore mixture with overlapped emission spectra, 3) confocally imaging and separately resolving the standard fluorescent stains in bovine pulmonary endothelial cells and nearly overlapping fluorescent stains on RAW 264.7 cells. This form of spectral balancing can allow for robust and tunable signal sorting.

3.1 TCSPC and DAFS

Time-correlated single photon counting (TCSPC) uses the emitted photon stream to measure single emitter lifetimes,[1] intensity fluctuations,[2] classical/nonclassical photon correlations,[3] and material photophysical characteristics such as the relative polarization,[4] phase,[5] frequency,[6] and time of arrival.[3,7,8] However, this often involves tradeoffs between spectral resolution, throughput, and experiment time, which may limit the ability to resolve complex dynamics in heterogeneous mixtures.[1,9–11] Previously we developed Decay Associated Fourier Spectroscopy (DAFS) by utilizing a scanning Mach-Zehnder (MZ) interferometer. DAFS allows the ability to obtain simultaneous frequency and temporal information in the photon stream.[11] By avoiding losses and aberrations from monochromator gratings and slits, DAFS retains an optical output mode while concurrently being wavelength agnostic, sensitive to weak signals, and capable of resolving octave spanning signals. However, DAFS is relatively slow, with a typical spectrum requiring ~30 minutes to collect. To distinguish two signals at different frequencies, the use of specific optical filters is considerably more efficient.

Here we demonstrate that a MZ interferometer can act as a tuned optical Fourier domain filter through judicious choice of the MZ path length difference used to separate any two arbitrary and overlapping luminescence spectral signatures. We implement STEF (Spectrally- selective Time-resolved Emission through Fourier-filtering) for several different systems and show how it can be generalized and extended to applications in microscopy.

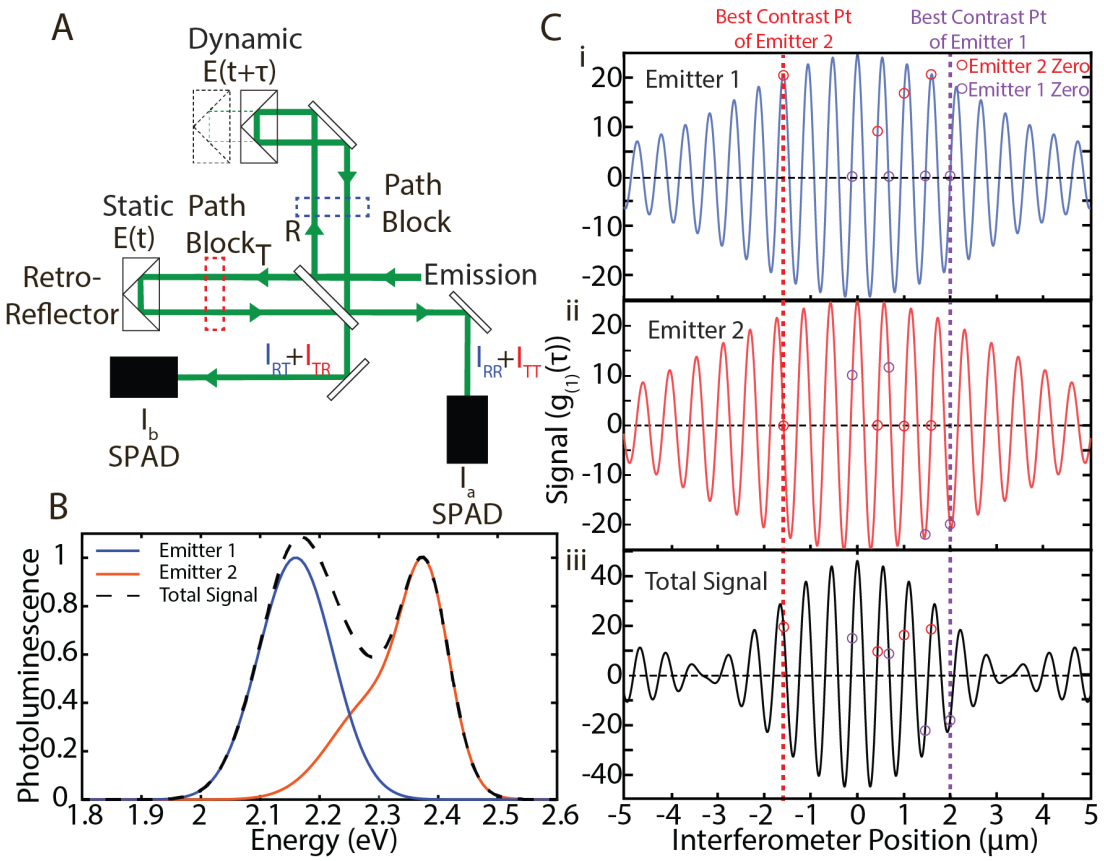

Figure 3.1 Fundamentals of Fourier Filtering

A. Folded Mach-Zehnder interferometer used for STEF. On one arm, the interferometer scans along a stage position on a dynamic delay stage, that defines the interferometer position for Fourier domain filtering, while the other arm remains static. Each path is blocked to record the respective interferometer imbalances. The imbalances are subtracted to recover more efficient filtering of the sample emission. B. Simulated example photoluminescence spectra of a solution with two spectrally overlapping emitters, blue (emitter 1) and orange (emitter 2) and the sum (dashed line) C. The real part of the Fourier transform for emitter 1, 2 and the combined signal. The points where each interference crosses zero is represented by the circles with their corresponding colors. The highest contrast zero-crossing is marked by the dashed lines.

3.2 Photoluminescence in Mach-Zehnder Interferometry

In our implementation of MZ interferometry, the incoming photon stream is directed through a beam splitter, separating the light into two paths where we introduce a variable delay (or phase shift) on one path using a retroreflector on a delay stage (Figure 3.1A); for a more rigorous description see our previous method paper, and supporting information (Figure 3.6).[11] At each output (labeled a and b), we use a single photon avalanche detector (SPAD) to time and measure weak photoemission. The photon stream intensity measured at b (I_b) is subtracted from that measured at a (I_a), recovering a signal proportional to the electric-field first-order correlation function, $g_1(\tau)$. For wide set stationary signals, $g_1(\tau)$ is the real part of the Fourier transform (FT) of the spectrum of emitted photons, *e.g.,* $\sigma(\omega)$, mathematically represented in equation 3.1:[12]

$$I_a - I_b \propto \frac{\langle E^*(t)E(t+\tau)\rangle}{|\langle E^*(t)E(t)\rangle|} = g_1(\tau) = Re\{FT[\sigma(\omega,\tau)]\} \qquad (3.1)$$

We plot an example photoluminescence (PL) $\sigma(\omega)$ for two emitters in Figure 1B.[13] In Figure 1C, we plot the FT of the PL spectrum for each emitter individually and the combined signal that would be measured from a mixture. In STEF, the stage position is set to the interferogram zero-point crossing for a particular emitter spectrum. We illustrate this in Figure 3.1C with the red dashed line, representing a position where emitter 2 is completely canceled out and the combined signal only represents signal contribution from only emitter 1. Similarly, emitter 2 can be isolated at the purple lined crossing positions. Red and purple circles represent other positions where emitter 2 and 1 can be canceled respectively. At any given zero-crossing, we obtain contrast between spectral components through a subtraction of detector signals. As all fluorescent signals have a carrier frequency, STEF can be applied to any lineshape and any arbitrary set of two (or more) emitter ensembles provided they have unique zero-crossings.

3.3 Finding Zero-Points

Each spectral component's interference pattern has many zero-crossing points. Finding the zero point can be done either by collecting an individual emitter's photoluminescence interferogram and determine the zero-crossing directly, or by Fourier transforming a measured individual emitter's photoluminescence spectrum. In our experiments, we used prior knowledge of the emission spectrum of one or both emitters collected through traditional photoluminescence measurements. Once the zero-point crossings are determined, one must select which one to use for spectral filtering. The optimal point will have the highest contrast, *e.g.*, position with the highest accumulated phase difference between the interferogram of emitters 1 and 2, while also selecting a point that is well separated from the other emitter's zero-points to limit cross-contamination. Thus, the contrast is a function of the carrier frequency and envelope, with narrower signals and different center frequencies leading to optimal contrast. While these considerations are like those for normal optical filters, the subtraction of signals allows us to completely cancel out a specific emitter's signal, which is not possible with a single filter and detector. It should be noted that the quality of Fourier filtering is dependent upon the contrast difference in the interferometer. This contrast would be similar if a set of filters were utilized instead because of signal loss that occurs from canonical filtering. We elaborate on this further in the discussion.

3.4 Correcting Non-Interferometric Imbalances

STEF relies on the cancellation of signals from each output of the MZ interferometer. However, the measured signal difference between each detector may arise due to (i) drift in the interferometer, (ii) differing efficiencies for each detector and (iii) imperfections in the reflection and transmission of the beamsplitter (or other optical elements after the beamsplitter). Drifting

may occur due to thermal fluctuations within the optical elements and/or laser output instability.[13–16] To address drift, we measured our Mach-Zehnder interferometer phase stability over the span of 2 hours, which is longer than a normal STEF measurement. Signals around 380 nm (the shortest wavelength where traditional silicon APDs function, and the worst-case scenario for phase instabilities) corresponded to a 62 cm^{-1} (7.7 meV) uncertainty in the filtering cut, i.e., two signals must be differentiated at least this much to separate them using STEF in our system. Though this phase shift is very small, it would result in imbalanced subtraction and less complete filtering. (Supporting Information: Figure 3.11). Further, we note that filtering at the zero-point crossing has the added advantage balanced detection, where symmetric fluctuations (such as laser drift) cancel out upon subtraction, adding further intrinsic stability to the STEF interferometric methodology.

To correct for detector and optical element imbalances, we perform two simple calibration measurements. We consider the signal measured at detector *a*/*b,* which is as follows:

$$I_{a,b} = \frac{\eta_{a,b}}{2} \varepsilon c \left| E_{a,b} \right|^2 \tag{3.2}$$

Where $\eta_{a,b}$ are the detector efficiencies respectively, ε is the dielectric permittivity in free space, and c is the speed of light. $E_{a,b}$ are the electric fields at *a, b*. As the path follows the beamsplitter we describe the electric field as a series of reflections and transmissions depending on the path:

$$E_a = RRE(t+\tau) + TTE(t) \tag{3.3}$$

$$E_b = RTE(t+\tau) + TRE(t) \tag{3.4}$$

where τ is the time separation induced by the path length difference. Here we assume that τ reflects a short time difference relative to the decay dynamics of the emitter (Figure 3.7), and thus the total intensity does not depend on the introduced delay, *e.g.,* $\langle I(t) \rangle = \langle I(t+\tau) \rangle$ We account for our imperfect beamsplitter efficiencies with the *R* (reflection) and *T* (transmission) beamsplitter

transfer functions $\hat{R} = \sqrt{\frac{\eta_R}{2}}$ and $\hat{T} = i\sqrt{\frac{\eta_T}{2}}$ (The i accounts for the $\frac{\pi}{2}$ phase change introduced by the beamsplitter.) $\eta_{T,R}$ are the efficiency terms of transmission and reflection respectively. Putting everything together, we can arrive at the following measured intensity at a:

$$I_{a,} = \frac{\eta_a}{2}\epsilon c\left[\frac{\eta_R^2}{4}|E(t+\tau)|^2 + \frac{\eta_T^2}{4}|E(t)|^2 - \frac{\eta_R\eta_T}{2}E^*(t)E(t+\tau)\right] \quad (3.5)$$

Or,

$$\langle I_a\rangle = \frac{\eta_a}{8}\varepsilon c\left(\eta_R^2 + \eta_T^2 - 2\eta_R\eta_T g^{(1)}(\tau)\right)\langle I(t)\rangle \quad (3.6)$$

The last term is the first-order correlation function $g^{(1)}(\tau)$.[17] The same can be done for the second detector:

$$\langle I_b\rangle = \frac{\eta_b}{4}\varepsilon c\left(\eta_R\eta_T + \eta_R\eta_T g^{(1)}(\tau)\right)\langle I(t)\rangle \quad (7.7)$$

To correct for unknown reflection and transmission terms, we block each path of the interferometer (Figure 3.2), and measure the intensity at *a* and *b*. We denote the intensity upon blocking each respective path as a series of *R* and *T* terms. For example, I_{aTT} is the intensity measured at *a* when the static retroreflector is blocked. Each path can give:

$$I_{xyz} = \frac{\eta_x}{4}\epsilon c\eta_y\eta_z\langle I\rangle \quad (3.8)$$

Where x is each detector and y and z are reflection and transmission terms. This gives the intensities of the blocked paths:

Thus, we can simplify equations 3.6 and 3.7 using blocked path intensities and the interference portion

$$\langle I_a\rangle = [\langle I_{aRR}\rangle + \langle I_{aTT}\rangle - \epsilon c\eta_a\eta_R\eta_T g^{(1)}(\tau)\langle I\rangle] \quad (3.9)$$

$$\langle I_b \rangle = \left(\langle I_{aRT} \rangle + \langle I_{aTR} \rangle + \epsilon c \eta_b \eta_R \eta_T g^{(1)}(\tau) \langle I \rangle\right) \qquad (3.10)$$

Combining equations 3.6 and 3.7 with the blocked interferometer measurements, the subtraction leaves only the interference terms.

$$\langle I_b \rangle - \langle I_a \rangle - (\langle I_{aRT} \rangle + \langle I_{aTR} \rangle) - (\langle I_{aTT} \rangle + \langle I_{aRR} \rangle) = I_{measured} \qquad (3.11)$$

$$I_{measured} = \epsilon c \eta_R \eta_T g^{(1)}(\tau)[\eta_a + \eta_b]\langle I \rangle \qquad (3.12)$$

3.5 Separating Excitation from Emission

As a proof of principle, we used STEF to separate laser scatter from sample PL (Figure 3.2). We use TIPS-pentacene (6,13-Bis(triisopropylsilylethynyl)pentacene) in hexane solution with an OD of 0.6. Using a 532 nm pulsed diode laser (LDH-P-FA-530B PicoQuant), we measure lifetime traces through the MZ interferometer using a pair of avalanche photodiodes (PD050-CTD, Micro Photon Devices). In Figure 2A, we show the spectra of the laser and TIPS-pentacene and in Figure 3.2B., the respective interference collected with the MZ interferometer. The interferometer is set to zero-point crossing (Figure 3.2B) which filters out the laser (red dashed line) and TIPS-pentacene (blue dashed line) fluorescence signal respectively. We recorded TCSPC traces with the interferometer open (Figure 3.2C), the static retroreflector blocked, and the moving retroreflector blocked (Figure 3.8). After subtraction and correction, the laser and TIPS-pentacene signals were successfully isolated (Figure 3.2D). As expected, the laser signal matches instrument response function. The STEF resolved TIPS-pentacene signal is identical to a standard TIPS-pentacene lifetime decay acquired by measuring the lifetime of TIPS by itself in an unmixed system. The TIPS standard and TIPS STEF give equivalent lifetimes. This demonstrates the powerful utility

of STEF in filtering out laser scatter, which is often detrimental in imaging and spectroscopic measurements.

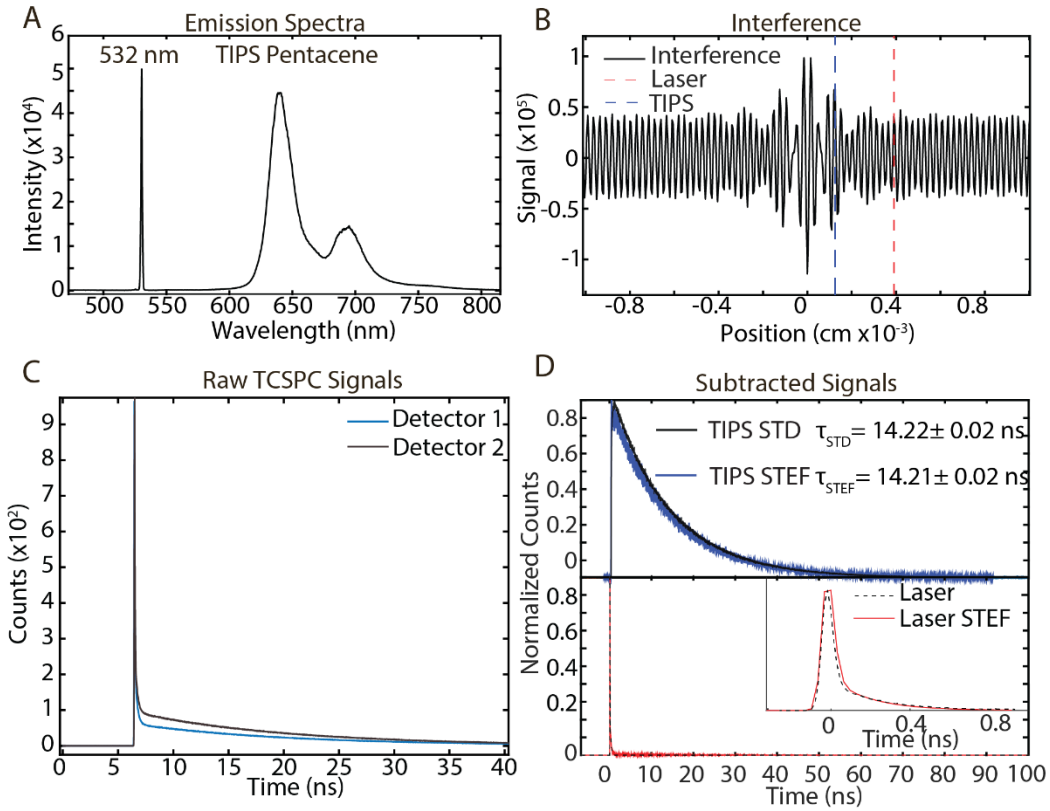

Figure 3.2 Fourier Filtering of Laser and Emission

A. The measured emission spectra of the laser and emitter. B. The corresponding interferogram ($g_1(\tau)$) collected with the MZ interferometer. Each dashed line represents the zero-point crossing where either the laser (orange dashed line) or TIPS (blue dashed line) are filtered. C. The TCSPC lifetime from each detector retrieved before balance correction and implementing STEF analysis. D. After subtraction and correction the signals can successfully separate yielding the lifetime of TIPS pentacene (top) and the laser limited instrument response function (bottom). The TIPS STEF is compared to the sample's lifetime by itself and without mixed (TIPS STD). Data is fit to a single exponential.

3.6 Separating Two Emitters

We next employed STEF in a binary mixture of rubrene and TIPS-pentacene in a hexane solution (Figure 3.3A) with a similar excitation-collection setup as above, but with an added 533 nm laser notch filter (NF533-17, Thorlabs). TIPS-pentacene and rubrene were used at an absorbance ratio of 0.63:0.57 OD respectively. This demonstrates the generality of STEF's ability to separate signals of arbitrary spectral shape, even with spectral overlap. We observed the dynamics of each component separately without the use of any additional filters with the exception of a 533 nm laser notch filter. The STEF lifetime traces of the TIPS-pentacene and rubrene mixture components match their single component solution counterparts (Figure 3.3B) with the exponential fits agreeing within experimental error. This successfully shows the applicability of STEF for mixed chromophore systems.

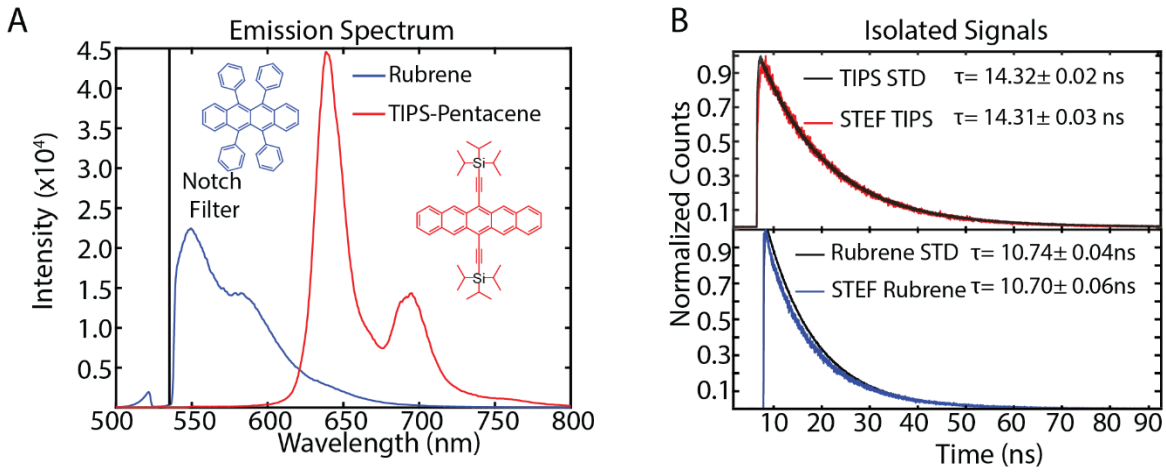

Figure 3.3 Fourier Filtering of Overlapping Emission Signals

A. Emission spectrum of the two-emitter system, Rubrene and TIPS-pentacene. A 533-notch filter was used throughout the experiment to filter out the laser and maintain a two-component system. The two emitters were excited using a 532-diode laser. B. The resulting lifetimes from the subtraction each compared with the lifetimes of each unmixed emitter. The similar lifetimes demonstrate STEF's ability to successfully subtract and isolate emissions - even with molecules of similar lifetimes.

3.7 Separating Emission Channels in Cellular Imaging

Finally, we show the breadth of STEF's utility by implementing the method in the context of imaging. We performed confocal microscopy to simultaneously image multiple fluorescent channels of stained bovine pulmonary artery endothelial cells (ThermoFisher, FluoCells™ Prepared Slide #1). Using a homebuilt inverted microscope setup (Figure 3.6) with a piezo stage (Mad City Labs Nano-View/M 200-3) and an 100x oil objective (Nikon, Plan APO 100x/NA=1.45), absolute intensities were collected while scanning across the sample. The scan had a dwell time of 100 ms, resulting in a collection time of 20 minutes. No filters were used other than a 533 notch filter to block direct laser scatter. Figure 4A shows a confocal image of the sample without any spectral filtering to discriminate the dye-stained features. We separated the fluorescence from the DAPI (4′,6-diamidino-2-phenylindole) DNA stain (Figure 4B) from the MitoTracker™ Red CMXRos mitochondria stain (Figure 4C) without filters. We first set the interferometer to a zero-crossing point and then performed a confocal imaging scan, with the signal from two detectors summed (Figure 3.4A).

The resulting images from each detector are processed by subtraction to obtain the isolated emissions image from each dye, all from a single experiment. This can be extended to any number of dyes. Each zero-crossing point can be treated as filtering one signal while leaving the ensemble mixed. A careful series of subtractions successfully isolates any desired single emission from a mix of emissions. Figure 3.4D shows that STEF correctly resolved the blue-stained DNA in the cell nucleus from the surrounding, red-stained mitochondria and allowed for the tuning of whatever signal ensembles appropriate for the system, confirming its general scope in biological or other imaging applications. This approach does not implement time-resolved

measurements but could be easily applied for filtering in fluorescent lifetime imaging microscopy (FLIM) measurements. In FLIM, the measurement time can vary depending on the fluence of emitted photons. However, given the brightness of dyes, the dwell time would not change significantly.

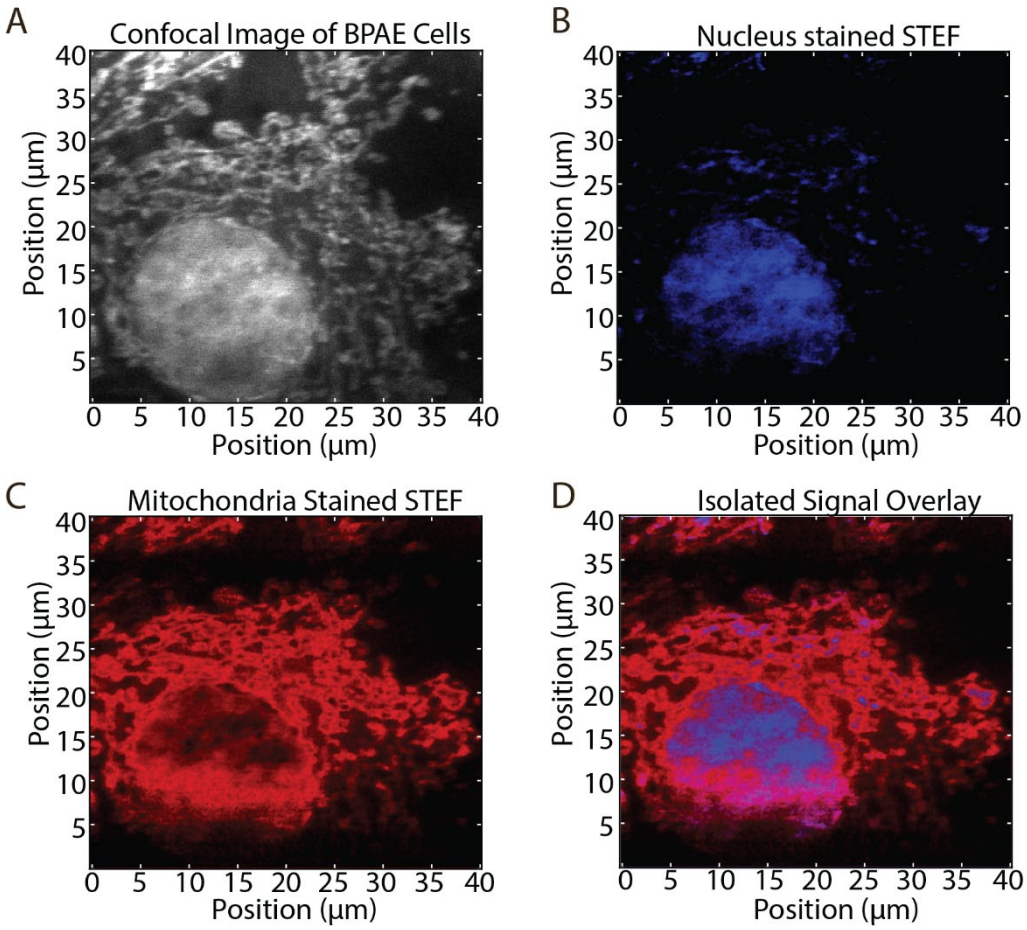

Figure 3.4 Fourier Filtering of Overlapping Emission Signals

Imaging of stained bovine pulmonary artery endothelial cells using unfiltered scanning confocal fluorescence microscopy B. STEF scanning microscope image of nucleus stained with DAPI with MitoTracker™ Red CMXRos filtered. C. STEF scanning microscope image of the mitochondria stained with MitoTracker™ Red CMXRos with DAPI filtered. D. Combined image overlay of the nucleus stained with DAPI filtered emission and mitochondria stained with MitoTracker™ Red CMXRos filtered emission.

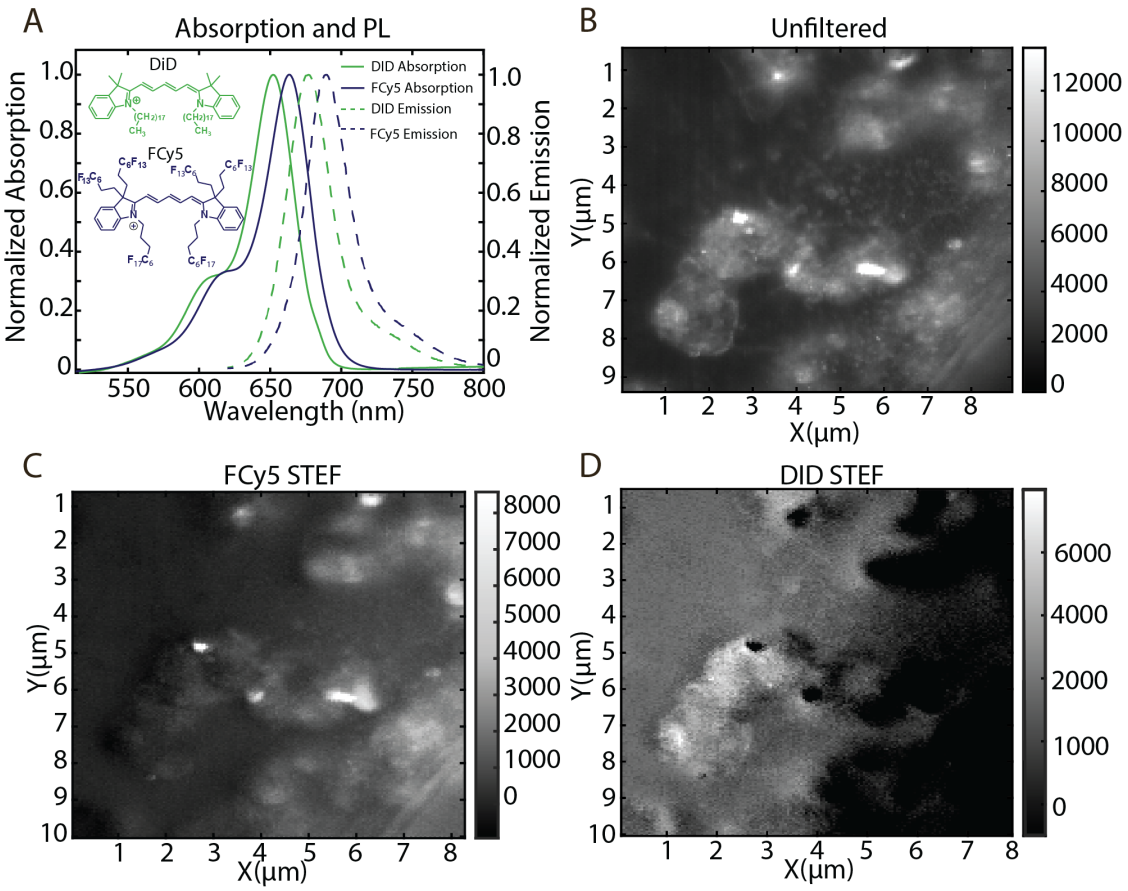

Figure 3.5 Fourier Filtering of Extreme Emission Overlap

A. Absorption and emission spectra of DID and FCy5, peaks are separated by 13 nm. B. Imaging of stained RAW264.7 cells using unfiltered scanning confocal fluorescence microscopy C. STEF scanning microscope image of lysosome stained with FCy5 with DID filtered. D. STEF scanning microscope image of the membrane DID with FCy5 filtered.

As a final proof of principle, a macrophage cell line (RAW264.7) was treated with two heptamethine carbocyanine dyes: DiD (1,1-dioctadecyl-3,3,3,3-tetramethylindodicarbocyanine,4-chlorobenzenesulfonate) and FCy5. DiD is a lipophilic fluorophore that associates with membranes and lipid droplets within the cell. FCy5 is a fluorous soluble fluorophore that is introduced by perfluorocarbon nanoemulsions that are internalized by endocytosis and label the endosomes/lysosomes.[18–20] The staining protocol can be found in Figure 3.10. These dyes had very similar line shapes and emission spectra, with the maxima spaced 13 nm apart (Figure 3.5A). The zero-point crossing positions were chosen to maximize

contrast in the combined signal while maintaining adequate separation between zero crossing points stage positions of the different emitters. The total image (Figure 3.5B) was obtained in a similar manner as above while sitting on a singular position. After this, the subtractions obtained yielded a successful separation of FCy5 (Figure 3.5C) and DiD (Figure 3.5D). The successful filtering of these two dyes has demonstrated STEF's ability to also separate similar dyes that overlap without specialty filters.

3.8 Comparison to Other Methods

Several Fourier domain filtering methods have been previously explored.[13,21–23] Most similarly, Candeo *et al.* gives a complementary interferometric approach for separating fluorescent signals.[24] Their method implements Translating-Wedge-based Identical pulses eNcoding System (TWINS) to direct an emitted photon stream directed through a single-output common-path birefringent wedge interferometer. In their implementation, they collect the emitted photon stream and direct it through the interferometer, imaging at a maxima of the interference pattern. As TWINS is a common path interferometer with minimal moving parts, it offers high stability and accuracy. However, due to the single path and output it forgoes the advantages of a two detector MZ balanced detection scheme. Hence, STEF uses a single measurement to obtain: the total binary solution lifetime trace, as well as each individual lifetime component. TWINS can only decrease the signal from one signature without completely canceling it out.

More commonly, optical filter elements such as long, short, and band pass filters provide a simple method to filter fluorescent signatures. However, these approaches cannot fully cancel a specific spectrum. Designing an analogous filter system would require a beamsplitter which "splits" the spectrum at equal intensity to each detector, which would enable perfect subtraction. Similar

approaches have been used to explore spectral diffusion but lack the flexibility of a tunable Fourier domain filter and are limited by the cost and availability of optical components.[25] STEF may filter out any arbitrary shape desired by the user including instances of significant spectral overlap. Monochromators with gratings provide some tunability, however, like filters they are limited to selecting spectral bands (by the exit slit) as opposed to spectral shapes. Furthermore, monochromators sacrifice throughput and optical mode for spectral resolution as defined by the grating lines/mm, slit width, and path length of the spectrometer.[26] STEF retains the complete sample emission (mode and intensity), allowing for higher throughput and tunability even at high resolution ($0.1 cm^{-1}$), dictated by scanning length of the stage. STEF two path/output methodology cancels signals in mixed samples while leveraging the above advantages to acquire isolated signals for lifetimes and imaging as demonstrated below.

3.9 Conclusion

As demonstrated, STEF is a powerful tool to separate spectral signatures by leveraging differences in the carrier frequency and coherence length. This avoids difficulties often encountered in systems with emission overlap and complicated line shapes which lead to signal contamination. The practical consideration of STEF's contrast is set by the difference in carrier frequency (or the accumulated phase difference between signals), and their coherence length (the width of the spectrum). Therefore, STEF works best when two signals are separated in energy (carrier frequency), and are narrow (large coherence lengths), paralleling traditional filters. With these factors in mind, STEF presents the advantage of overall tunability and specificity to arbitrary desired signals, working well in cases of overlapping spectral signatures and without requiring specialized filters. It should also be emphasized that STEF leverages the Mach-Zehnder interferometer and only requires two detectors for any number of emitters in solution. Because of

this, any mixed sample can be isolated through a series of subtractions with the number of measurements being N-1 where N is the number of emitters. Mach-Zehnder's phase shift sensitivity offers an avenue of advantages including wavelength-range insensitivity, drift-noise cancellation, and optical mode retention. Hence, we were able to demonstrate separation of the emission from a laser and chromophore, two separate chromophores, and imaging of two channels in a stained cellular environment with strongly overlapped spectral signatures. These demonstrations show STEF's wide utility across disciplines in spectroscopy, solution analysis, material science, and biological imaging.

3.10 Supplementary Information

STEF Setup

Experiments were conducted on a home-built optical microscope. All samples were excited by either a 532 or 405 nm pulsed diode laser (LDH-P-FA-530B, or LDH-P-C-405 PicoQuant, respectively). For TCSPC experimental examples shown in figures 3.7 and 3.8, epifluorescence of the sample was collected through the microscope using a 40x objective (Nikon MRD00405). Rubrene and TIPS-Pentacene were excited using a 532 nm laser which was filtered out with a 533 notch filter (NF533-17, Thorlabs) and a 550 nm longpass filter employed through a dichroic beamsplitter (DMLP550R, Thorlabs). The filtered emission was then sent through the MZI: the PL was passed through a 50:50 beamsplitter plate (Thorlabs BSW10R) with one path containing a fixed hollow retroreflector (Newport UBBR2.5-5S) and the other directed to linear translational stage (ANT-95L-050, Aerotech). We introduce a compensator plate (Thorlabs BCP43R) to be able to fix any dispersions introduced by the BS that may result in a chirp or chromaticity introduced by the beam splitter. The output of each path is recombined at different spot on the same 50:50

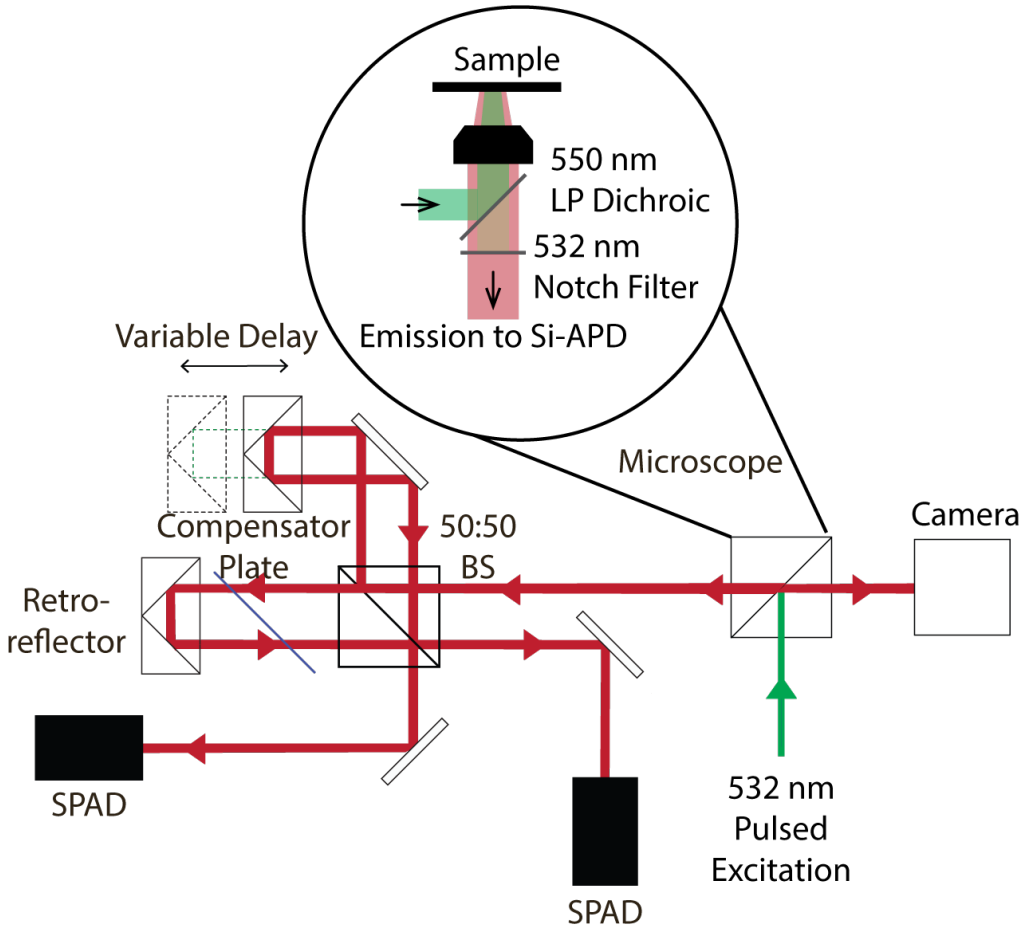

Figure 3.6 General Scheme of STEF

Optical apparatus built for STEF measurements. Measurements were collected through the epifluorescence collected from a custom-built microscope. The emission signal was then sent through a Mach-Zehnder (MZ) interferometer. The interferometer utilizes a 50:50 beamsplitter (BS) and a compensator plate to adjust for chirp in the interference. Positions in the interference are found using a retroreflector on dynamic linear stage. Signal was finally measured using single-photon avalanche diodes (SPADS) on each arm of the interferometer

beamsplitter plate. The interferometer was scanned using a linear stage that moved at constant velocity. When measuring STEF, the stage positions were static. The two outputs of the interferometer are focused onto avalanche photodiodes (APDs) (PD050-CTD, Micro Photon Devices). Photon streams are timed by a HydraHarp 400 (Picoquant) in Time-Tagged Time-Resolved (TTTR) mode. To adjust for any after pulsing seen in the detectors multiple photon

events concurring in the same pulse were filtered out. This was accomplished by removing the latter photon if the time between the two photons was less than the detectors deadtime (~63 ns).

For the imaging experiments shown in Figure 3.9 and Figure 3.10, upon excitation, the epifluorescence is sent through a similar path for filtering. Widefield images (Figure 3.9 and 3.10) were acquired by introducing a dispersing lens before excitation and directing the emission at a sCMOS camera (Zyla sCMOS, Andor). The scanning images seen in Figure S4 were taken with the sample fixed to a piezo stage (Mad City Labs Nano-View/M 200-3) using an 100x oil objective (Nikon MRD01905). The samples in Figure 3.10, however, were collected using a scanning galvometer mirror system (Thorlabs GVS012). Emission is then sent through the STEF setup as described above. For scanning, however, we record overall intensities instead of lifetimes.

Separating Evolving Signals in Time

In Figure 3.7, we present an evolving signal from an impulsive excitation, and how we can use STEF to separate time-evolving signals. For example, after an impulsive excitation (for example, by an ultrafast laser), the photoluminescence from an ensemble of emitters can be thought of as a rapidly oscillating electric field whose overall amplitude in proportion to the excited state population (Figure 3.7A). This signal evolves with a global time t. Therefore, we can express the electric field as

$$E(t) = A(t)^{1/2}\{exp(i\omega_0 t)exp(i\phi[t])\} \qquad 3.13$$

Where $A(t)$ is an envelope function, ω_0 is the optical carrier frequency, and $\phi(t)$ is a phase function which represents the rapidly changing phase of the ensemble of emitters (example shown in inset of figure 3.7a). MZ interferometry allows us to extract $g_1(\tau)$

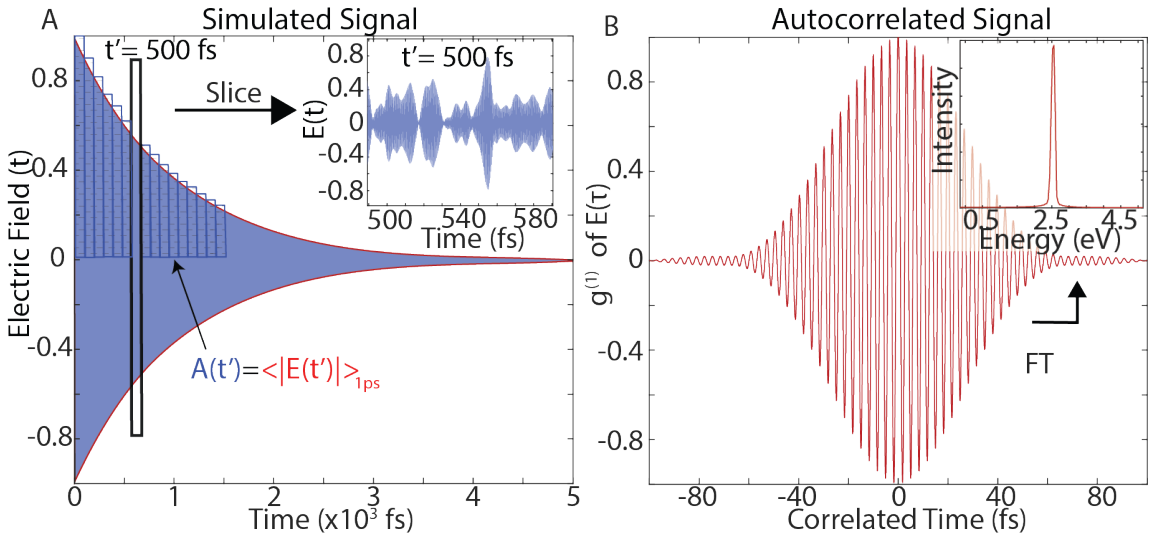

Figure 3.7 Isolating Evolving Figures in Time

A. Simulated signals from a fluctuating oscillating electric field with a decaying average amplitude. A faster time scale (500 fs) in comparison to overall signal is separated. B. This separated signal is autocorrelated revealing the interferometric pattern which can then we easily Fourier transformed to give the emission spectra of that signal.

MZ interferometry allows us to extract $g_1(\tau)$:

$$g_1(\tau) = \frac{\langle E^*(t)E(t+\tau)\rangle}{|\langle E^*(t)E(t)\rangle|} = \cos(\omega_0\tau)\,\Phi(\tau), \qquad 3.14$$

where $\Phi(\tau) = \frac{\langle \phi^*(t)\phi(t+\tau)\rangle}{|\langle \phi(t)\rangle|^2}$. By inspection, we can see that the random fluctuations in the electric field are identical to the linewidth in equation 2. We show a typical first order correlation function Figure 3.7B. In the inset, we show the real part of the Fourier transform of the spectrum, which will always have a corresponding zero-point in the MZ interferogram. We will assume that $A(t) = A(t+\tau)$ for short τ. This allows us to treat the path length difference between interferometer legs as not inducing a change in the measured TCSPC histogram. Simply put, the coherence time of

the electric field (τ_c) must be less than the bin-width. A 10 meV linewidth corresponds ~500 fs coherence length, considerably shorter than typical bin and instrument response functions in TCSPC.

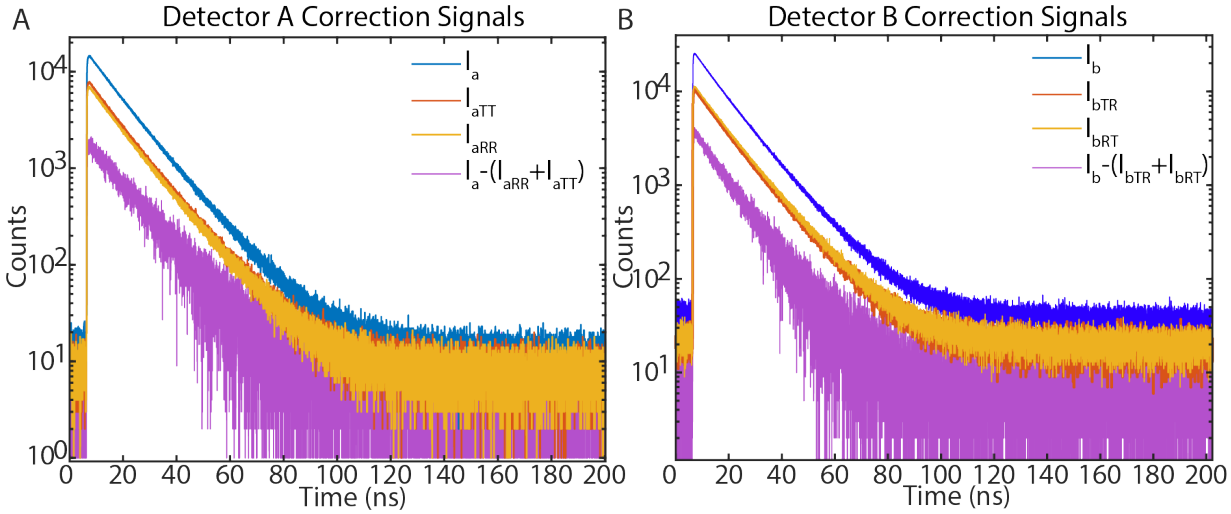

Figure 3.8 Sample TCSPC's Collected During Imbalance Corrections

An example of each of the measurements taken for the TIPS-Pentacene for both detectors (A and B). Each TCSPC is collected with the imbalance corrections added together. The addition of the imbalances are then subtracted from the total signal collected when the interferometer is unblocked and interfering. The corrected signal for each detector is then subtracted from the other detector's corrected signal resulting in the STEF measurement shown in the main tex.

All Signals Before Correction.

In Figure 3.8, we show the measured TCSPC of the subtracted/measured signals for each detector used in the Rubrene/TIPS pentacene experiment. I_A and I_B represent the intensity at each detector, while subscript represent blocking one path of the interferometer as described in the main text. These terms are then added together and subtracted from the total detector signal collected when the arms are unblocked. Once these corrections are made the two detectors are subtracted yielding the STEF results shown in the main text.

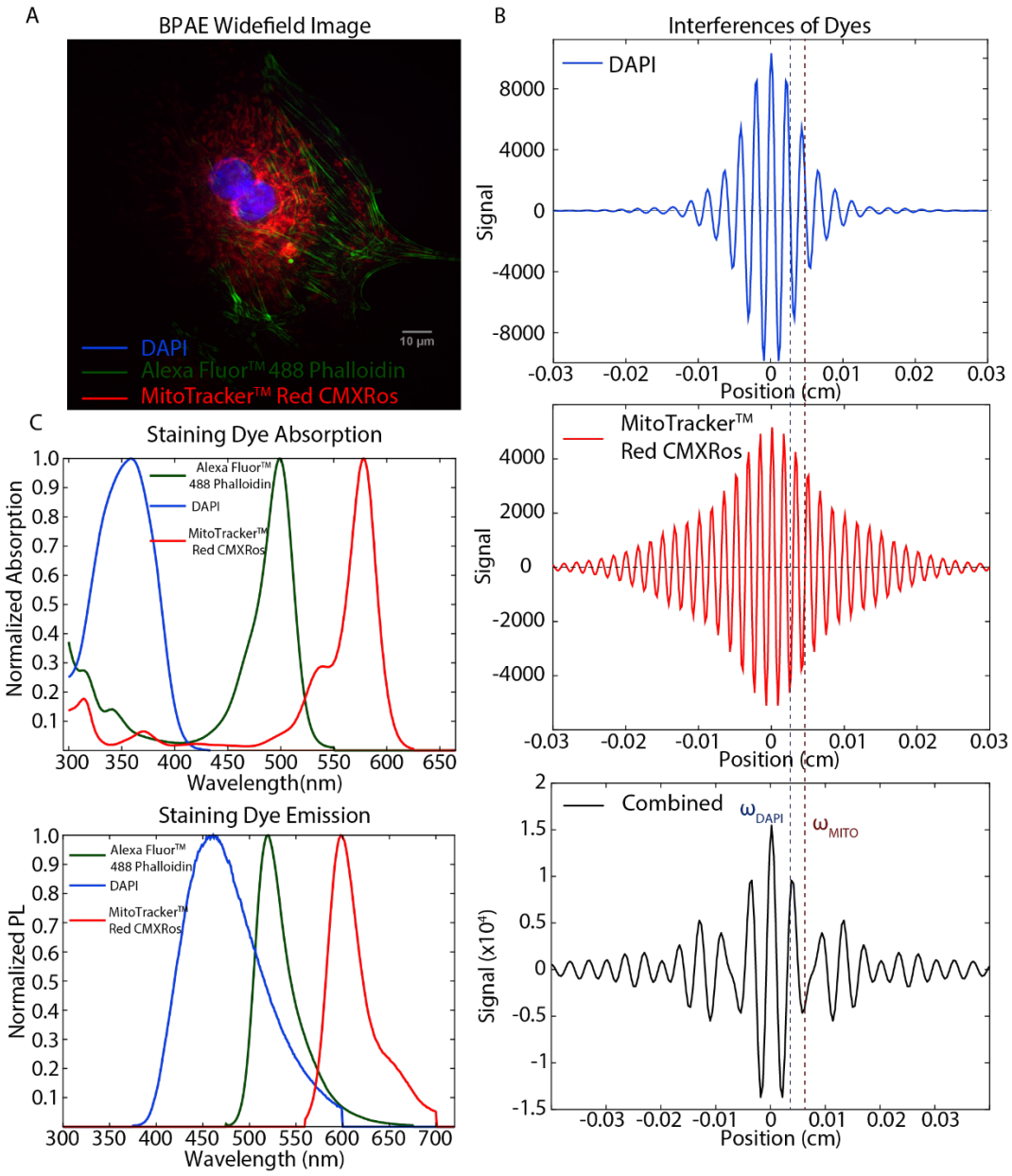

Figure 3.9 Widefield Image and Spectra of BPAE

A. Overlay of the different dyes in the BPAE cells initially imaged with a sCMOS camera (Zyla sCMOS, Andor) and their relative normalized B (top) absorption and (bottom) emission spectra. B. Fourier transforms of the emission spectra used to find zero crossing point. The points used for DAPI and MitoTracker Red were at 21.4 um and 49.0 um away from the center burst respectively. C. (top) absorption and (bottom) emission spectra

BPAE Cells Used for Imaging

BPAE Cells (Invitrogen Thermofisher FluoCells™ Prepared Slide #1) were used as the first imaging proof of principle. Here, we collect an initial image of the three dyes and their initial spectra. DAPI emission was collected with a 405 nm laser and a stack of 420 nm longpass filter and BG3 bandpass color glass filter (315nm-445nm, 715nm-1095nm). AlexaFluor emission was collected using a 405 nm laser and a 515 nm longpass filter, a 550 nm shortpass, and a 533 notch filter. Finally the MitoTracker™ Red was collected with a 532 nm laser and the BG3 bandpass color glassed filter.

S5 RAW 264.7 Cells

Live cells were treated with DiD and FCy5 dye. A FCy5 emulsion was created by dissolving 5 nmol of FCy5 dye in 20 μL of perfluorooctyl bromide (PFOB).[27–29] Then, 200 μL of 28 wt% Pluronic F-68 surfactant was added to the top of the PFOB layer. Solutions were sonicated using a probe sonicator at 35% amplitude for 90 seconds at 0 °C. The DiD stain was prepared as a 1 mg/mL stock in DMSO.

RAW264.7 cells were plated on an 8 (45,000 cells/well) or 2 (225,000 cells/well) chamber well slide (IDBI) in 5% fetal bovine serum (FBS) Dulbecco's Modified Eagle Medium (DMEM) containing penicillin-streptomycin. Cells were allowed to adhere onto the slides for 24 hours. Media was then aspirated, and the cells were washed with PBS. The FCy5 emulsions were then added into the wells (8 chamber slide 40 μL of emulsions per well) with DMEM media and incubated for 3 hours at 37 °C.

After incubation, the media was aspirated again. The cells were then washed with media and LiCl Buffer in triplets and followed up with a single PBS buffer wash. A 1:1000 dilution of DiD stock

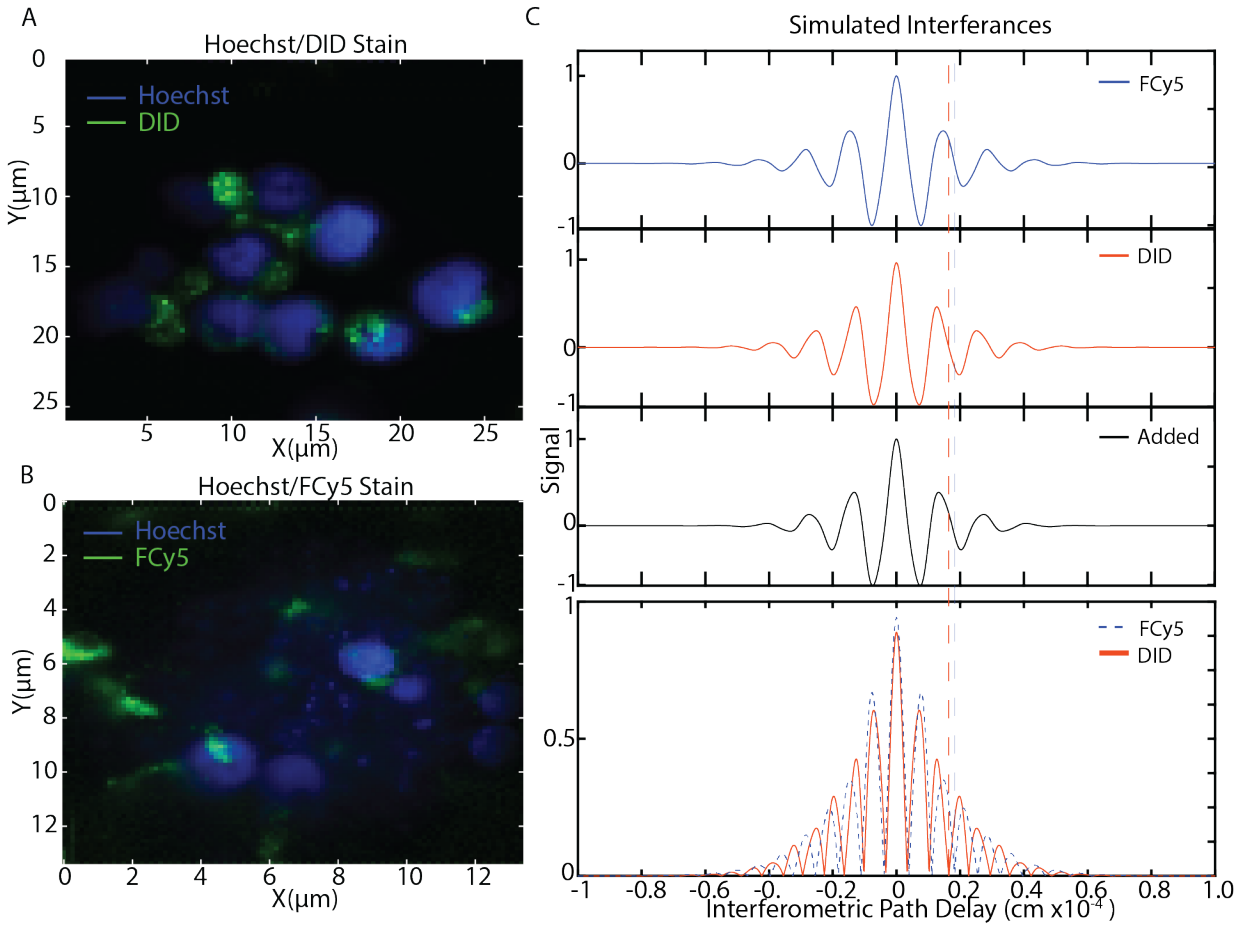

Figure 3.10 Confocal Images and Fourier Spectra of RAW Cells

A. Control confocal image of the DiD and Hoescht dye staining in the RAW cells B. Control confocal image of the FCy5 and Hoescht dye staining in the RAW cells C. Fourier transforming the emission spectra used to find zero crossing point. The points used for DiD and FCy5 were at 0.163 µm and 0.187 µm away from the center burst respectively.

was then added to the cells, incubated at room temperature for 20 minutes, and washed with PBS twice. If nuclear staining was required a 1:10000 diluted from a 1 mg/mL Thermofisher Hoechst 33342 working stock in PBS was added to the cells and incubated at room temperature for 10 minutes. The cells were washed twice with PBS. Coverslips were placed to the top of the chamber well and sealed with clear nail polish.

Controls were used to identify and verify dye localization within the cells. A confocal scan was used to collect intensity traces of FCy5 and Hoechst (Figure 3.10A) in cells only and Hoechst and

Hoechst only (Figure 3.10B)[27,28]. The simulated interferences calculated (Figure 3.10C) yielded very closely spaced zero-point crossings. However, because the stage used was within a degree of error where these positions did not cross or mix this did not become an issue. The points were selected such that the positions were adequately far apart from each other while still having large contrast in the total signal.

Drift Calculations in the Interferometer

We describe the wavelength drift we find in STEF that could cause any wavelength variations in the calculated zero-point crossing points. We start using an equation detailed in the following paper[11]:

$$S(\delta') = S_a(\delta') - \left(\frac{\eta_a}{\eta_b}\right) S_b(\delta') - mean\left[S_a(\delta') - \left(\frac{\eta_a}{\eta_b}\right) S_b(\delta')\right]_{\delta'} \qquad 3.15$$

$$= \sum_i \dot{N} \cos(\delta k_i)$$

Where $S_{\frac{a}{b}}$ are the detector signals, $\eta_{\frac{a}{b}}$ are the detector efficiencies, $\dot{N}$ is the rate of sample photon emission, δ is the interferometer retardation, k is the wavevector of the photon: $k_i = \frac{\omega}{c} = \frac{2\pi}{\lambda}$

$$\delta = \left(\frac{2\pi}{\lambda}\right) \cos^{-1}\left[\frac{S_a(\delta') - \left(\frac{\eta_a}{\eta_b}\right) S_b(\delta') - mean\left[S_a(\delta') - \left(\frac{\eta_a}{\eta_b}\right) S_b(\delta')\right]_{\delta'}}{S_a(\delta') + S_a(\delta')}\right] \qquad 3.16$$

After sitting in a single position for a long duration of time we can correlate the two detectors as a function of counts (Figure 3.11A). We then plot the function according to equation 3.16 (Figure 3.11B) and take the standard deviation. Using the standard deviation, we can find the drift in wavelength that is a result of uncorrelated noise. The interferometric drift is found to be 0.007 nm.

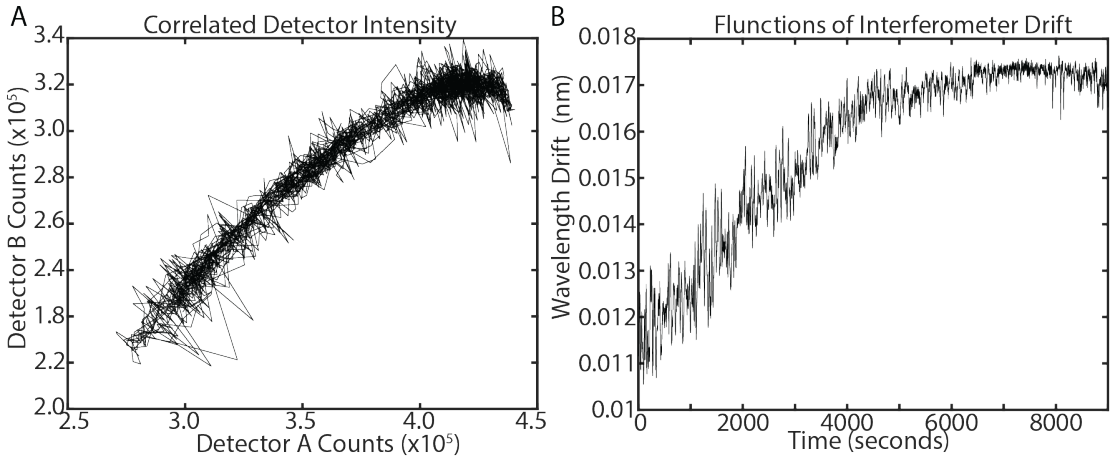

Figure 3.11 Interferometer Drift

A. The counts of each detector plotted in respect to each other while sitting on a stage position for 2 hours. The slanted aspect of this is considered the correlated signal. B. Equation 3.16 plotted with y axis as the δ this is fluctuations of interferometer drift

References

1. Jian Cui, P. Beyler, A., S. Bischof, T., B. Wilson, M. W. & G. Bawendi, M. Deconstructing the photon stream from single nanocrystals: from binning to correlation. Chem Soc Rev 43, 1287–1310 (2014).

2. Schlegel, G., Bohnenberger, J., Potapova, I. & Mews, A. Fluorescence Decay Time of Single Semiconductor Nanocrystals. Phys Rev Lett 88, 137401 (2002).

3. Rigler, R. & Elson, E. S. Fluorescence Correlation Spectroscopy: Theory and Applications. in Springer Series in Chemical Physics vol. 65 (Springer-Verlag Berlin Heidelberg, 2001).

4. Kliger, D. S., Lewis, J. W. & Randall, C. E. Polarized Light in Optics and Spectroscopy - David S. Kliger, James W. Lewis - Google Books. Academic Press, Inc (1990) doi:10.1016/C2009-0-22282-3.

5. Terasaki, A., Tokunaga, E. & Kobayashi, T. Frequency-domain interferometer for femtosecond time-resolved phase spectroscopy. Optics Letters, Vol. 17, Issue 16, pp. 1131-1133 17, 1131–1133 (1992).

6. Valeur, Bernard. & Berberan-Santos, M. Nuno. Molecular Fluorescence : principles and applications. (Wiley-VCH, 2013).

7. Schlawin, F. Entangled photon spectroscopy. Journal of Physics B: Atomic, Molecular and Optical Physics 50, 203001 (2017).

8. Loumaigne, M., Vasanthakumar, P., Richard, A. & Débarre, A. Time-of-Flight Photon Spectroscopy: A Simple Scheme To Monitor Simultaneously Spectral and Temporal Fluctuations of Emission on Single Nanoparticles. ACS Nano 6, 10512–10523 (2012).

9. Crouch, C. H. et al. Facts and Artifacts in the Blinking Statistics of Semiconductor Nanocrystals. Nano Lett. 10, 1692–1698 (2010).

10. Ambrose, W. P. & Moerner, W. E. Fluorescence spectroscopy and spectral diffusion of single impurity molecules in a crystal. Nature 1991 349:6306 349, 225–227 (1991).

11. Atallah, T. L. et al. Decay-Associated Fourier Spectroscopy: Visible to Shortwave Infrared Time-Resolved Photoluminescence Spectra. J Phys Chem A 123, 6792–6798 (2019).

12. Caram, J. R. et al. PbS Nanocrystal Emission Is Governed by Multiple Emissive States. Nano Lett 16, 6070–6077 (2016).

13. Ellis, J. D., Spronck, J. W., Joo, K.-N., Kan, P. J. M. van & Schmidt, R. H. M. Simple heterodyne laser interferometer with subnanometer periodic errors. Optics Letters, Vol. 34, Issue 3, pp. 386-388 34, 386–388 (2009).

14. Hou, W. & Wilkening, G. Investigation and compensation of the nonlinearity of heterodyne interferometers. Precis Eng 14, 91–98 (1992).

15. Xie, Y. & Wu, Y. Zeeman laser interferometer errors for high-precision measurements. Applied Optics, Vol. 31, Issue 7, pp. 881-884 31, 881–884 (1992).

16. Fu, H., Wu, G., Hu, P., Tan, J. & Ding, X. Thermal Drift of Optics in Separated-Beam Heterodyne Interferometers. IEEE Trans Instrum Meas 67, 1446–1450 (2018).

17. Scully O., M. & Zubairy Suhail, M. Quantum Optics. (Cambridge University Press, 1997). doi:10.1017/CBO9780511813993.

18. Day, R. A. & Sletten, E. M. Experimental Perspectives on Direct Visualization of Endosomal Rupture. ChemBioChem 22, 3277–3282 (2021).

19. Sutton, E. J., Henning, T. D., Pichler, B. J., Bremer, C. & Daldrup-Link, H. E. Cell tracking with optical imaging. Eur Radiol 18, 2021–2032 (2008).

20. Lim, I. et al. Fluorous Soluble Cyanine Dyes for Visualizing Perfluorocarbons in Living Systems. J Am Chem Soc 142, 16072–16081 (2020).

21. Mosier-Boss, P. A., Lieberman, S. H. & Newbery, R. Fluorescence Rejection in Raman Spectroscopy by Shifted-Spectra, Edge Detection, and FFT Filtering Techniques. Appl Spectrosc 49, 630–638 (2016).

22. Rossi, T. M. & Warner, I. M. Fourier Transform Filtering of Two-Dimensional Fluorescence Data: Appl. Spectrosc. 38, 422–429 (1984).

23. Lieber, C. A. & Mahadeven-Jansen, A. Automated Method for Subtraction of Fluorescence from Biological Raman Spectra. Appl. Spectrosc. 57, 1363–7 (2003).

24. Candeo, A. et al. A hyperspectral microscope based on an ultrastable common-path interferometer. APL Photonics 4, 120802 (2019).

25. Fernée, M. J. et al. Spontaneous spectral diffusion in CdSe quantum dots. Journal of Physical Chemistry Letters 3, 1716–1720 (2012).

26. Griffiths, P. R. & de Haseth, J. A. Fourier Transform Infrared Spectrometry: Second Edition. Fourier Transform Infrared Spectrometry: Second Edition 1–529 (2006) doi:10.1002/047010631X.

27. Lim, I. et al. Fluorous Soluble Cyanine Dyes for Visualizing Perfluorocarbons in Living Systems. J Am Chem Soc 142, 16072–16081 (2020).

28. Sutton, E. J., Henning, T. D., Pichler, B. J., Bremer, C. & Daldrup-Link, H. E. Cell tracking with optical imaging. Eur Radiol 18, 2021–2032 (2008).

29. Day, R. A. & Sletten, E. M. Experimental Perspectives on Direct Visualization of Endosomal Rupture. ChemBioChem 22, 3277–3282 (2021).

Chapter 4: Measuring the Total Photon Economy of Molecular Species through Fluorescent Optical Cycling (FOC)

Preprint with permission from "Anthony V. Sica, Ash Sueh Hua, Belle Coffey, Kierstyn P. Anderson, Ben T. Nguyen, Alexander M. Spokoyny, and Justin R. Caram. Shelving States to Observe Simultaneous Rates with Fluorescent Optical Cycling (FOC)"

The total photon economy of molecule/material is a measure of how light input is converted to light and heat output across energies and timescales. We describe a technique, Fluorescent Optical Cycling (FOC), which allows for simultaneous observation of prompt and delayed emission *during* and *after* multiple pulsed excitations granting access to uncover multi-state photophysical rates. Using controllable duration pulse trains followed by extended (laser-off) wait times we can simultaneously resolve fluorescence, phosphorescence, and singlet oxygen sensitization in a single experiment. Control over the pulse train allows us to "optically shelve" long-lived intermediate states without the use of diode or flashlamp excitation. We use FOC to examine the photophysics of dual emitting bis(di-R-phosphino) alkane thiophene-pyridineplatinum ($[Pt(thpy)(P\hat{}P)]^+$) complex under different solvation conditions. We further couple FOC with Decays Associated Fourier Spectroscopy to achieve simultaneous spectral and lifetime data in this dual emitting complex. Finally, FOC is coupled to superconducting nanowire single photon detectors (SNSPDs) to observe the shortwave infrared phosphorescence of singlet oxygen sensitized by Rose Bengal. Taken together, FOC provides a powerful tool to study emission across energy and time-scales.

4.1 Introduction

The total photon economy of a material represents how energy is partitioned and ultimately dissipated upon an initial excitation event. Resolving the time and frequency of light emission upon excitation provides an indirect method to observe excited state dynamics through standard time-correlated single photon counting (TCSPC). However, excited state processes in materials span many orders of magnitude in time, from femtosecond coherences to seconds of long-delayed emission. Often, the most chemically relevant excited states (e.g., those long-lived enough to participate in diffusion limited chemical reactions), may only populate once after hundreds of excitations, and even then, may only emit photon sparingly. Measuring long-lived emission in a time-resolved fashion requires long and intense illumination (e.g., through a flash lamp or LED) which limits the time resolution of shorter events. Conversely in other methods, such as transient absorption, can resolve simultaneous across timescales, but lack the easy setup, low-intensity and insensitivity to scatter provided by TCSPC.[1]

In this manuscript, we demonstrate a method that allows us to simultaneously study both instantaneous and delayed emissions in a material by using multiple pulsed excitations as an alternative to high power excitation. Building from prior multiple excitation strategies for studying multi-excitons/trap states in quantum dots,[2] phosphorescent dyes,[3] and charging in perovskites,[4,5] we introduce tunable timed-pulse trains while retaining high-time resolution to study the formation and decay of multiple excited states. The resulting pulse trains can span picosecond to millisecond timescales, and then can be turned off for tunable length scales. Our method, which we deem Fluorescent Optical Cycling (or FOC), takes advantage of these tunable pulse trains to build population in long-lived states by 'optically shelving' excitation over multiple pulses. We further

reveal how short-time dynamics and fluorescent intensities are changed upon multiple excitations, providing a complement that describes internal conversion and intersystem crossing.

Typical implementation of time-correlated single photon counting (TCSPC) averages over many pulses to create a fluorescent lifetime trace by histogramming photon arrival times following a pulsed excitation. FOC utilizes the timing of TCSPC to observe multiple decay events over a span of numerous laser pulses. Photoluminescent processes can cover a very wide range of time scales. Fluorescence can be on the order of ns to μs while phosphorescence can span from μs to several seconds.[6,7] We innovate over prior methods through control over the pulse-train, off times, and through resolution of both prompt and delayed emission. Similar methods include periods of turning a continuous wave or burst modes of pulsed lasers. Here, FOC finally looks at fluorescent lifetimes within each pulse of the burst time while simultaneously observing the off time where laser stimulus is halted. To demonstrate the value of the technique, various systems that range from weakly phosphorescent to strongly phosphorescent are studied. FOC was able to probe a variety of systems from film to solution to study phosphorescence induced by heavy atom effects. To also observe the spectral properties of samples, FOC was also paired with a Mach-Zehnder interferometer utilizing the previously established technique of Decay Associated Fourier Spectroscopy (DAFS).[8] With combination of FOC and DAFS, pumping samples can help resolve usually difficult to detect spectral features. Further, FOC was successfully implemented to study emissive events in the visible and shortwave infrared (SWIR) range of emission (SWIR=1000-2000 nm) using superconducting nanowire single photon emitters (SNSPDs). FOC in tandem with the SNSPDs allowed for the direct detection of singlet oxygen via the sensitizer Rose Bengal, a process that often requires flash-lamp excitation due to the relatively low quantum yield of singlet oxygen emission.

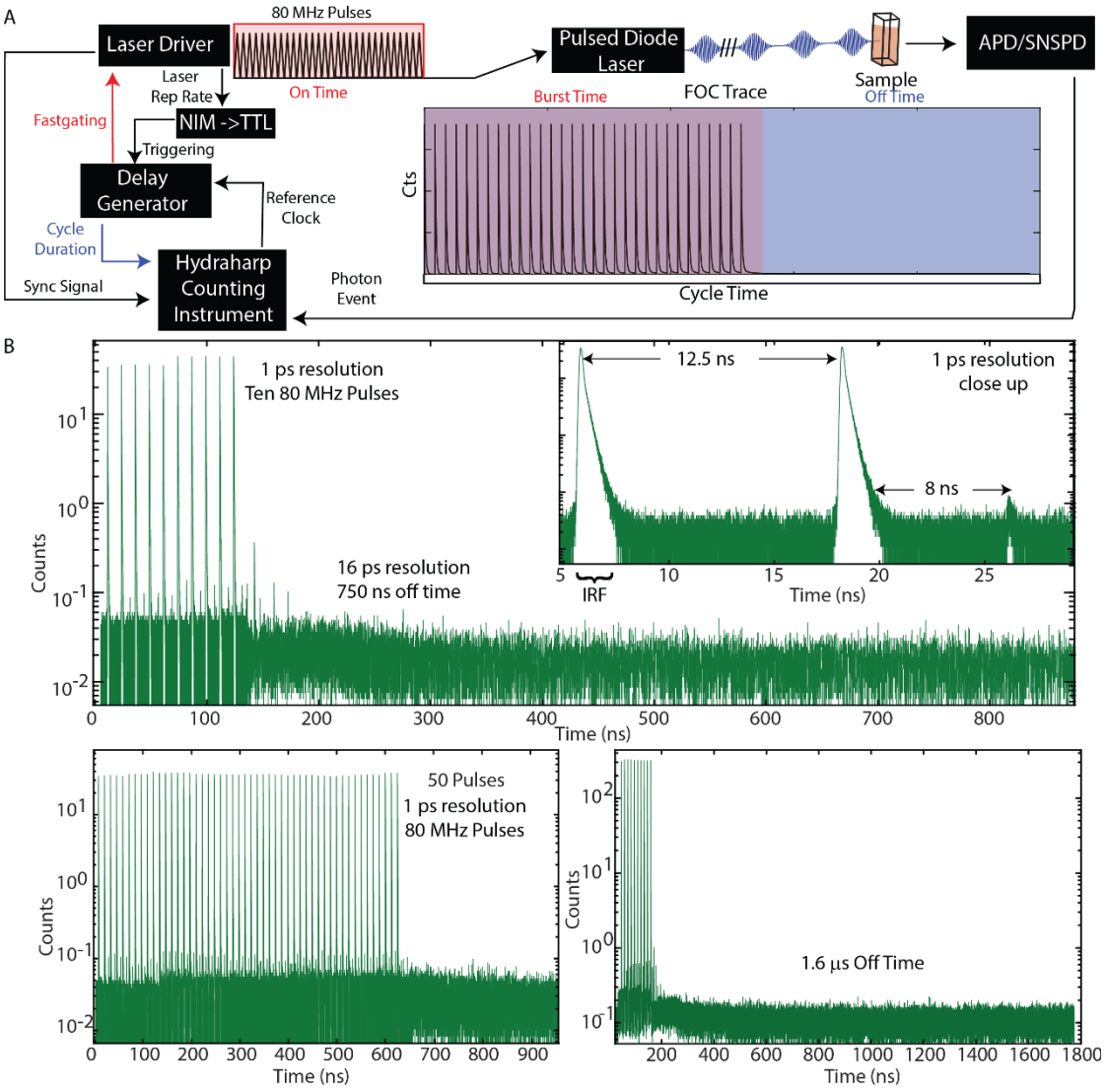

Figure 4.4 Principles and Implementation of FOC

A. General timing scheme used to synchronize on/off times. Briefly, the laser repetition rate is fed into a delay generator that is seeded with a reference clock provided by the photon counting module (Hydraharp, Picoquant). The delay generator provides a fast-gating pulse which controls the number of pulses in a burst. The delay generator signal is also fed into the counting card as a marker. B. Demonstration of tunability of timing in FOC. Here, a laser is used to measure the instrument response function of the system. By adjusting the on/off times the number of pulses and wait times can be tuned with a bin size of 1 ps, and a resolution limited only by the timing and photon collection electronics.

4.2 Generating pulse trains with controllable off times

FOC starts with pulsed laser driver (Picoquant PDL 800D) which is compatible with multiple diodes (LDH-P-FA-530B, or LDH-P-C-405 PicoQuant). The laser driver provides a global synchronization signal using the device's innate crystal repetition rate of 80 MHz. The corresponding sync is fed into the counting card (HydraHarp 400, Picoquant) which where it generates a standard 10 MHz reference clock output; that in turn is used to phase-lock a delay generator (Stanford Research System, INC DG535). The laser driver simultaneously relays a trigger to the delay generator which will then output a signal that can be used to fast gate the laser output. This gating pulse also can be tagged as a marker and used in the analysis of the recorded photon stream. An illustrative depiction of this scheme is found in Figure 1a. In short, the delay generator allows us to control the number of pulses (as fast as a 12.5 ns repetition rate) that are produced prior to the subsequent waiting period or laser off time. In Figure 1b, we show TCSPC of incoming laser scatter to demonstrate how the number of pulses is finely controlled as well as the wait times with a resolution of up limited only by the avalanche photodiode (~30 ps), suggesting little to no jitter between pulse bursts.

4.3 Collecting Lifetimes

Experiments were conducted on a home-built optical microscope. All samples were excited by either a 532 or 405 nm pulsed diode laser (LDH-P-FA-530B, or LDH-P-C-405 PicoQuant, respectively). The emission of the solid-state samples was collected using a 40x air objective (Nikon MRD00405), while the solution emission was collected using a 60x IR water immersion objective (Nikon MRD07650) to insure a tighter focal volume. The emission was sent through our previously reported instrument.[8] The two outputs were either focused onto avalanche photodiodes

(APDs) (PD050-CTD, Micro Photon Devices) for visible detection or super-conducting nanowire single photon detectors (SNSPDs Quantum Opus One). Complete collection of the photon streams was achieved through recording in TTTR (time-tagged time resolved) mode.

4.4 Modeling

In order to understand the results, we employ a kinetic model that is used for fitting and interpretation of the FOC signal. We start with a three-state system to mimic ground state population, singlet excited state fluorescence, and a triplet state which phosphoresces. Included in this model are rates for fluorescence, phosphorescence intersystem crossing, and reverse intersystem crossing. At initial times, a percentage of the population is shelved to the singlet excited state. From there, the kinetics begin using the following differential equations:

$$\frac{\partial S_0}{\partial t} = k_P[T_1] + k_F[S_1] \tag{1}$$

$$\frac{\partial S_1}{\partial t} = k_{BISC}[T_1] - (k_F + k_{ISC})[S_1] \tag{2}$$

$$\frac{\partial T_1}{\partial t} = -(k_P + k_{BISC})[T_1] + k_{ISC}[S_1] \tag{3}$$

The series of differentials can then be described using a matrix:

$$\begin{bmatrix} S_0{}' \\ S_1{}' \\ T_1{}' \end{bmatrix} = \begin{bmatrix} S_{i0} \\ S_{i1} \\ T_{i1} \end{bmatrix} \begin{bmatrix} 0 & k_f & k_p \\ 0 & -(k_F + k_{ISC}) & k_{BISC} \\ 0 & k_{ISC} & -(k_P + k_{BISC}) \end{bmatrix} \tag{4}$$

To exponentiate, we then diagonalize and get the following expressions for each rate:

$$S_0' = \frac{\left\{S_{i1}\,\mathrm{k_F}\left(-1 + \exp\left[\frac{1}{2}At\right]\right)\right\}}{A} + \frac{\left\{T_{i1}\,\mathrm{k}_P\left(-1 + \exp\left[\frac{1}{2}Bt\right]\right)\right\}}{B} \tag{5}$$

$$S_1' = S_{i1}\ \exp\left[\frac{1}{2}At\right] \tag{6}$$

$$T_1' = T_{i1}\ \exp\left[\frac{1}{2}Bt\right] \tag{7}$$

Where B and A are:

$$A = \left\{-(k_{BISC} + k_F + k_{ISC} + k_P)\right. \tag{8}$$

$$\left. - \sqrt{(k_{BISC} + k_F + k_{ISC} + k_P)^2 - 4(k_{BISC} * k_F + k_P(k_F + k_{ISC})}\right\}$$

$$B = \left\{-(k_{BISC} + k_F + k_{ISC} + k_P)\right. \tag{9}$$

$$\left. + \sqrt{(k_{BISC} + k_F + k_{ISC} + k_P)^2 - 4(k_{BISC} * k_F + k_P(k_F + k_{ISC})}\right\}$$

States remaining in each state at the end of a cycle are then used as initial populations in addition to new populations introduced within the next excitation. An example of how each one of these parameters is seen in an FOC trace is described in Figure 2. The adjustment of intersystem crossing from high (Figure 2A) to low demonstrates that the higher ISC populates phosphorescence faster. As a result, each burst peak becomes longer in decay showing a lifting of the bottom of the signal. With intersystem crossing rates remaining constant, a change in phosphorescence rates decreases the overall lifetimes as phosphorescence is shelved in the burst period. Coincidingly, when more molecules can be excited at time (Figure 2C) a faster time to reach a saturation of the rise can be seen. Finally, a depletion event is added to pathways of phosphorescence. This is describe using a ratio of the two states. As depletion rates are increased rates larger percentage of depletion transfer is seen. This causes a downward trend in the burst cycle.

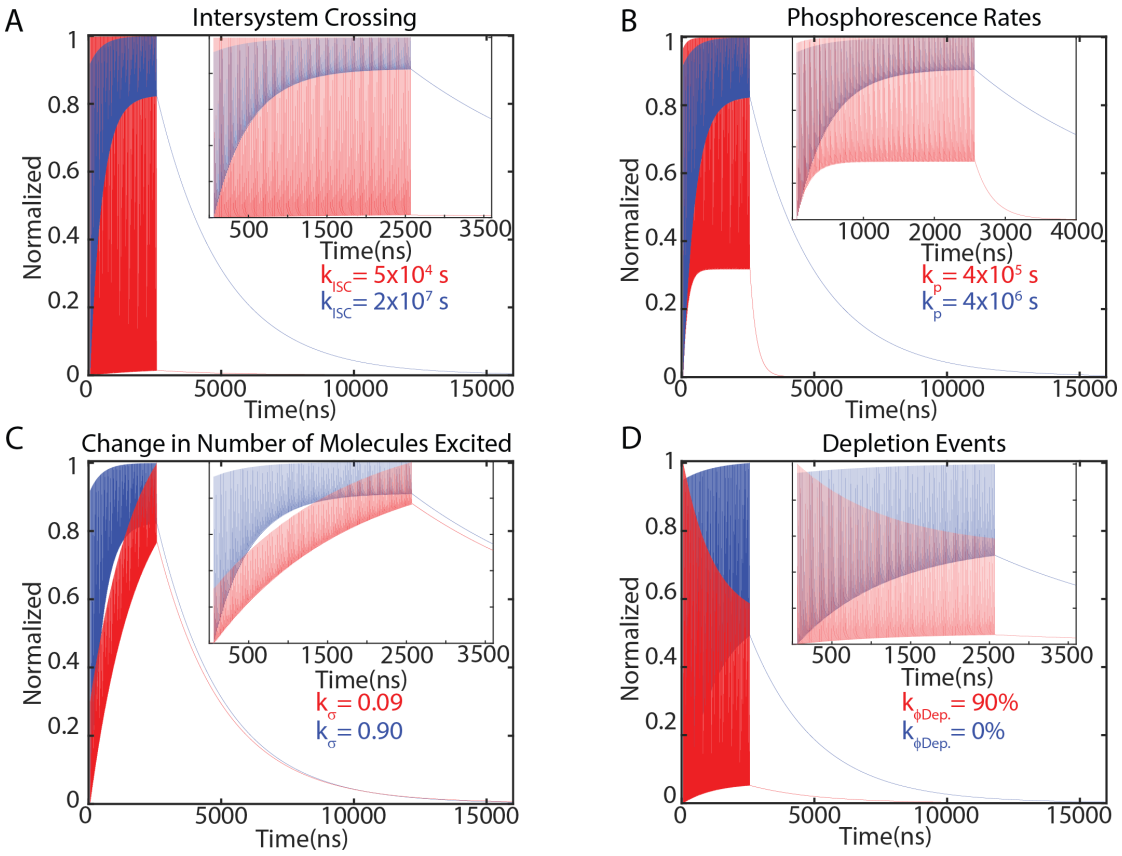

Figure 4.2 Demonstrating Kinetic Modelling Parameters

Demonstrating the effects of adjusting parameters in the kinetic modelling and the resulting FOC trace. A Making the intersystem rate slower causes the increased phosphorescence resulting in the raise in the bottom of the signal. B. With the intersystem rate the same, the phosphorescent rate decrease makes the cycled bursts have a slower overall lifetime. C. Populating the excited state with a higher percentage of molecules leads to a faster saturation than D. Here, a third pathway is added to phosphorescence as a depletion event causing varying percentage of phosphorescent to depletion lifetimes. This results in a downward trend in the burst cycle.

4.5 Dual Emitting Platinum Complexes

To start, we use a sample that exhibits simultaneous fluorescence and phosphorescence. A platinum complex bis(di-R-phosphino) alkane thiophene-pyridineplatinum [Pt(thpy)(P^P)]$^+$ was synthesized using a synthetic procedure established by *Gai, et al.*[9] The Pt complex were cast on a PMMA film by 2 wt% Pt1. The sample was pumped with various laser burst lengths (Figure 3A)

and a trend was observed where the increased in burst length increased the intensity and phosphorescent signal. The signal also reaches saturation point where the increase in signal levels off. FOC continues to also retain the resolution of 64 ps set by the binning the histogram. This way the faster lifetimes as well as the longer-lived states are simultaneously observed. The Pt complex was then mixed in solution with varying ratiometric concentrations of dichloromethane (DCM)

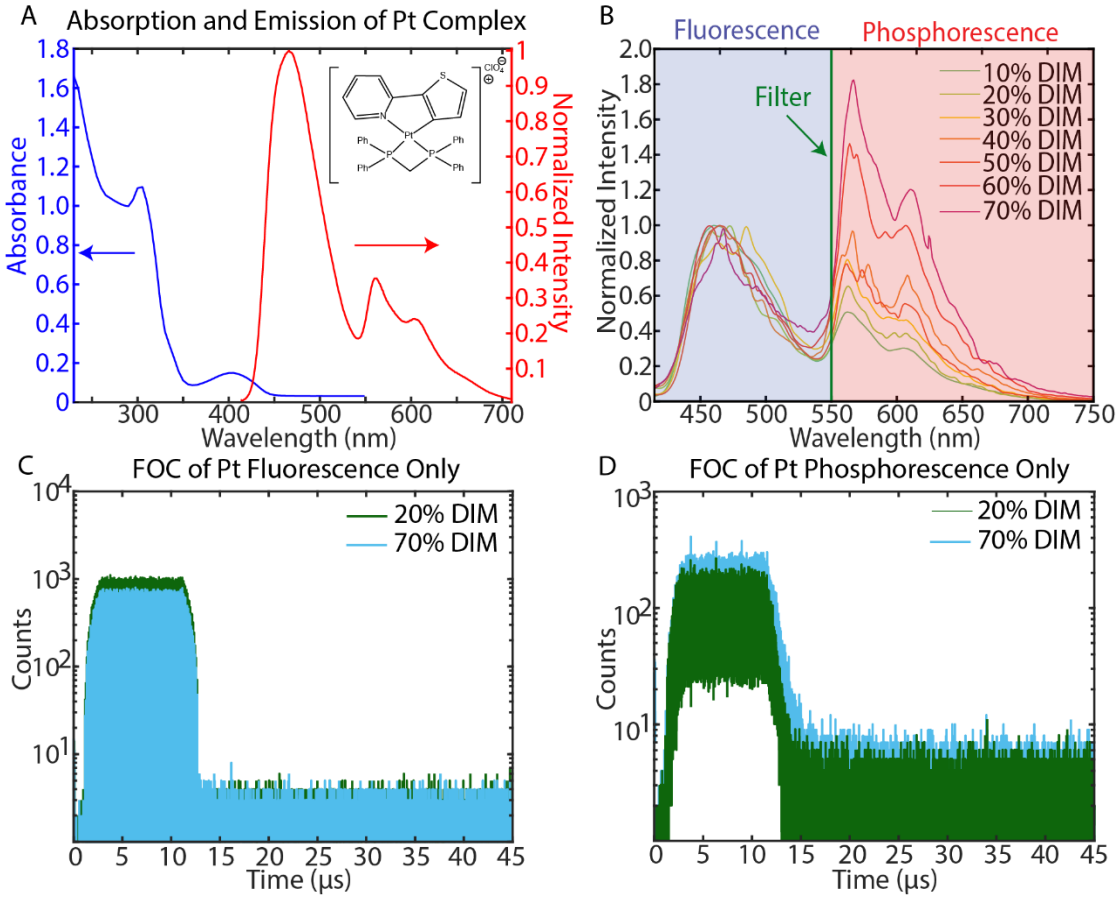

Figure 4.3 Characterization and FOC of Dual-Emitting Pt Complex

Using FOC to pump the dual emitting platinum complex. A. Absorption and Emission of Pt complex in DCM B. The emission spectra of the Pt complex in a mixture of DCM to DIM, as the percentage of DIM increases there is an overall increase in the phosphorescent peak. Emission spectra was normalized to the fluorescent peak at ~460 nm. An FOC of all the DIM: DCM solution samples was taken with a (C) 550 short pass filter and a (D) 550 long pass allowing the measurements of fluorescence and phosphorescence separately. The phosphorescence contains the characteristic rise that has been seen in all previous examples while the fluorescent FOC does not. This confirms the rise in FOC graphs are attributed to this higher order, long lived states like phosphorescence.

and diiodomethane (DIM) to induce a heavy solvent effect and observe dual emission. With an increase in DIM, a clear increase of phosphorescent yield (~550-650 nm) can be seen through the emission spectra (Figure 3B). The emission spectra were normalized to the fluorescent peak (~460 nm) to emphasize this effect. Fluorescence measurements were taken using a commercial fluorimeter (Horiba FluoroMax). Next, the samples were loaded into bulk gaskets and the lifetimes were measured using a microscope. The complexes were excited using a 405 nm laser diode at 10 MHz with a burst time of 10 μs. The measurement was simultaneously taken with one trace isolating the fluorescence by using a 550 short pass (Figure 3C) and the other trace isolating the phosphorescence by using a 550 long pass (Figure 3D). Within the fluorescent only FOC signal the characteristic rise in intensities is not seen, but the phosphorescent only signal results in a rise and decay consistent with slow population of the triplet state. The kinetic model is then used to fit the decays to find all the rates of emission. A sample fit is shown in figure 4A.

In figure 4B, we demonstrate a solvent heavy atom effect in the total and relative quantum yield of phosphorescence fluorescence. We observe generally that as phosphorescence begins to be promoted through the addition of more DIM the phosphorescence lifetimes get longer (Figure 4C) and the intersystem crossing rates get shorter. To explain this trend, we look at the intersystem crossing rates and the subsequent nonradiative pathways. The relative nonradiative rates of fluorescence and phosphorescence were found using the following equations:

$$\phi_f = \frac{k_f}{k_f + k_{nr} + k_{ISC}} \tag{10}$$

$$\phi_p = \frac{k_{ISC}}{k_f + k_{nr} + k_{ISC}} \tag{10}$$

Where ϕ is the relative quantum yields measured in the emission spectra, k_{ISC} is the intersystem found from the modeling, k_f is the fluorescent rate fit from the lifetimes. Addition of DIM results

in an increase in the nonradiative rate for fluorescence and a decrease in nonradiative rate for phosphorescence (Figure 4D). This results in relatively more phosphorescence, but decreased overall emission in the system, as the singlet state can decay nonradiatively. Simultaneously, it is surprising that DIM results in changes in the non-radiative rates of phosphorescence. While there is a relative increase in phosphorescence concurrently a big increase is shown in the nonradiative pathways associated with triplet state decay. As a result, a trend of increased phosphorescence is observed.

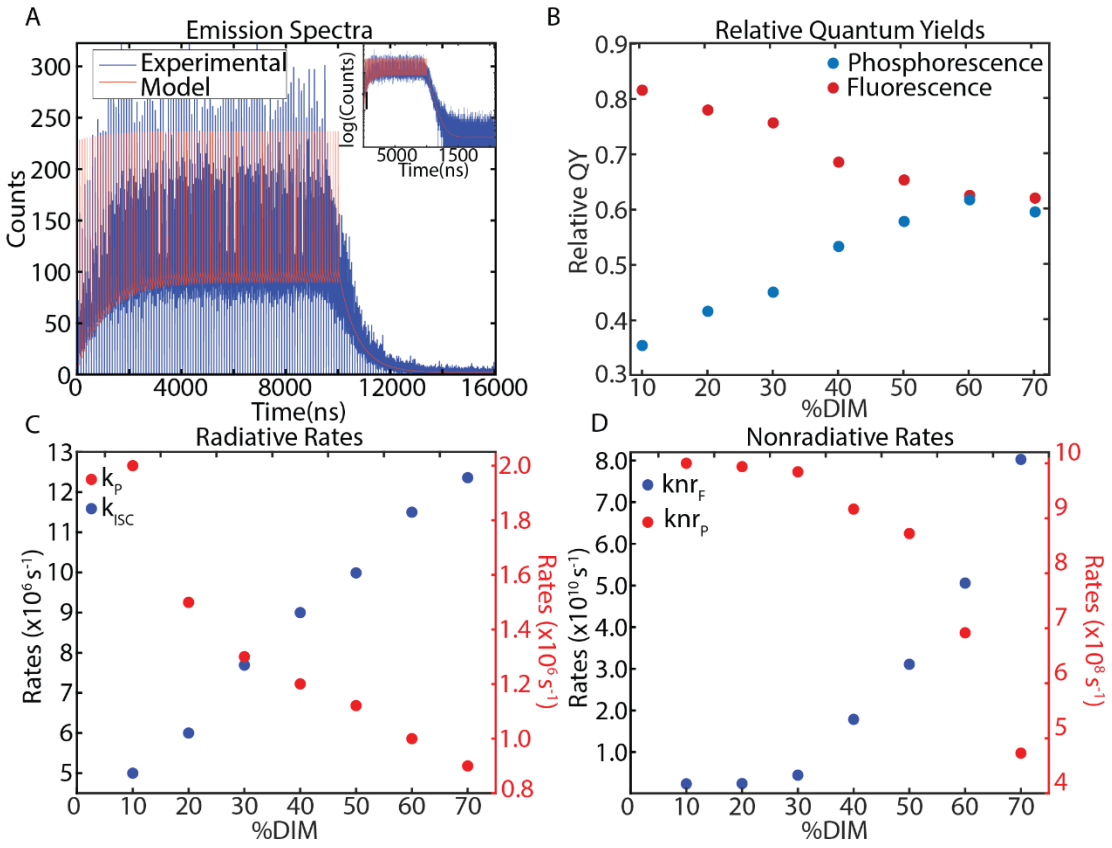

Figure 4.4 Fitting Pt Data with Kinetic Modeling

A. The Pt1 sample with 70% DIM mapped onto the kinetic model confirming the ability to match the model with the experimental data. B. Emission spectra was integrated across fluorescent and phosphorescent peaks to measure relative quantum yields of each emission event. C. Using the model, phosphorescent and intersystem crossing lifetimes were fit. As the phosphorescence of system increases as a function of DIM the subsequent intersystem crossing decreases. D. Using the quantum yields and rates the nonradiative lifetimes can be indirectly measured as well.

4.6 DAFS FOC of Platinum

In prior work,[8] we have used a Mach-Zehnder interferometer to capture emission and lifetime spectra simultaneously. Decay associated Fourier spectroscopy (DAFS) is a wavelength agnostic technique that allows octave spanning across the visible to SWIR region The advantages of DAFS also offers optical mode retention, path-length dependent resolution, and balanced detectors that allows for Fourier filtering of different fluorescent emitters.[10] To summarize, the emission is sent through folded Mach-Zehnder interferometer where one path is allowed vary. The MZ interferometer yields two output beams. DAFS was used in tandem with FOC in order to promote phosphorescence while being able to simultaneously obtain the spectral signatures associated with the lifetimes. DAFS FOC was taken of the Pt1 in PMMA film (Figure 5A). The resulting DAFS displayed the emission of the Pt complex with corresponding lifetimes. The film showed a clear separation of the fluorescent and phosphorescent emissions. Longer-lived lifetimes were observed when integrating phosphorescence. However, when fluorescence was integrated this long-lived decay was less prominent.

4.7 FOC of Direct Detection of Singlet Oxygen

Ground state triplet oxygen can be sensitized to a higher lying singlet state through interaction with a dye molecule that can undergo triplet energy transfer. There are two singlet states, termed $^1\Sigma^+_g$ (corresponding to two paired electrons in different orbitals) and the more stable, lower energy $^1\Delta_g$ (corresponding to two paired electrons in the same orbital). Singlet oxygen plays a paramount role in an array of biological functions such as signaling for cell death and oxidative stress,[11] bioenergetics,[12] cancer mechanisms,[13] and many others.[14–16] Outside of the natural systems, singlet oxygen is also used for treatments such as photodynamic therapy, where undesired tissue

is damaged through photooxidative processes.[17] One method to probe singlet oxygen is through its phosphorescent emission from the $^1\Delta_g$ state at 1275 nm, in the short-wave infrared (SWIR). Superconducting nanowire single-photon detectors (SNSPDs) have been used previously to detect singlet oxygen, we utilize them with FOC to enhance and study the singlet oxygen emission through burst excitation.

Rose Bengal, as a sensitizer for FOC, was purposely used to detect the singlet oxygen generation at ~1275 nm. A sample of Rose Bengal flowed through a gasket at a medium flow rate. Flowing the sample helped regenerate unexcited sample and collect emission of singlet oxygen at higher yields and less time. The sample's emission was detected using SNSPDs (Quantum Opus) whose quantum efficiencies reach ~85% at the region of interest. Before collection, a 533 nm notch filter and 550 nm LP were used to filter out the majority of the fluorescence. The sample was collected using a 532 nm laser at 80 MHz with a hold time of ~15 μs and an off-time of 60 μs. The sample FOC collected is seen in Figure 5B. In this FOC, we see a gradual decrease in the signal during bust mode, which is emphasized in linear plot shown as an inset. This is modeled as seen above as a depletion event. The depletion in signal here is attested to the energy transfer process between the Rose Bengal and triplet state oxygen necessary to form singlet oxygen. Because of this, the kinetic model is adjusted to include this additional transfer pathway. When using a more applicable kinetic model this decay is a product of less phosphorescent yield and slower energy transfer rates. This contributes to the signal being dominated by shorter lifetimes components and more yield in nonradiative pathways. The FOC burst times begins to resemble the fluorescence depletion seen in our example model (Figure 1B). When fitting the tail, the lifetimes is found to be 3.39 μs. This is like ultrafast studies at room temperature which found the lifetime of singlet oxygen to be 3.5 μs.[18,19]

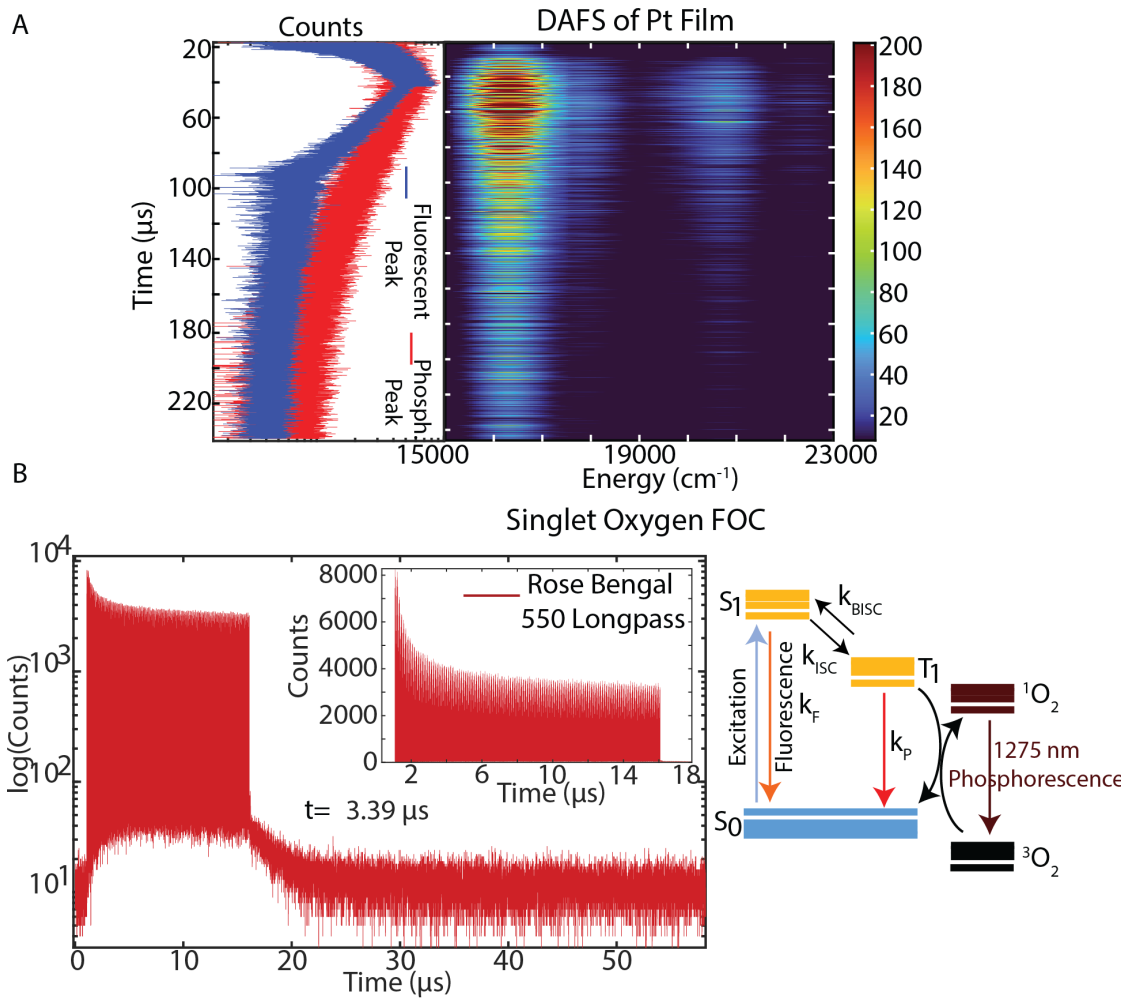

Figure 4.5 DAFS FOC of Pt and FOC of Singlet Oxygen

A. DAFS of Pt PMMA film. There is a clear separation of a shorter lifetime seen at the fluorescent peak while a longer lifetime is observed when integrating along the redder phosphorescent region. B. FOC of Rose Bengal using a 550 LP filter. Lifetimes were collected through SNSPDs to directly observe the phosphorescence of singlet oxygen at 1275 nm. The sample was continuously flowed to freely diffuse Rose Bengal. To the right is, the Jablonski diagram of singlet oxygen showing the pathway of Rose Bengal fluorescence and energy transfer to the triplet oxygen to form singlet oxygen.

4.8 Discussion

We have successfully demonstrated the utility of FOC to simultaneously capture long-lived photophysical events and faster dynamics. This is done while maintaining proper resolution to be

able to observe both states. Along with this, the breadth of this technique to pump and observe systems from highly phosphorescent to weakly phosphorescence such as the singlet oxygen photoluminescence is successfully demonstrated. There has been similar pumping technique as a method to probe oxygen in live cells while simultaneously imaging in reference to the study of phosphorescent lifetime imaging microscopy (PLIM).[20] However, we demonstrate the ability to directly detect singlet oxygen's emission and lifetimes with the use of SNSPDs. The ability to measure fluorescent lifetime imaging (FLIM) as well as PLIM in tandem opens an interesting avenue to view the dynamics of short-lived fluorescent probes and their interaction with longer emission events.

References

1. Penzkofer, A., Beidoun, A. & Daiber, M. Intersystem-crossing and excited-state absorption in eosin Y solutions determined by picosecond double pulse transient absorption measurements. *J Lumin* **51**, 297–314 (1992).

2. Singh, G., Guericke, M. A., Song, Q. & Jones, M. A multipulse time-resolved fluorescence method for probing second-order recombination dynamics in colloidal quantum dots. *Journal of Physical Chemistry C* **118**, 14692–14702 (2014).

3. Shcheslavskiy, V. I., Neubauer, A., Bukowiecki, R., Dinter, F. & Becker, W. Combined fluorescence and phosphorescence lifetime imaging. *Appl Phys Lett* **108**, 091111 (2016).

4. Saba, M. *et al.* Light-induced charged and trap states in colloidal nanocrystals detected by variable pulse rate photoluminescence spectroscopy. *ACS Nano* **7**, 229–238 (2013).

5. Wieghold, S. & Nienhaus, L. Precharging Photon Upconversion: Interfacial Interactions in Solution-Processed Perovskite Upconversion Devices. *Journal of Physical Chemistry Letters* **11**, 601–607 (2020).

6. Introduction to Fluorescence. *Principles of Fluorescence Spectroscopy* 1–26 (2006) doi:10.1007/978-0-387-46312-4_1.

7. Fluorescence Microscopy - Basic Concepts in Fluorescence | Olympus LS. https://www.olympus-lifescience.com/en/microscope-resource/primer/techniques/fluorescence/fluorescenceintro/.

8. Atallah, T. L. *et al.* Decay-Associated Fourier Spectroscopy: Visible to Shortwave Infrared Time-Resolved Photoluminescence Spectra. *J Phys Chem A* **123**, 6792–6798 (2019).

9. Li, K. *et al.* Excitation-Wavelength-Dependent and Auxiliary-Ligand-Tuned Intersystem-Crossing Efficiency in Cyclometalated Platinum(II) Complexes: Spectroscopic and Theoretical Studies. *Inorg Chem* **59**, 14654–14665 (2020).

10. Sica, A. v, Atallah, T. L. & Caram, J. R. Spectrally-selective Time-resolved Emission through Fourier-filtering (STEF). (2021) doi:10.26434/CHEMRXIV-2021-G7HMW.

11. Laloi, C. & Havaux, M. Key players of singlet oxygen-induced cell death in plants. *Front Plant Sci* **6**, 39 (2015).

12. Sokolovski, S. G., Rafailov, E. U., Abramov, A. Y. & Angelova, P. R. Singlet oxygen stimulates mitochondrial bioenergetics in brain cells. *Free Radic Biol Med* **163**, 306–313 (2021).

13. Baier, J., Maisch, T., Maier, M., Landthaler, M. & Bäumler, W. Direct detection of singlet oxygen generated by UVA irradiation in human cells and skin. *J Invest Dermatol* **127**, 1498–1506 (2007).

14. Flors, C. & Nonell, S. Light and singlet oxygen in plant defense against pathogens: Phototoxic phenalenone phytoalexins. *Acc Chem Res* **39**, 293–300 (2006).

15. Reddi, E. *et al.* Photophysical Properties and Antibacterial Activity of Meso-substituted Cationic Porphyrins¶. *Photochem Photobiol* **75**, 462–470 (2002).

16. Kammerlander, G. *et al.* A clinical evaluation of the efficacy and safety of singlet oxygen in cleansing and disinfecting stagnating wounds. *J Wound Care* **20**, 149–158 (2011).

17. Dolmans, D. E. J. G. J., Fukumura, D. & Jain, R. K. Photodynamic therapy for cancer. *Nature Reviews Cancer 2003 3:5* **3**, 380–387 (2003).

18. Bregnhøj, M., Westberg, M., Minaev, B. F. & Ogilby, P. R. Singlet Oxygen Photophysics in Liquid Solvents: Converging on a Unified Picture. *Acc Chem Res* **50**, 1920–1927 (2017).

19. Wilkinson, F., Helman, W. P. & Ross, A. B. Quantum Yields for the Photosensitized Formation of the Lowest Electronically Excited Singlet State of Molecular Oxygen in Solution. *J Phys Chem Ref Data* **22**, 113–262 (1993).

20. Mizukami, K. *et al.* In vivo O2 imaging in hepatic tissues by phosphorescence lifetime imaging microscopy using Ir(III) complexes as intracellular probes. *Scientific Reports 2020 10:1* **10**, 1–14 (2020).

Chapter 5: Future Work and Perspectives

This chapter discusses preliminary research directions and short progress reports. In the prior chapters, interferometry and balanced detection was utilized to separate temporal and spectral information by manipulating the photon stream. The following chapter elaborates future perspectives. To start, a dip probe method was used for collecting photoluminescence lifetimes. Dip probe-based spectroscopy allows us to explore reaction dynamics which affect chromophore lifetimes within a reaction vessel. I will show preliminary work to measure the reaction time of aggregation and the resulting lifetime changes due to suppression of nonradiative traps and emergence of superradiance. In addition, a progress report towards implementing fluorescent lifetime imaging microscopy (FLIM) in the SWIR will be presented with a few examples of visible FLIM implemented with stage scanning. Finally, the first instance of correlative light with electron microscopy (CLEM) is demonstrated with the use of nanoplatelets.

Following this, future suggestions of projects and improvements on interferometry will be explored. One such project uses correlation methods to study effects such as single photon emitters and diffusion in a sample. Furthermore, the prospects of pushing correlation in tandem with interferometry will be discussed. Photon Correlation Fourier Spectroscopy (PCFS) uses interferometry to measure relative spectral features of highly correlated events and could be implemented to study multi-excitonic features such as biexcitons. With this, I will also introduce the use of fiber optic stretchers with the intention of building simple in-fiber interferometers to measure higher order correlations in the system. Finally, perspectives of wild-field interferometry will be discussed for hyperspectral imaging. Typically measured with EmCCD cameras, an array of APDs may offer the ability to collect high-resolution temporal information

with the emitted photon stream. This opens avenues to implement high-throughput measurements. Within each pixel, a sub-ensemble of photons can be manipulated to collect wide-field FLIM, FOC, DAFS, correlation measurements, and super-resolution microscopy.

5.1 Dip Probe

Most experiments that study the emitted photon stream focus on bulk solution or single molecules fixed to a surface. There are few fluorescent measurements that examine the sample in varying environments such as high-temperature Schlenk lines synthetic apparatus or air-free glove boxes. Here we implement a dip probe to excite and collect fluorescence lifetimes signals to observe reaction kinetics in real time. Dip probes have been previously utilized to measure reaction kinetics via absorption and emission collection.[1–4] The dip probe utilizes a bundle of

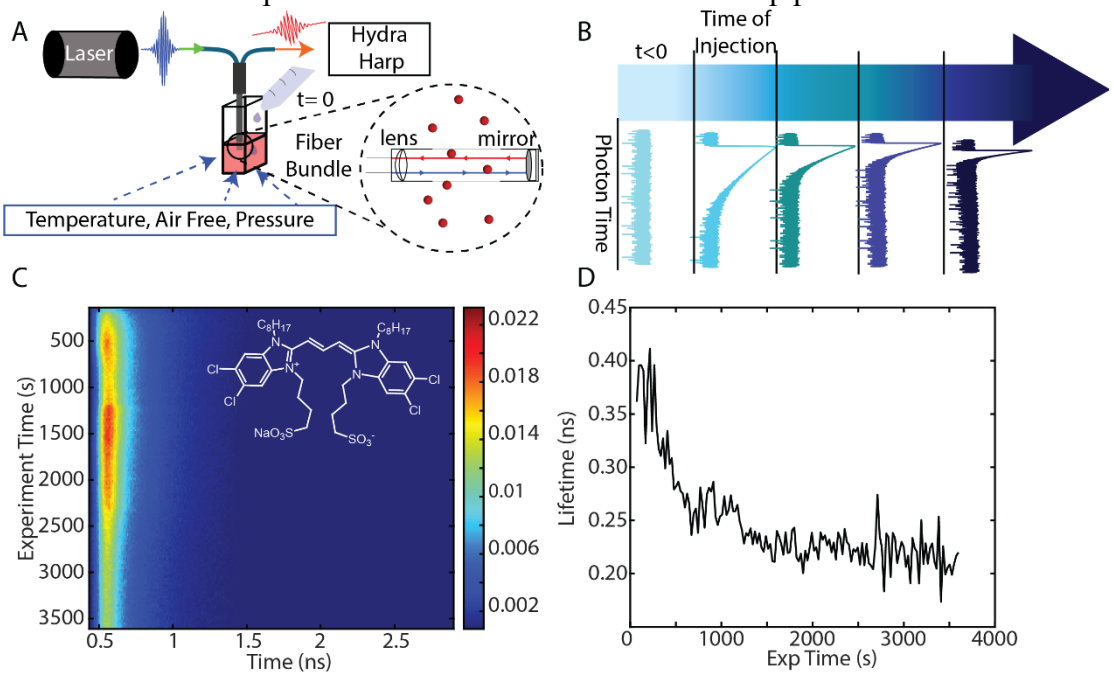

Figure 5.1 Lifetime in situ photoluminescence

A. Schematic of the dip probe where laser excitation is applied directly into sample under sub-optimal conditions such as temperature, pressure, and air free. B. The reaction starts and the TCSPC collects change in lifetimes as the experiment proceeds. C. Dip probe measurement of water being added to a MeOH solution of C3S8 to observe aggregation through change of lifetimes. D. Each slice is fitted to lifetimes and a decrease a lifetime is seen as a product of aggregation.

optical fibers that transmit light through a metal tip with a small path length of collimated light. Using attenuated reflection, an increased signal is recovered, and fluorescence is then collected back into the fiber bundle where the emission can be observed with single photon detectors. With these principles, the dip probe is implemented to collect lifetimes as a reaction proceeds. Dip probe offers the advantage of having a semi-portable cuvette in a tip that can be used in environments typically difficult to study. An example being processes that occur in sub-optimal environments such as measuring reactions in high temperature Shlenk lines or air-free methods within a glovebox. In a preliminary demonstration of dip probe (Figure 5.1C-D), we inject water into a methanol solution of C8S3. As water is added, the molecular dye will begin to aggregate, and the lifetime dynamics of aggregation can be observed in real time. This is demonstrated by fitting lifetimes across experimental time increments. As a result, a decrease in lifetimes is observed as the reaction proceeds (Figure 5.1D), indicative of exciton superradiance.

5.2 Temperature Dependent Excitonic Studies of Proteins

Using synthetic routes for protein construction is a rapidly growing area.[5] Fine tuning proteins offers a means for studying structure-function of protein dynamics but has not been extensively applied to pigment-proteins. We have collaborated with Prof. David Baker whose lab has designed a de novo C_2-symmetric protein that binds cholorophyll. This synthesized protein offers a way to explore the photophysical dynamics demonstrated by strongly coupled chromophores within the protein (Figure 5.2A). The protein, SP2, positions chlorophyll dimers uniformly. In order to understand this excitonic coupling we contribute perspective on the photophysical changes as a function of temperature (Figure 5.2B-C). We utilize a cryostat with temperature controller to module the temperature from 75K to room temperature and study photophysics through absorbance, emission, and lifetime measurements. Within the studies we observe various

line shape changes in the emission spectra as well as lifetime dependence in temperature that indicate the emergence of strong coupling among chlorophyll molecules in this designed protein environment. An in-depth interpretation may be found in the subsequent paper (Preprint: Ennis, M Nathan, *et al.* "De novo design of energy transfer proteins housing excitonically coupled chlorophyll special pairs" https://doi.org/10.21203/rs.3.rs-2736786/v1).[6]

Methods

A sugar matrix was utilized to retain state and study the sample. A 50:50 sucrose/trehalose (w/w) dissolved in distilled water was added to solutions of SP2-ZnPPaM.[7] A 100 μL sample sugar solution was used as SP2 at 34 mg/mL (ZnPPaM dimer) was added dropwise followed by gentle mixing. This mixture was then dropped into a Starna Cell 0.1 mm quartz cuvette. Overnight, the sugar matrix was kept under vacuum. We then used a Janis ST-100 cryostat to load the sample. Using a custom-built copper cuvette holder, the system was cooled with liquid nitrogen, and a Lakeshore 330 Autotuning Temperature Controller was used to control the temperature. For emissions, the samples were excited with a 405 nm cw laser diode. The lifetime samples were excited via a pulsed laser output from a 405 nm pulsed diode laser (LDH-P-C-405, PicoQuant) with a 10 MHz repetition rate.

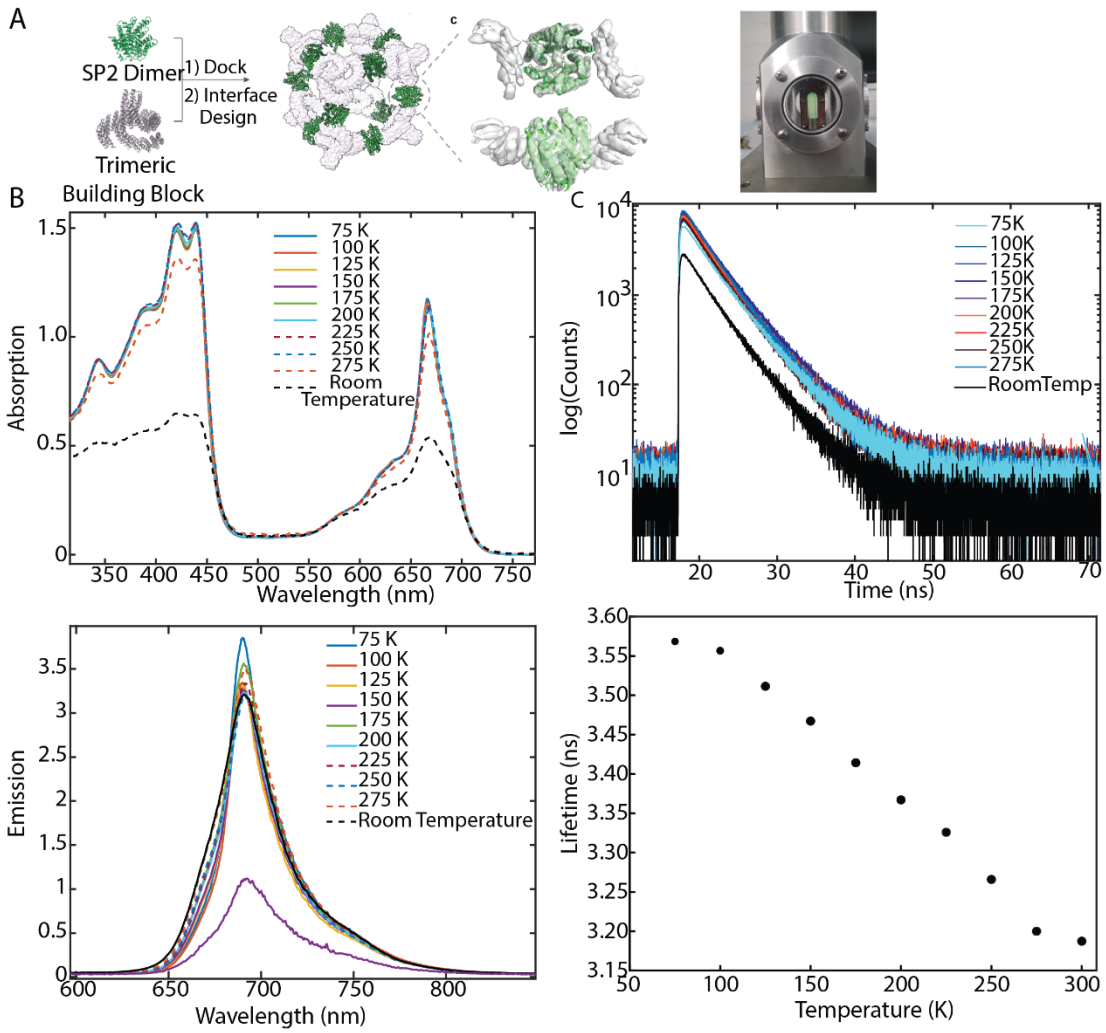

Figure 5.2 Temperature Studies of Excitonic in Synthetic Proteins

A. (left) A SP2 ZnPPaM dimer synthetically designed to have C_2 symmetry to understand Ch1-Ch1 coupling and excitonic characteristics of the protein. (right) Cryostat setup in which SP2 was integrated into a sugar matrix and used to take measurements. B. Absorption (top) and emission (bottom) spectra as a function of temperature. C. TCSPC traces (top) as a function of temperature and their corresponding lifetime fits (bottom) with an increase of temperature leading to slower lifetimes.

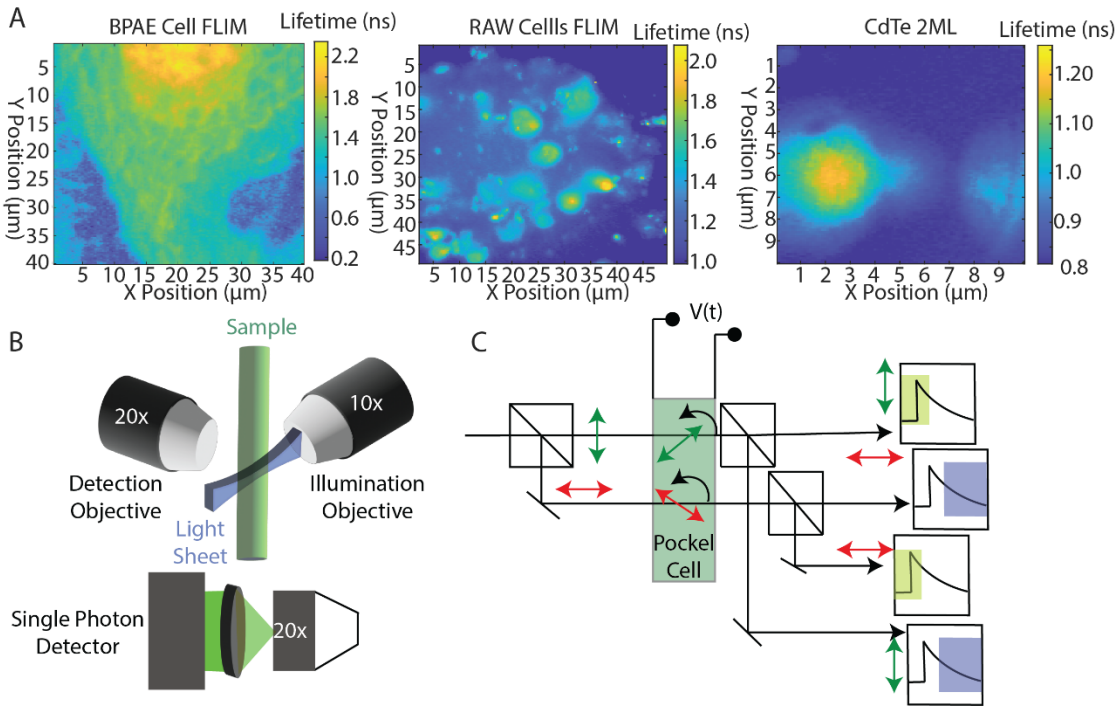

Figure 5.3 Fluorescent Lifetime Measurements

A. Sample FLIMs taken thus far with (left) BPAE cells, (middle) RAW 264.7 cells, and (right) 2ML CdTe nanoplatelets. B. Scheme for a possible wide-field implementation of FLIM. In this example, a light sheet is taken and then collected through a separate objective which subsequently projected onto a single photon array.[9] C. An electro-optical FLIM set up that separates polarization through the use of a Pockel cell. This can then project the first and second half of the lifetime on a camera, allowing for wide field FLIM.[10]

5.3 Fluorescent Lifetime Imaging

Fluorescent probes can be used to label specific targets of interest and localize them in a broader context. Typically, images are collected using a microscope that collects the intensity of emission events. Images collected through this means only describe the spatial features of a system but lack photophysical information about the system. Fluorescent lifetime imaging microscopy (FLIM) resolves this issue by collecting lifetimes pixel to pixel and associates photophysical events with spatial features. Collection of images with encoded lifetimes allows us to study energetic interactions such as FRET that cannot be differentiated otherwise.[8] Here, I demonstrate the successful construction of a FLIM microscope. Using a confocal microscope,

lifetime traces can be measured as a translational system scans spatially. Originally, a piezo stage was implemented. However, such scans were slow, resulting in the need for a fast-scanning dual axis galvos system to speed up the speed of scans. As a result, the time of scan becomes only limited by the fluence of photons needed to resolve a lifetime. Using the microscope, FLIM is implemented with example systems (Figure 5.3) emitting in the visible region. Eventually we hope to move towards an area that is less explored by doing FLIM in the SWIR. Because the photon stream is collected when measuring FLIM, simultaneous measurements such scanning correlation measurements are easily obtainable. To improve the throughput of FLIM, it may be advantageous to explore wide-field FLIM. Wide field imaging offers collection of z-axis slices instead of performing lengthy point scans. There are such examples that use light sheet microscopy which will collect layers of images at a time.[9] Another example is the use of electric modulation to increase throughput where the light is divided into two directions and imaged on a camera.[10] While one loses half the field of view on the camera it can dramatically increase the speed at which lifetimes are collected. Normally these could be collected on a CCD or cMOS camera, however, there are additional avenues to achieve the temporal resolution necessary such as the use of a SPAD array.[11,12] In addition, it is also possible to leverage the interferometer for ratiometric imaging using balanced detection or STEF.[13]

5.4 Correlative Super-Resolution Light and Electron Microscopy (CLEM)

While fluorescence allows for the study of sample photophysics and localizes regions of interest, the resolution of images collected are limited by the diffraction of light. This makes it very difficult to measure images at sub-nm scales and interpret finely resolved structures. Correlative light and electron microscopy (CLEM) is a toolset that combines the two and allows for the localization and energetic information akin to fluorescence while simultaneously being able to

gather structural information offered by electron microscopy. We demonstrated our first use of CLEM by studying 3 ML CdTe nanoplatelets. The photoluminescence of the nanoplatelets is successfully overlayed with electron microscope images (Figure 5.4).[14] With this, things such as spatial inhomogeneities and other structural features are observed. Overlaying these images while also collecting single molecule lifetimes or correlations can further elucidate how the morphology of nanoplatelets such as layer number and size of nanoplatelets influence the sample's photophysics. However, the use can be somewhat limited without the means to also study such materials at cryogenic temperatures. With cryogenic microscope sample holders becoming widely utilized it should be something to consider in the future.

5.5 Super Resolution Microscopy

With CLEM potentially on the horizon it would be useful to increase the resolution in the optical microscopes we use. There are already such implementations that can exceed the diffraction limit of light. An example of this is stochastic optical reconstruction microscopy (STORM).[15] Samples with blinking emission signals are slowly collected through time and an image is formed through point-spread function (PSF) localization. STORM is a relatively straight forward optical setup where the difficulty lies in the analysis. Other such methods that are not as straightforward utilize patterns of illumination, structured illumination microscopy (SIM),[16] and stimulation/depletion events using stimulated emission depletion (STED).[17] While these are more complex to optically achieve, the toolsets still exist in our lab space.

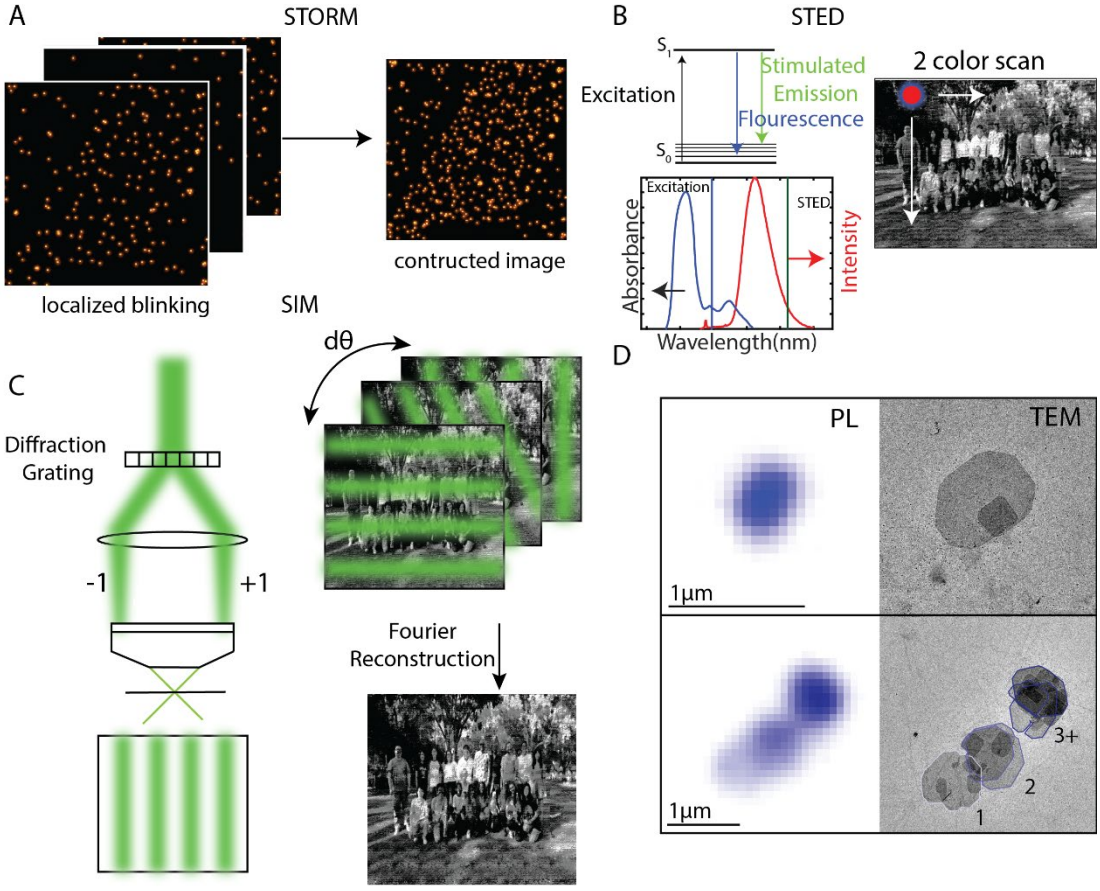

Figure 5.4 Correlative Super-Resolution Light and Electron Microscopy (CLEM)

A. Example STORM data analysis. Blinking of emitters are leveraged to collect a complete image as time goes on. The complete image is then assembled using PSF analysis.[15,36] B. STED utilizes a continuous excitation which is then depleted through a second laser via stimulated emission.[17] This is a scanning confocal method so it tends to be slower and since it is stimulated emission driven it can also use high laser power. C. Diffraction gratings are used in SIM to create array or patterns of illumination. The illumination is then rotated through space. The image is then reconstructed through Fourier reconstruction.[16] D. An example of CLEM used in our experiments. 3ML nanoplatelets photoluminescence is overlayed with TEM images of the same platelets.[14]

5.6 Improvements in Current Interferometry

Photon Correlation Fourier Spectroscopy (PCFS).

As demonstrated, a robust interferometric system has been implemented using Mach-Zehnder interferometry and single photon detectors. Because of our interest in single molecule studies, the next lucrative trajectory is in fluorescence correlation studies. Correlations, specifically second order, can be described as follows:

$$g^{(2)}(\tau) = \frac{\langle I(t)I(t+\tau)\rangle}{\langle I(t)\rangle\langle I(t+\tau)\rangle} \tag{5.1}$$

Where $g^{(2)}(\tau)$ is the second-order correlation function, $I(t)$ is the intensity, and τ is a time lag. Correlation spectroscopy correlates fluorescence intensity fluctuations to interpret physical events in a system. These fluctuations can be used to observe diffusion constants,[18] hydrodynamic radii,[19] concentrations,[20] chemical kinetics,[21] and singlet-triplet dynamics.[22,23] When considering emitters in the quantum regime, a careful analysis of the photon stream must be implemented. The collected signal must be considered as single photons in vs number of photons out of the system.[24] We can start our description by taking $\boldsymbol{\tau \rightarrow 0}$ which treats our expression as:

$$\lim_{\tau \to 0} g^{(2)}(\tau) = \frac{\langle I(t)^2\rangle}{\langle I(t)\rangle^2} = C \tag{5.2}$$

Where C describes the anti-bunching of the photon stream. Anti-bunching describes single photon events as a result of a single laser pulse stimulus i.e. if I put in one photon do I get only one out. When two photons are detected simultaneously from a single emitter C approaches 0.5.[25–28]

When a multi photon event occurs the correlation function can reveal information about the emitters photophysics such as the existence of excitonic dynamics that form excitons, biexcitons, or trions.[29] In other words, with the use of correlations measured the existence of higher-order recombination dynamics and likelihood of these events can be determined. However, correlations only allude to the existence of these events while revealing no information to the energetics within the system. To fix this, interferometry can be implemented to gain a spectral

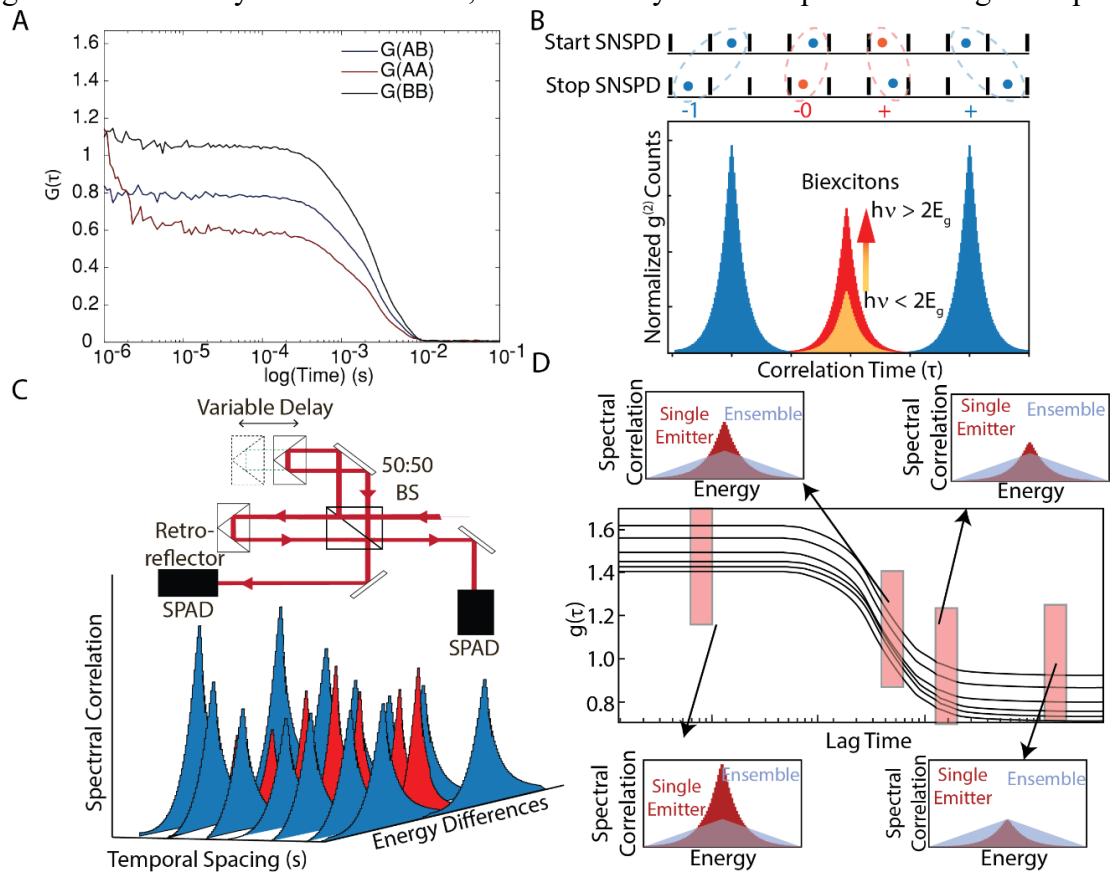

Figure 5.5 Photon Correlations

A. Sample solution FCS taken using a water objective and a solution of flowed Rhodamine 6G. B. Simulated anti-bunching photon correlations. The rise in the center peak represents multi photon events from one photon in indicating biexciton features. C. Sample PCFS setup, as the interferometer scans through space the correlations that are taken also have spectral information correlated with them. D. Solution PCFS where the log correlation function is taken as path delay changes. Different time scales of the FCS can show us single molecules in and out of the focal volume represented by the correlation peak higher in shorter times while matching ensemble in longer times. Figure C-D adapted[37]

perspective on the processes using photon correlation Fourier spectroscopy (PCFS).[30] PCFS leverages interferometry to resolve relative spectral information of a correlated pair of photons. PCFS, however, does not reveal absolute energies, and only begins to quantify the relative energetics of the incoming excitonic features. This has been used in a range of single molecule applications and has also been implemented in solutions.[31] We hope to implement both techniques to study SWIR emitting materials on a single molecule scale and begin studying higher order correlations. The efforts have already begun instrumentally as DAFS has been adjusted to support PCFS measurements.

Heterodyne Detection

Another improvement in the interferometer is to optimize the precision that the instrument can achieve in the observed energetics. The use of heterodyne detection can introduce a known wavelength as an internal standard. Heterodyne detection uses a local oscillator of known frequency as a point of reference in comparison to the emission of unknown frequency and line shape.[32] This will be implemented in the DAFS setup by overlaying a laser with short linewidths resulting in a long coherence length that can span the entire length of the stage. For this reason, a long coherence length HeNe laser is a practical candidate. The two-detection scheme could also be used as one detector can correspond to the HeNe and the other to the sample making the use of heterodyne higher throughput. The use of heterodyne can resolve signals of larger coherence lengths with and be used as a spectral signature for emission spectra.

Fiber Based Interferometry

The scheme of interferometry used above is set up with extremely high stability. Because of this, however, the optical setup takes up a lot of space and requires more materials. Within the horizon, we hope to install multiple arrays of beam splitters to obtain higher order correlations. It has been shown that correlations above $g^{(2)}$ correlation can begin to elucidate higher order photophysical pathways in Auger processes.[23] Energetics and correlations must be facilitated through compact series of beam splitters/interferometers. To optimize this, we propose the use of various length fibers to act as interferometers. Winding two bundles of single mode optical fibers around drums will act as path lengths. As we stretch one drum the path length on one side is

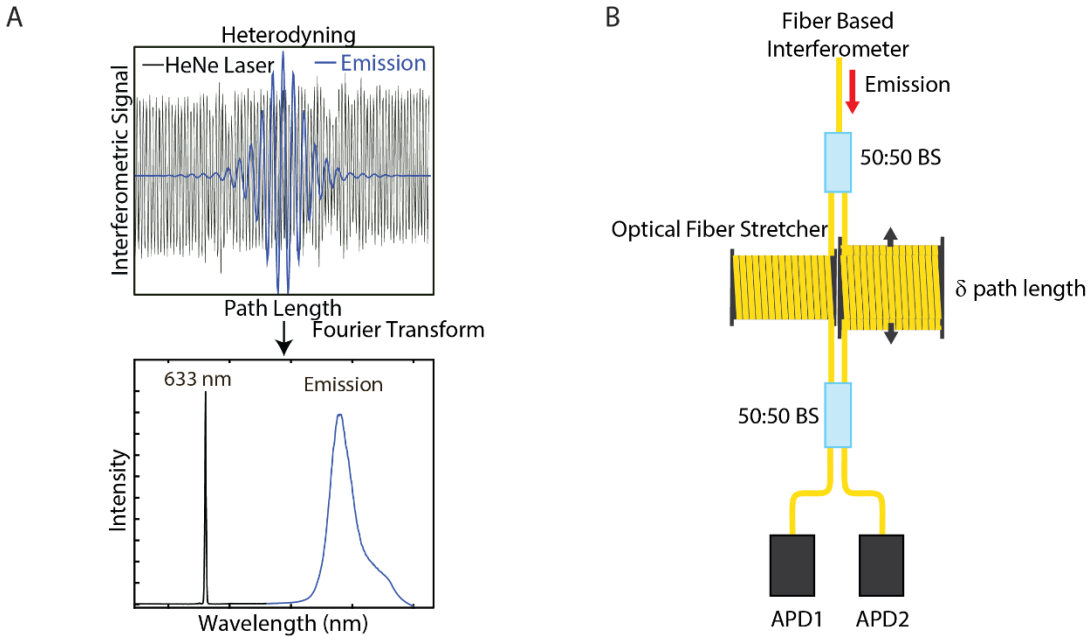

Figure 5.6 Interferometry Perspectives

A. Example of heterodyning where a HeNe interference is plotted with an emission. When Fourier transforming the emission peak signature can use the 633 nm HeNe as a reference. B Single mode fiber-based interferometry in which emission is split between two fiber pathways of similar length. Both are wound around drums with one path, however, being wrapped around a drum that can stretch in diameter. This stretch creates a path length difference allowing for interferometry.

modulated allowing for the scanning of interferences. There are a few things to consider with the largest being wavelength dependent dispersions. This will result in larger phase chirps in the signal. To amend this, the Mertz correction already implemented in DAFS will need to be fine-tuned and the interferometer calibrated with heterodyne detection in a rigorous way. The use of drum fibers will free up space and allow easier direct connection to fiber coupled APDs making parallel beam splitters an easier and compact design.

5.7 Wide-Field Interferometry

Interferometry has helped in studying and collecting many physical aspects in the system simultaneously. An advantageous route would be to begin extending this with imaging to retain spatial information of samples. However, it can be cumbersome measuring interferometry and imaging samples simultaneously with high throughput. Here I offer already established avenues that I think should promote more efficient sample collection and reduce the lengthy experiment times. All the following schemes considered below will enable us to collect wide-field interferometric images on a 2D array of single photon detectors. This allows the total photon economy to be collected spatially as well. With this, a single image can be hyperspectral while allowing for any combination of techniques described above.

Light Sheet Interferometry

Light sheet microscopy is a newer method that uses sheet-like illumination to quickly recover volumetric slices of a sample.[33] As demonstrated, wide-field interferometry can be implemented using light sheet instead of confocal as a system of collection. 3D interferometric lattice light-sheet (3D-iLLS) implements three objectives to excite the sample and collect emission along two paths where one path adds a variable delay path.[34] The scheme can be found in Figure 5.7A. This

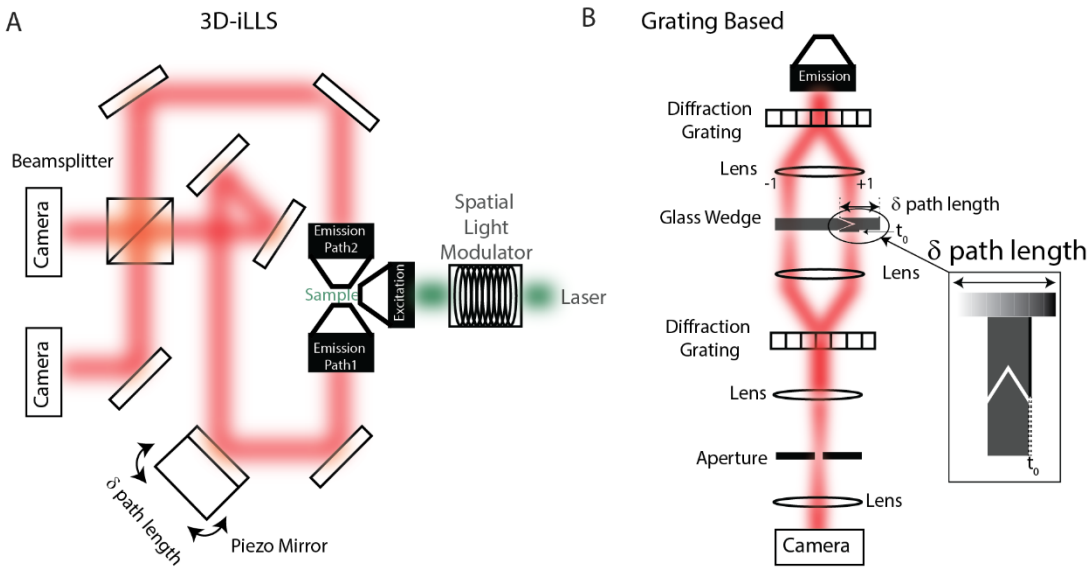

Figure 5.7 Wide-Field Interferometry

A. Wide field interferometric approach, 3D-iLLS where light sheet and SIM microscopy are combined to interfere sheets of light. The path length difference is controlled by a piezo mirror, figure adapted.[34] B. Wide field interferometry diffraction-based measurements. Emission is sent through a diffraction grating that splits the light and sends it through a glass wedge. The glass is translated to create a path delay. After, a similar grating recombines the emission which is then passed through an aperture to reject secondary diffraction modes. Finally, emission is focused on a camera, figure adapted.[35]

route offers resilient resolution in both the equatorial and axial plane when being combined in tandem with SIM allowing for super-resolution spectral imaging. The disadvantage to this technique, however, is the need for three objectives and spatial light modulator making the setup technically more complex and rather expensive.

Grating Based

Another method splits the incoming light with transmission gratings in reflection mode. In this design, the two arms of the interferometer are formed by two transmission gratings: one that splits the image and other that combines it. After the initial gratings the split image is sent down

two parallel paths. The incident beam is then focused on two subsequent glass wedges. One wedge remains stationary while the other moves. These wedges are complimentary in the way they are cut (Figure 5.7B) with a gap introduced in the interface where the wedges meet. The translation will change the thickness of the air gap that is between the surfaces of the two wedges. An additional thickness of glass is added to the end of a glass wedge to introduce a negative path delay. After this, light is recombined with a similar grating and passed through an aperture to block off-axis order diffractions. Finally, the photon stream is focused onto a camera where a hyperspectral image can be recorded.[35] The disadvantage here being the loss of wavelength agnostic optics that can be advantageous in the DAFS work.

References

1. Hendriksen, B. A., Sanchez-Felix, M. V. & Tam, K. Y. A New Multiwavelength Spectrophotometric Method for the Determination of the Molar Absorption Coefficients of Ionizable Drugs . *http://dx.doi.org/10.1081/SL-120013129* **35**, 9–19 (2007).

2. Rivera, L. *et al.* Simple dip-probe fluorescence setup sensor for in situ environmental determinations. *Sens Actuators B Chem* **137**, 420–425 (2009).

3. Kavanagh, K. Y. *et al.* Microspectrophotometric analysis of respiratory pigments using a novel fibre optic dip probe in microsamples. *Physiol Meas* **20**, 303 (1999).

4. Mhatre, A. M., Chappa, S., Gupta, S. K. & Pandey, A. K. LED based optical dip-probe spectrophotometer for in situ monitoring of uranyl and uranous ions in aqueous process stream. *Microchemical Journal* **183**, 108019 (2022).

5. Mutter, M. & Vuilleumier, S. A Chemical Approach to Protein Design—Template-Assembled Synthetic Proteins (TASP). *Angewandte Chemie International Edition in English* **28**, 535–554 (1989).

6. Ennist, N. *et al.* De novo design of energy transfer proteins housing excitonically coupled chlorophyll special pairs. doi:10.21203/rs.3.rs-2736786/v1.

7. Deshmukh, A. P. *et al.* Design Principles for Two-Dimensional Molecular Aggregates Using Kasha's Model: Tunable Photophysics in Near and Short-Wave Infrared. (2019) doi:10.1021/acs.jpcc.9b05060.

8. Laptenok, S. P. *et al.* Global analysis of Förster resonance energy transfer in live cells measured by fluorescence lifetime imaging microscopy exploiting the rise time of acceptor fluorescence. *Phys Chem Chem Phys* **12**, 7593–7602 (2010).

9. Hirvonen, L. M. *et al.* Lightsheet fluorescence lifetime imaging microscopy with wide-field time-correlated single photon counting. *J Biophotonics* **13**, (2020).

10. Bowman, A. J., Klopfer, B. B., Juffmann, T. & Kasevich, M. A. Electro-optic imaging enables efficient wide-field fluorescence lifetime microscopy. *Nature Communications 2019 10:1* **10**, 1–8 (2019).

11. Gersbach, M. *et al.* High frame-rate TCSPC-FLIM using a novel SPAD-based image sensor. *https://doi.org/10.1117/12.860769* **7780**, 357–369 (2010).

12. Ulku, A. C. *et al.* A 512 × 512 SPAD image sensor with integrated gating for widefield FLIM. *IEEE Journal of Selected Topics in Quantum Electronics* **25**, (2019).

13. Yudovich, S. *et al.* Ratiometric widefield imaging with spectrally balanced detection. *Biomed Opt Express* **10**, (2019).

14. Tenney, S. M. *et al.* Mesoscale Quantum-Confined Semiconductor Nanoplatelets through Seeded Growth. *Chemistry of Materials* **34**, 6048–6056 (2022).

15. Rust, M. J., Bates, M. & Zhuang, X. Sub-diffraction-limit imaging by stochastic optical reconstruction microscopy (STORM). *Nat Methods* **3**, 793–795 (2006).

16. Gustafsson, M. G. L. Surpassing the lateral resolution limit by a factor of two using structured illumination microscopy. *J Microsc* **198**, 82–87 (2000).

17. Hell, S. W. Fluorescence nanoscopy: Breaking the diffraction barrier by the RESOLFT concept. *NanoBiotechnology* **2005**, (2005).

18. Elson, E. L. Fluorescence Correlation Spectroscopy: Past, Present, Future. *Biophys J* **101**, 2855 (2011).

19. De Thomaz, A. A., Almeida, D. B., Pelegati, V. B., Carvalho, H. F. & Cesar, C. L. Measurement of the hydrodynamic radius of quantum dots by fluorescence correlation spectroscopy excluding blinking. *Journal of Physical Chemistry B* **119**, 4294–4299 (2015).

20. Zhang, L., Perez-Romero, C., Dostatni, N. & Fradin, C. Using FCS to accurately measure protein concentration in the presence of noise and photobleaching. *Biophys J* **120**, 4230–4241 (2021).

21. Levitus, M. Relaxation kinetics by fluorescence correlation spectroscopy: Determination of kinetic parameters in the presence of fluorescent impurities. *Journal of Physical Chemistry Letters* **1**, 1346–1350 (2010).

22. Lupton, J. M. & Vogelsang, J. Photon correlations probe the quantized nature of light emission from optoelectronic materials. *Appl Phys Rev* **8**, 041302 (2021).

23. Amgar, D., Yang, G., Tenne, R. & Oron, D. Higher-Order Photon Correlation as a Tool to Study Exciton Dynamics in Quasi-2D Nanoplatelets. *Nano Lett* **19**, 8741–8748 (2019).

24. Verberk, R. & Orrit, M. Photon statistics in the fluorescence of single molecules and nanocrystals: Correlation functions versus distributions of on- and off-times. *J Chem Phys* **119**, 2214 (2003).

25. Lounis, B. & Orrit, M. Single-photon sources. *Reports on Progress in Physics* **68**, 1129 (2005).

26. Kimble, H. J., Dagenais, M. & Mandel, L. Photon Antibunching in Resonance Fluorescence. *Phys Rev Lett* **39**, 691 (1977).

27. Fleury, L., Segura, J. M., Zumofen, G., Hecht, B. & Wild, U. P. Nonclassical Photon Statistics in Single-Molecule Fluorescence at Room Temperature. *Phys Rev Lett* **84**, 1148 (2000).

28. Basché, T., Moerner, W. E., Orrit, M. & Talon, H. Photon antibunching in the fluorescence of a single dye molecule trapped in a solid. *Phys Rev Lett* **69**, 1516 (1992).

29. Nair, G., Zhao, J. & Bawendi, M. G. Biexciton quantum yield of single semiconductor nanocrystals from photon statistics. *Nano Lett* **11**, 1136–1140 (2011).

30. Utzat, H., Utzat, H., Bawendi, M. G. & Bawendi, M. G. Lifetime-resolved photon-correlation Fourier spectroscopy. *Optics Express, Vol. 29, Issue 10, pp. 14293-14303* **29**, 14293–14303 (2021).

31. Gómez, D. E., Van Embden, J. & Mulvaney, P. Spectral diffusion of single semiconductor nanocrystals: The influence of the dielectric environment. *Appl Phys Lett* **88**, 154106 (2006).

32. DeLange, O. E. Optical heterodyne detection. *IEEE Spectr* **5**, 77–85 (1968).

33. Corsetti, S. *et al.* Widefield light sheet microscopy using an Airy beam combined with deep-learning super-resolution. *OSA Continuum, Vol. 3, Issue 4, pp. 1068-1083* **3**, 1068–1083 (2020).

34. Cao, B., Coelho, S., Li, J., Wang, G. & Pertsinidis, A. Volumetric interferometric lattice light-sheet imaging. *Nat Biotechnol* **39**, 1385 (2021).

35. Yaqoob, Z. *et al.* Near-common-path interferometer for imaging Fourier-transform spectroscopy in wide-field microscopy. *Optica, Vol. 4, Issue 5, pp. 546-556* **4**, 546–556 (2017).

36. Stochastic Optical Reconstruction Microscopy (STORM) Imaging | Nikon's MicroscopyU. https://www.microscopyu.com/tutorials/stochastic-optical-reconstruction-microscopy-storm-imaging.

37. Cui, J., Beyler, A. P., Bischof, T. S., Wilson, M. W. B. & Bawendi, M. G. Deconstructing the photon stream from single nanocrystals: from binning to correlation. *Chem Soc Rev* **43**, 1287–1310 (2014).